THERMAL DRAWING OF LOW-DIMENSIONAL MATERIAL-INTEGRATED TRIBOELECTRIC FIBERS FOR HEALTHCARE APPLICATIONS

A THESIS SUBMITTED TO

THE GRADUATE SCHOOL OF ENGINEERING AND SCIENCE

OF BILKENT UNIVERSITY

IN PARTIAL FULFILLMENT OF THE REQUIREMENTS FOR

THE DEGREE OF

MASTER OF SCIENCE

IN

MATERIALS SCIENCE AND NANOTECHNOLOGY

By

Md Sazid Bin Sadeque

July 2024

Thermal drawing of low-dimensional material-integrated triboelectric fibers for healthcare applications
By Md Sazid Bin Sadeque
July 2024

We certify that we have read this thesis and that in our opinion it is fully adequate, in scope and in quality, as a thesis for the degree of Master of Science.

Mustafa Ordu(Advisor)

Bilge Baytekin

Yusuf Keleştemur

Approved for the Graduate School of Engineering and Science:

Orhan Arıkan
Director of the Graduate School

ABSTRACT

THERMAL DRAWING OF LOW-DIMENSIONAL MATERIAL-INTEGRATED TRIBOELECTRIC FIBERS FOR HEALTHCARE APPLICATIONS

Md Sazid Bin Sadeque
M.S. in MATERIALS SCIENCE AND NANOTECHNOLOGY
Advisor: Mustafa Ordu
July 2024

The potential of flexible wearable devices and sensors to revolutionize healthcare lies in their ability to facilitate real-time monitoring. However, many of these wearable sensors are extensive energy consumers, and the requirement of bulky energy storage devices significantly hampers their acceptability. Currently available sensing devices mostly employ film-based devices, which lack breathability, reducing their applicability in widespread healthcare applications. Triboelectric nanogenerators (TENGs) are environmentally sustainable devices that convert mechanical and biomechanical energy into electrical output through the synergetic processes of triboelectrification and electrostatic induction. These devices effectively harvest low-frequency mechanical and biomechanical energy and enable self-powered sensing. TENG performance can be enhanced by incorporating low dimensional materials with high specific surface area into flexible ferroelectric polymers. Ferroelectric polyvinylidene fluoride (PVDF) and its copolymers are particularly advantageous due to their high dielectric constant and abundant highly electronegative fluorine ions. Various low dimensional materials can interact with the polar groups of PVDF and reorient them to conform to electroactive phases. Moreover, they can also form micro-capacitors and modulate the surface properties of nanocomposite. In this thesis, we aim to prepare a triboelectric nanogenerator integrated textile fiber with self-energy generating ability and breathability as textiles. We employed the thermal drawing process as a fabrication platform for preparing continuous triboelectric fibers. Graphene nanoplatelet (GNP) and Molybdenum disulfide (MoS_2) are added to the PVDF matrix to improve triboelectric properties. β phases of thermally drawn nanocomposite fibers demonstrate significant improvement and were increased to 37.6%, 39.5%, and 43.3% for 1, 3, 5% GNP integration. For the case of MoS_2, β phase increases to

47.5% for 3 wt%MoS_2; however, β phase decreases beyond 3 wt%. The nanocomposite TENG fibers demonstrate improved triboelectric properties. The fibers show superior sensitivity, flexibility and durability, enabling their applications in critical healthcare applications.

Keywords: Triboelectric nanogenerator, thermal drawing, wearable sensors, respiration monitoring, blinking monitoring.

ÖZET

BYOHAREKET ALGILAMA VE SALIK UYGULAMALARI ÇN DÜÜK BOYUTLU MALZEMELER ENTEGRE TRBOELEKTRK FBERLERN TERMAL ÇZM

Md Sazid Bin Sadeque
Malzeme Bilimi ve Nanoteknoloji Yüksek Lisans, Yüksek Lisans
Tez Danışmanı: Mustafa Ordu
July 22, 2024

Esnek giyilebilir cihazların ve sensörlerin sağlık hizmetlerinde devrim yaratma potansiyeli, gerçek zamanlı izlemeyi kolaylaştırma yeteneklerinde yatmaktadır. Ancak, bu giyilebilir sensörlerin çoğu yoğun enerji tüketicileridir ve büyük enerji depolama cihazlarının gerekliliği, kabul edilebilirliklerini önemli ölçüde engellemektedir. Şu anda mevcut algılama cihazları çoğunlukla, nefes alabilirliği olmayan film bazlı cihazlar kullanılmakta olup, bu durum bunların yaygın sağlık uygulamalarında uygulanabilirliklerini azaltmaktadır. Triboelektrik nanojeneratörler (TENG'ler), triboelektrifikasyon ve elektrostatik indüksiyonun Sinerjetik süreçleri yoluyla mekanik ve biyomekanik enerjiyi elektrik çıkışına dönüştüren, çevresel açıdan sürdürülebilir cihazlardır. Bu cihazlar, düşük frekanslı mekanik ve biyomekanik enerjiyi etkili bir şekilde toplar ve kendi kendine çalışan algılamayı mümkün kılar. TENG performansı, yüksek spesifik yüzey alanına sahip düşük boyutlu malzemelerin esnek ferroelektrik polimerlere dahil edilmesiyle artırılabilir. Ferroelektrik poliviniliden florür (PVDF) ve kopolimerleri, yüksek dielektrik sabitleri ve yüksek derecede elektronegatif flor iyonlarının bolluğu nedeniyle oldukça avantajlıdır. Çeşitli düşük boyutlu malzemeler, PVDF'nin polar gruplarıyla etkileşime girebilir ve bunları elektroaktif fazlara uyacak şekilde yeniden yönlendirebilir. Ayrıca bu malzemeler mikro kapasitörler oluşturabilir ve nanokompozitin yüzey özelliklerini modüle edebilir. Bu tezde, kendi kendine enerji üretme yeteneğine ve tekstil olarak nefes alabilirliğe sahip triboelektrik nanojeneratörle entegre bir tekstil fiberi hazırlayarak sorunu ele almayı amaçlıyoruz. Bu çalışmada, kesintisiz triboelektrik fiberlerin hazırlanmasında termal çekme işlemi üretim platformu olarak kullandık. Triboelektrik özellikleri geliştirmek için PVDF matrisine grafen nanoplatelet

(GNP) ve Molibden disülfit (MoS_2) eklenmesi yapılmıştır. Termal olarak çekilmiş nanokompozit fiberlerin β fazları önemli bir gelişme göstermektedir ve %1, %3, %5 GNP entegrasyonu ile %37,6, %39,5 ve %43,3'e yükseltilmiştir. MoS2 durumunda, β fazı ağırlıkça %3 MoS_2 miktarı ile %47,5'e yükselir; ancak, β fazı ağırlıkça %3 MoS_2'nin ötesinde azalmaktadır. Nanokompozit TENG lifleri gelişmiş triboelektrik özellikler göstermektedir. Fiberler kritik sağlık uygulamalarında kullanılmalarını mümkün kılacak şekilde üstün hassasiyet, esneklik ve dayanıklılık göstermektedir.

Anahtar sözcükler: Triboelektrik nanojeneratör, ısıl çekim, giyilebilir sensörler, solunum izleme, göz kırpma izleme..

Acknowledgement

I extend sincere gratitude to my advisor, Dr. Mustafa Ordu, whose guidance, expertise, and encouragement have been indispensable. His dedication to excellence and commitment to my professional development have motivated me along the way. His constructive criticism, insightful feedback, and unwavering support have guided me through challenges. I am sincerely grateful for his mentorship and the confidence he has shown in my abilities.

I am thankful to all past and present members of our research group at the Contemporary Fibers Laboratory. Their diverse perspectives and passion for knowledge have created a stimulating academic environment for me. I would like to express my appreciation to my friends and colleagues for their support, encouragement the during challenging times. Their friendship, laughter, and shared experiences have provided much-needed balance throughout my academic journey.

I am deeply thankful to the National Nanotechnology Research Center-UNAM for providing a conducive academic environment and access to state-of-the-art research facilities. I gratefully acknowledge the engineers and technicians from UNAM for their technical support and expertise. I am also thankful to Dr. Mehmet Yilmaz and Dr. Talip Serkan Kasırga for their generous support in providing access to electrical characterization equipments. Their willingness to share their expertise and resources has significantly enhanced the quality of my work.

Financial support from the Scientific and Technological Research Council of Turkey (TÜBİTAK) is gratefully acknowledged. This support has provided essential resources and opportunities that have enabled me to conduct in-depth research, and advance my academic career.

I would like to acknowledge the members of my thesis jury board, Dr. Bilge Baytekin and Dr. Yusuf Keleştemur for their rigorous examination and valuable

feedback on my work. Their expertise and insights have significantly enriched this thesis and helped refine its scholarly contributions.

I am deeply grateful to my parents for their support, love, and encouragement throughout my academic journey. Their sacrifices and belief in my abilities have been fundamental to my achievements. Their guidance has not only shaped my academic pursuits but also molded my character, and I owe them a debt of gratitude for their enduring patience and unwavering faith in my aspirations.

I am deeply indebted to everyone who has supported me with their wisdom, encouragement, and contributions. Your belief in my abilities and dedication to my success have been invaluable to me.

Contents

1 Introduction **1**

1.1 Introduction 1

1.2 Approaches for self-powered sensing 4

1.2.1 Electromagnetic nanogenerator 4

1.2.2 Piezoelectric Nanogenerator 5

1.2.3 Magnetoelastic nanogenerator 5

1.2.4 Thermoelectric nanogenerator 6

1.2.5 Hybrid nanogenerator 7

1.2.6 Triboelectric Nanogenerator 8

1.3 Challenges 9

1.3.1 Charge generation and transfer mechanism between polymer fibers 10

1.3.2 Wearability and comfortability 10

1.3.3 Scalable manufacturability compatible with mature industrial production 10

1.3.4 Long-term working stability and durability 11

1.3.5 Impedance and capacitance matching with energy storage devices 11

1.4 Motivation 11

2 Graphene nanoplatelet integrated thermally drawn PVDF triboelectric nanocomposite fibers for biomotion sensing 16

2.1 Introduction 17

2.2 Experimental Section 19

2.2.1 Chemicals and films 19

2.2.2 Sensor Fabrication 19

2.2.3 Materials Characterization 20

2.2.4 Electrical Characterization 20

2.2.5 High-Temperature Electrical Characterization 20

2.2.6 Durability test 21

2.2.7 Surface Roughness Measurement 22

2.3 Fabrication of Triboelectric Fibers 22

2.4 Materials Characterization 25

2.5 Electrical Characterization 30

2.6 Durability Test 42

2.7 Temperature Dependence of the Triboelectric Output 44

2.8 TENG Fabric for Self-Powered Sensing and Energy Harvesting . . 46

2.9 Summary 52

3 Thermal drawing of MoS_2 integrated PVDF triboelectric fibers for continuous respiration monitoring 53

3.1 Introduction 54

3.2 Experimental Section 56

3.2.1 Chemicals and films 56

3.2.2 Preparation of triboelectric nanocomposite film 56

3.2.3 Preparation of triboelectric fiber 57

3.2.4 Materials characterization 57

3.2.5 Electrical characterization 58

3.3 Fabrication of Triboelectric Fibers 58

3.4 Materials Characterization 60

3.5 Electrical Characterization 70

3.6 Triboelectric Fiber for Wearable Sensors 77

3.7 Triboelectric Face Mask for Respiration Monitoring 78

3.8 Summary 81

4 Conclusion and future prospective **82**

A Experimental setup **117**

B Code **119**

B.1 Arduino code with digital filter 119

B.2 Matlab code for data acquisition 120

List of Figures

1.1 Configuration of an electromagnetic generator. (a) with a moving magnet and the fixed coils[1]. (b) with the moving coils and fixed magnet[2].(Reproduced with permission. Copyright © 2019, Elsevier,Copyright © 2018, Elsevier) 4

1.2 Working mechanism of piezoelectric nanogenerator[3].(Reproduced with permission. Copyright © 2022, Springer.) 5

1.3 Working principle of a magnetoelastic nanogenerator[4].(Reproduced with permission. Copyright © 2023, Wiley Online Library.) . . . 6

1.4 Working principle of a thermoelectric nanogenerator[5].(Reproduced with permission. Copyright © 2012, ACS Publications.) 7

1.5 Electron cloud model of tribo electrification[6].(Reproduced with permission. Copyright © 2022, Frontiers.) 9

1.6 Recent development trend of TENG integrated with textile[7].(Reproduced with permission. Copyright © 2021, Springer.) 13

2.1 Fabrication procedure for GNP-PVDF triboelectric fiber. (a) Solution processing of GNP and PVDF to produce a dry nanocomposite film. (b) Schematic of the thermal drawing process for continuous TENG fiber. Fiber cross sectional image. (c) SEM image of the drawn fiber. Scale bar: 500 μm. (d) LSCM image of the drawn fiber's cross-section. Scale bar: 100 μm. 23

2.2 Continuously drawn long-length nanocomposite fiber. 24

2.3 Raman spectra of multilayered GNP. 25

2.4 Material characterization of thermally drawn fibers. FTIR spectra of the PVDF fiber and GNP-PVDF nanocomposite fibers with various wt.% 26

2.5 (a) FTIR and (b) XRD spectra of PVDF film[8]. 27

2.6 Material characterization of thermally drawn fibers. XRD spectra of the PVDF fiber and GNP-PVDF nanocomposite fibers with various wt.% 28

2.7 Contact area maximization due to surface roughness. (a) Contact between two flat hard surfaces. No increment of real contact area occurs. (b) Contact between a hard-flat surface and a soft-rough surface. A decrease in real contact area occurs due to the flattening of the soft, rough surface. (c) Contact between a soft flat surface and a soft-rough surface. An increase in the real contact area occurs. 29

2.8 Surface profile and surface roughness measurement. (a) and (b) surface profiles of pure PVDF fiber. (c) and (d) surface profiles of PGr-5 fiber. 30

2.9 LSCM surface images of pure PVDF fiber and PGr-5 fiber. Scale bar 50 μm. 31

2.10 Electrical characterization of thermally drawn TENG fiber. (a) Working principle of a single electrode (SE mode) TENG fiber. (b) Open circuit voltage (V_{oc}) and (c) Short circuit current (I_{sc}) of pristine and PGr-(1-5%) TENG fiber (contact length: 3 cm and frequency: 5 Hz). (d) Peak power output for PGr-5 fiber and only PVDF fiber with equivalent circuit connection for measuring power output. 32

2.11 Micro-capacitor formation due to interaction between GNP and PVDF enhancing electron trapping. 34

2.12 Charge decay in a tribonegative surface. (a) Generation of negative charge in tribonegative surface. (b) Depletion of charge density due to charge decay. 35

2.13 (a) Output voltage V_{oc} and (b) current I_{sc} of PGr-5 TENG fiber at varied contact lengths (1-4 cm) at 5 Hz frequency. 36

2.14 (a) Output voltage V_{oc} and (b) current I_{sc} of PGr-5 fiber TENG at varied frequencies (1, 3, 5, and 7 Hz) with a 3 cm contact length. 36

2.15 Construction of plain-woven fabric. Cotton warp placed in the warp direction and continuous PGr-5 TENG fiber in the weft direction. 37

2.16 Electrical characterization of thermally drawn TENG fabric. (a) V_{oc} of PGr-5 TENG fabric at varied frequencies (1, 3, 5, and 7 Hz) with a 3 cm contact length. (b) V_{oc} of PGr-5 TENG fabric at varied contact areas at 5 Hz frequency. (c) The power output of PGr-5. 38

2.17 (a) I_{sc} of PGr-5 TENG fabric at varied frequencies (1, 3, 5, and 7 Hz) with 3 cm contact length (b) I_{sc} of PGr-5 TENG fabric at varied contact area (2,4,6 and 8cm2) at 5 Hz frequency. 39

2.18 (a) Prepared fabric with varied cotton yarn thickness. (b) Power density and (c) current density of TENG fabric prepared from varied cotton yarn thickness. 40

2.19 Power output for fabric sensor prepared with (a) 287 tex, (b) 440 tex and (c) 897 tex cotton warp. 41

2.20 Durability test for PGr-5. (a) PGr-5 fiber's surface image at different stages of thousands of tapping cycles Scale bar: 10 μm. (b) Reliability of output voltage for thousands of tapping cycles. Washability test for (c) fiber and (d) fabric. Both fiber and fabric demonstrated stable output during multiple washing cycles. (e) Saltwater stability for PGr-5 fiber. Voltage output of the PGr-5 fiber during multiple (f) cooling and (g) heating cycles. 43

2.21 (a) TENG fiber wrapped around a pencil demonstrating its flexible property. (b) The knotting of TENG fiber demonstrates its applicability in textile processing. (c) Bending of TENG fabric in the horizontal and vertical direction. 45

2.22 Temperature dependence of triboelectric output. (a) V_{oc} and (b) I_{sc} of the PGr-5 fiber at different temperatures. Power output for PGr-5 (c) at room temperature and (d) 100°C. (e) Peak power output for PGr-5 at room temperature and 100°C. 46

2.23 Demonstration of real-world applications with TENG sensor. (a) Smart TENG sock prepared by TENG fabric attachment at the heel region. (b) Detection of walking pattern using TENG output. (c) Variation of open circuit voltage at varied human movement speed (sensor was attached on right sock only). (d) Step count measurement (sensor was attached to both socks). 47

2.24 Characteristic output voltage for failing of gate (FOG). 48

2.25 Output voltage for (a) slow walk, (b) fast walk with period T between each cycle (sensor was attached on right sock only). . . . 49

2.26 TENG sensor attached between the forearm and upper arm region for arm movement monitoring. (a) Sensor attachment. (b) Arm bending detected through monitoring of output. 49

2.27 Hand grasping test for PGr-5 TENG. (a) Sensor placement on palm. (b) Detection of hand grasping by the Fabric TENG. (c) Detection of high and slow-frequency grasping. 50

2.28 (a) V_{oc} and (b) I_{sc} for hand tapping with one to four fingers. . . . 50

2.29 Rectified output voltage using a bridge rectifier. 51

2.30 (a) Setup for powering up simple electronic instrument. (b) Equivalent circuit. (c) Hand tapping to power up a table clock. 52

3.1 Fabrication procedure for MoS_2 - PVDF nanocomposite fibers. (a) Solution processing of MoS_2 and PVDF to produce uniform nanocomposite solution. (b) Preparation of final preform by casting and rolling. (c) Schematic of the thermal drawing process for continuous TENG fiber. (d) Continuous TENG fiber acquired from the thermal drawing process. (e) LSCM image of the drawn fiber's cross-section (Scale bar: 50 μm). 60

3.2 SEM image of the as-received bulk MoS_2 (Scale bar: 50 μm). . . . 61

3.3 (a) and (b) XPS analysis of the as-received bulk MoS_2. (c) XRD spectra of bulk MoS_2 before and after ultrasonication. 61

3.4 α, β and γ configurations of PVDF. 62

3.5 Material characterization of thermally drawn MoS_2-PVDF nanocomposite fibers. (a) XRD and (b) FTIR spectra of the 0 wt% MoS_2 - PVDF fiber and MoS_2-PVDF nanocomposite fibers with various wt%. 63

3.6 FTIR spectra of 0% MoS_2 film, 3% MoS_2 film and 3% MoS_2 fiber. 64

3.7 Comparative analysis of the β-phase formation between MoS_2, GNP and MXene ($Ti_3C_2T_x$) integrated nanocomposite TENG fibers[8, 9]. 65

3.8 SEM and XPS analysis of PM3 nanocomposite fiber. (a) SEM image (Scale bar: 500 μm) and zoomed-in view of the mapping point (Scale bar: 2 μm). (b) EDS element maps of F, C, Mo and S. (c) EDX spectra of PM3 fiber. (d) XPS survey of PM0 and PM3 fibers. (e) Zoom-in view of the XPS survey from 150 to 250 eV. High-resolution XPS spectra of (f) Mo3d and (g) S2p. 66

3.9 High-resolution XPS spectra of PM3 fiber for (a) C1s and (b) F1s. 67

3.10 EDS elemental mappings for the surface agglomeration of MoS_2 in PVDF fibers at different nanoparticle concentrations: (a) 1 wt% MoS_2, (b) 2 wt% MoS_2, (c) 3 wt% MoS_2, (d) 4 wt% MoS_2 and (e) 5 wt% MoS_2 (Scale bar: 2 μm). 68

3.11 Surface morphologies of (a) PM0, (b) PM1, (c) PM2, (d) PM3, (e) PM4 and (f) PM5 fibers (Scale bar: 500 μm). 69

3.12 (a) XRD and (b) FTIR spectra of MoS_2 and GNP integrated PVDF TENG fibers and (c) their corresponding β-phase formations. 70

3.13 Comparative cross-sectional analysis of the pristine, single and dual nanoparticle integrated TENG fibers (a) 0 wt% MoS_2, (b) 3 wt% MoS_2, (c) 2 wt% MoS_2 and 1 wt% GNP, (d) 1 wt% MoS_2 and 2 wt% GNP and (e) 3 wt% MoS_2 and 2 wt% GNP. 71

3.14 Electrical characterization of the TENG fiber. (a) The working mechanism of TENG fiber in the single electrode mode. (b) Open circuit voltage output of TENG fibers at different nanoparticle concentrations. (c) Peak power output comparison for 0 wt% and 3 wt% MoS_2 - PVDF fiber. 73

3.15 Electrical characterization of the PM3 fiber. (a) V_{oc} and (b) I_{sc} of the PM3 fiber at different frequencies. (c) V_{oc} and (d) I_{sc} or the PM3 fiber at different contact lengths. 74

3.16 Electrical characterization of PM3 fabric. (a) Woven fabric structure comprised of PM3 fiber. (b) V_{oc} and (c) I_{sc} of the PM3 fabric at different frequency. (d) V_{oc} and (e) I_{sc} of the PM3 fabric at different contact area. 75

3.17 TENG fiber for skin interfaced sensor. (a) Schematic of the data acquisition and monitoring system. (b) Fiber sensor attached to the upper eyelid. (c) Sensor response during slow and fast blinking. (d) The fiber sensor is attached to the index finger. (e) Detection of various finger bending motions with attached sensor output. . . 76

3.18 Wearable triboelectric mask for respiration monitoring. (a) The schematic of the commercial mask, TENG fiber directly woven into the mask. (b) Respiration cycle. (c) Respiration sensor working mechanism. (d) Detection of various respiration stages with TENG mask sensor. (e) Long-time stability of the signal output from the TENG sensor integrated with a wearable face mask. 80

A.1 Electrical characterization setup. 117

A.2 Set up of wash-ability test for TENG fiber. 118

A.3 Electrical characterization set up for temperature dependence test on triboelectric output. (b) Custom-made small tapping device that was placed over the hot plate. 118

List of Tables

2.1 Summary of the performance of textile based TENGs (single electrode mode). 41

Chapter 1

Introduction

1.1 Introduction

Textiles have been are key elements for human civilization, providing aesthetics, safety, and comfort from the surrounding harsh environment. In this era of the Internet of Things (IoT), integrating smart functionalities into our clothing for sensing, actuating, and communication has become a necessary trend to ensure human well-being. With the development of soft materials, sensor architecture, and integration technologies, research on textile-based wearable electronics has reached a critical milestone that impacts our everyday lives. However, the widespread use of wearable devices is greatly hampered by the necessity of a maintenance-free, sustainable, and flexible power source for sensing applications.

The rapid advancement of nanotechnology has enabled the fabrication of multifunctional e-textiles, which has contributed significantly to the field of wearable electronics[10]. Wearable e-textile devices are exposed to various sustainable energy sources such as biomotion, biofluids, body heat, solar irradiation, and a vast amount of physiological data[11, 12]. Harnessing these vast resources while keeping the textile wearable and breathable is a key challenge for the research

community. Among all the energy sources for wearable electronics, biomechanical energy is one of the most diverse and abundant[13]. Various nanogenerator devices have been proposed to harness this biomechanical energy (electromagnetic, piezoelectric, triboelectric energy, and magnetoelastic)[14]. Triboelectric nanogenerators are recently implemented energy harvesting device that has come to the spotlight in recent years. As a wearable e-textile device, TENG has been pushing forward the advancement of self-sustainable IoT, implantable electronics, and self-powered sensing and energy harvesting.

TENGs have been utilized for different applications by exploiting the wide range of material choices and available operational modes[15, 16]. Irrespective of TENG's application as an energy harvester or a self-powered sensor, the high energy conversion efficiency desired for practical applications is still far from achieved due to the low surface charge density of polymeric TENGs. Various methods have been applied to enhance surface charge density, which includes material selection with high inherent charge density[17, 18], material modification[19, 20, 21], charge injection through corona charging or polarization[22, 23], and device structure optimization[24, 25, 26, 27]. However, these methods require complex fabrication procedures, special materials, and expensive equipment, which raise the total manufacturing cost, rendering them unsuitable for widespread applications[20, 21]. Thus, a material with high charge affinity and electron trapping properties is desirable for enhanced triboelectric output.

A wide range of polymeric materials have recently been investigated as friction layers in triboelectric nanogenerators, and they offer promising charge density[28]. Ferroelectric fluoropolymers like polyvinylidene fluoride (PVDF) have garnered significant interest due to their high electronegativity, flexibility, and tunable polarizability[29, 30]. Different strategies, including ion injection[31], increment of dielectric constant[32], spontaneous polarization[33], surface functionalization[34], and inclusion of charge trapping interlayer[35] have been reported to increase triboelectric output. Integration of low dimensional material has been widely utilized as an effective strategy to tune the dielectric property of a polymer nanocomposite to improve the charge density of the friction

layer[36].

Nanomaterials have received great attention in the field of TENGs due to their high surface area, excellent electrical properties, chemical stability and durability, tailorable surface properties, and enhanced charge storage capability[37, 38]. Various low dimensional materials have been reported with TENGs, for example, graphene, graphene oxide, MXenes, transition metal dichalcogenides (TMDs), black phosphorus (BP), layered metal-organic frameworks (MOFs), hexagonal boron nitride (h-BN), layered covalent-organic frameworks (COFs), and layered metals[39, 40, 41, 42, 43, 44, 45]. The atomically thin nature of low dimensional materials translates to a very large surface area per unit volume. This extensive surface area provides more opportunities for triboelectric charge transfer when the material comes into contact with another surface.

Previous studies of low dimensional material integrated PVDF nanocomposite TENG demonstrated the fabrication of PVDF nanocomposite membrane/film by solution processing[46] or preparation of nonwoven nanocomposite matt by electrospinning[47, 48]. Both methods require the seperate processing for electrode deposition while lacking the continous form which requires for e-textiles. Additionally, membrane/film-based TENGs are incompatible with the textile fabric manufacturing. In this respect, the thermal drawing process (TDP), a promising method where the polymer can be stretched to a thinner diameter over its glass transition temperature, can preserve the design of a multi-material preform from the macroscopic level to microscopic and even nanoscopic length scales[49]. Moreover, TDP can overcome the existing challenges by continuously co-drawing electrodes and triboelectric material to kilometer-long fibers in one draw within a few hours with an appropriate preform. In this thesis, we aim to extend our knowledge to understand the material and electric properties of low dimensional material integrated thermally drawn 1D fibers and demonstrate their applicability as wearable electronics.

1.2 Approaches for self-powered sensing

1.2.1 Electromagnetic nanogenerator

Electromagnetic nanogenerators (EMG) capitalize on electromagnetic induction to convert mechanical energy into electrical energy, which can be used for various applications, including powering sensors and other electronic devices[50]. It runs on the principle of Faraday's law of electromagnetic induction, which states that an induced current will be produced if a conductor is placed in a varying magnetic field or due to the inductor's movement in a static magnetic field. Thus, a moving magnet can introduce an alternating magnetic flux to a static conductor coil when designing an EMG (Figure 1.1a)[1]. Alternatively, the coil used to harvest mechanical energy can be attached to movable parts of the wearables, keeping the magnet fixed (Figure 1.1b)[2].

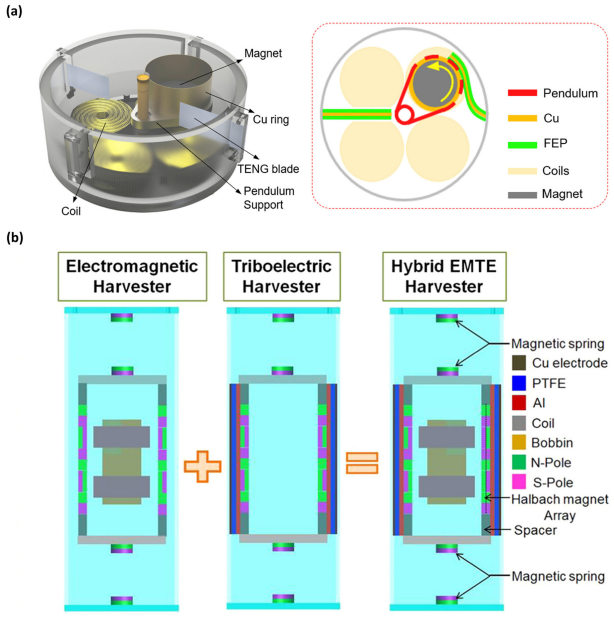

Figure 1.1: Configuration of an electromagnetic generator. (a) with a moving magnet and the fixed coils[1]. (b) with the moving coils and fixed magnet[2].(Reproduced with permission. Copyright © 2019, Elsevier,Copyright © 2018, Elsevier)

1.2.2 Piezoelectric Nanogenerator

Piezoelectric nanogenerators (PENG) consist of piezoelectric materials having electromechanical coupling ability in case of applied mechanical stress. Conversely, piezoelectric materials physically deform in the presence of an electrical field. Harnessing this unique ability, a wide variety of wearable piezoelectric sensing and energy harvesting devices have been designed. Two electrodes are attached to the piezoelectric material on both sides to harness the piezoelectric potential generated by applied stress (Figure 1.2a)[3]. In the case of applied stress, dipoles of the piezoelectric materials align in the same direction, which induces a potential difference between the two electrodes. This potential difference facilitates current flow between the electrodes (Figure 1.2 b-d).

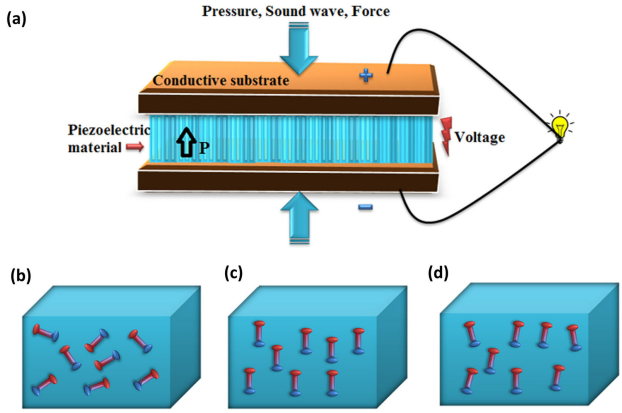

Figure 1.2: Working mechanism of piezoelectric nanogenerator[3].(Reproduced with permission. Copyright © 2022, Springer.)

1.2.3 Magnetoelastic nanogenerator

Magnetoelastic nanogenerators (MEG) utilizes magnetoelastic effect that is the change of the magnetic property of a material due to mechanical stress. With the magnetoelastic effect, mechanical energy can be converted into electrical energy. With the external application of mechanical motion, such as vibrations,

pressure, or bending, there is a deformation in the magnetoelastic material. The deformation changes the alignment of magnetic domains within the material[4]. This change in domain alignment modifies the local magnetic field. If the magnetoelastic material is coupled with a coil or an electrode setup, this change in the magnetic field can induce an electrical voltage across the coil or electrodes (Figure 1.3).

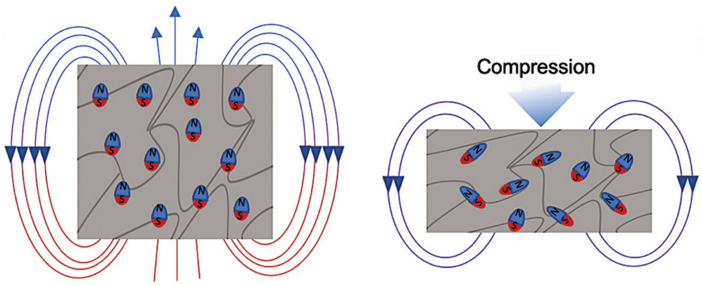

Figure 1.3: Working principle of a magnetoelastic nanogenerator[4].(Reproduced with permission. Copyright © 2023, Wiley Online Library.)

1.2.4 Thermoelectric nanogenerator

The thermoelectric nanogenerators(TEGs) function on the principle of thermoelectric (TE) effect, which enables the direct conversion of heat energy into electricity when there is a temperature difference between two electrodes of TE materials[5]. A π-type model illustrated in figure 1.4 explains this phenomenon where heating one side of a p-type or n-type material while cooling the other causes the majority carriers (holes (h+) in p-type materials and electrons (e-) in n-type materials) to move from the hot side to the cold side. This results in the generation of TE voltages in both p-type and n-type materials having the same direction. When an external circuit is connected, a functional circuit is established.

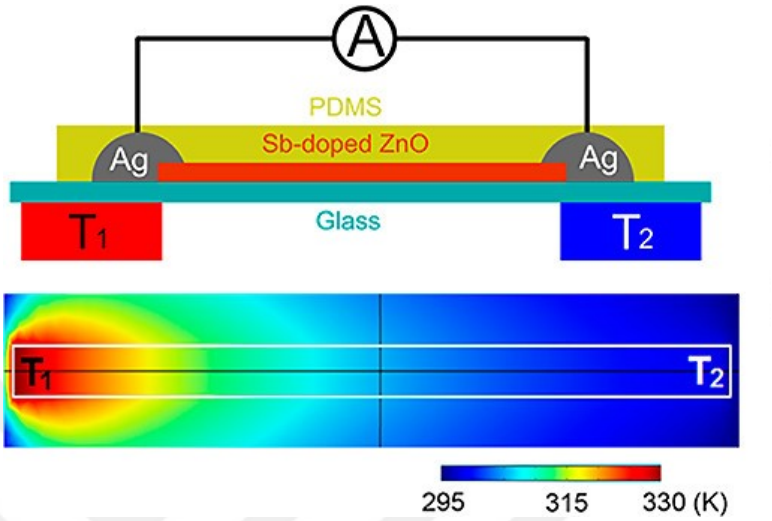

Figure 1.4: Working principle of a thermoelectric nanogenerator[5].(Reproduced with permission. Copyright © 2012, ACS Publications.)

1.2.5 Hybrid nanogenerator

A hybrid nanogenerator (HNG) integrates piezoelectric, thermoelectric, magnetoelastic, and triboelectric technologies to efficiently harvest energy from multiple sources, offering continuous and adaptable power generation for various applications. Hybrid nanogenerators are unique due to their ability to harvest energy from different sources simultaneously, maximizing the efficiency of energy scavenging[51]. These devices ensure continuous power generation by integrating mechanisms like mechanical vibrations, thermal gradients, and solar radiation. This versatility enhances energy capture efficiency and offers redundancy, ensuring uninterrupted operation in harsh weather conditions that disable one or multiple scavenging sources. This advantage makes hybrid nanogenerators invaluable for applications requiring sustained and reliable power, such as wearable electronics, IoT devices, and remote sensors, while also contributing to environmental sustainability through renewable energy sources.

1.2.6 Triboelectric Nanogenerator

Triboelectric nanogenerators(TENG) run on the principle of contact electrification (CE) and electrostatic induction. When two materials come into contact, one material tends to donate electrons while the other tends to accept electrons, leading to a charge imbalance. This charge separation can be harnessed to generate an electrical current when the material is connected through an external circuit. This electron transfer can occur between suitable materials of all phases, including solid-solid, solid-liquid, liquid-liquid, gas-liquid, gas-gas, and gas-solid. This is a significant advantage of triboelectric nanogenerators over other nanogenerator devices[6].

A material's tendency to gain or lose electrons during contact with other materials is determined by electron affinities and work functions of the two materials. When two materials with different work functions are brought into contact, electrons will transfer from the material with lower electron affinity to the one with higher. The Electron cloud model is proposed as a general explanation model for understanding the CE between any two materials. In this model, the outermost electrons of the atoms or molecules are considered a cloud of negative charge. During contact at the atomic level, overlap occurs between the two material's electron clouds, and electron transfer occurs based on the differences in their electron affinities. Electron transfer only occurs when the interatomic distance between two materials becomes lower than the bonding length. Thus, this electron cloud overlap caused a reduced interatomic potential barrier facilitating electron transfer between two materials (Figure 1.5).

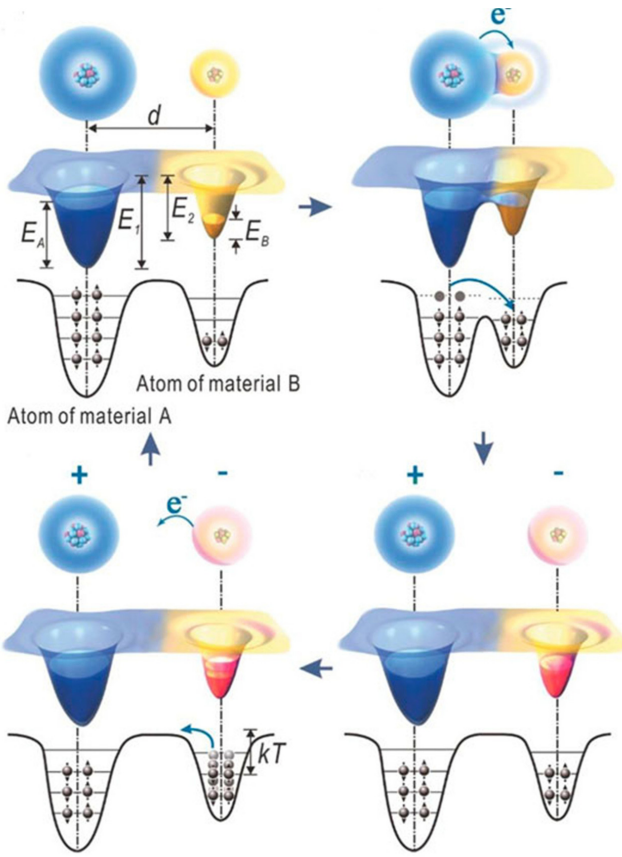

Figure 1.5: Electron cloud model of tribo electrification[6].(Reproduced with permission. Copyright © 2022, Frontiers.)

1.3 Challenges

Several key challenges have been identified that is limiting the performance of textile TENGs[7]. These issues restrict their power output and sensing accuracy, impeding their widespread adoption in commercial applications.

1.3.1 Charge generation and transfer mechanism between polymer fibers

Extensive research has analyzed the charge transfer mechanisms in conventional planner TENGs, a comparable understanding of textile TENGs with 1D structure remains limited. To bridge this knowledge gap and gain deeper insights into the interfacial processes occurring between polymer fibers, further investigations are necessary.

1.3.2 Wearability and comfortability

Balancing between wearability and functionality remains a significant challenge in the development of textile TENGs. For instance, the integration of micro/nanostructured functional materials to enhance performance may compromise biocompatibility and skin-friendliness. This can lead to adverse effects such as skin irritation, discomfort due to thermal fluctuations, and even potential for wound infections and inflammation. Additionally, complex chemical treatments employed to improve functionality can render garments stiff, negatively impacting their drape, softness, and breathability. Therefore, the design of textile TENGs requires consideration of both human-centric materials and readily deformable textile structures to achieve optimal wearability without sacrificing functionality.

1.3.3 Scalable manufacturability compatible with mature industrial production

The ultimate objective for textile TENGs is to achieve widespread adoption in commercial applications. However, the vast majority of current textile TENG designs remain confined to the laboratory setting. These prototypes are often characterized by intricate structures, limited scalability, fabrication processes demanding excessive resources, and inadequate long-term stability.

1.3.4 Long-term working stability and durability

The long-term working stability and durability of textile-based electronics are important considerations directly impacting their suitability for real-world applications. Both the mechanical and electrical stability of these devices are highly influenced by the employed textile structures, the utilized manufacturing methods, and the environmental conditions they operate in. Frequent or excessive external loads can compromise the integrity of the surface materials, leading to a decline in electrical output performance. Therefore, focus required on the improvement of the long-term stability and durability of textile TENGs by designing compact and robust fabric structures focusing on selecting wear-resistant materials.

1.3.5 Impedance and capacitance matching with energy storage devices

Self-powered systems rely heavily on energy storage devices to accumulate the electrical charges generated during motion and release them upon demand. Textile Triboelectric Nanogenerators (TENGs) exhibit a characteristic alternating current (AC) output with high open-circuit voltage and low short-circuit current. This inherent output characteristic creates a significant impedance and capacitance mismatch between TENGs (typically in the range of $10^5 - 10^7\,\Omega$) and energy storage devices (typically ranging from $10^{-2} - 10^4\,\Omega$)[7]. This mismatch presents a major limitation, significantly hindering the efficiency of direct energy transfer or storage within the system.

1.4 Motivation

Smart textile-based triboelectric nanogenerator (TENG) offers an innovative textile technology that combines traditional wearable fabrics with advanced TENG

devices. Smart textile TENGs retain the original softness and comfort of clothing while delivering continuous, stable, environmentally friendly functional properties. They offer great potential for diverse applications, such as wearable micro- and nanopower sources, self-powered sensing, healthcare monitoring, biomimetic systems, human-machine interfaces, and artificial intelligence. We envision that this technology will significantly advance the development of on-body wearable electronics and artificial intelligence in the future.

High electromechanical conversion efficiency and excellent wearability are fundamental conditions of textile TENG. However, a significant obstacle to the widespread integration of TENG is the absence of 1D TENG materials with high charge density. Almost all earlier works on TENG devices concentrated on fabricating planer TENG devices with very high triboelectric output, adding self-powered sensing ability; however, planer TENG is unsuitable for seamlessly integrating with textiles. Figure 1.6 depicts the recent chronological advancement of textile TENGs. The first breakthrough of continuous wearable TENG came with the 3D spacer technology with PTFE-coated nylon fabric and graphene-coated nylon fabric as triboelectric materials of opposite polarities. However, manufacturing and designing 3D knitted spacer structures can be complex, requiring specialized expertise and machinery. Also, the intricate production process may result in a higher production cost than traditional flat-knitted or woven fabrics[52]. Melt spinning is another promising technology that has been gaining prominence in recent years, and it allows continuous core-sheath triboelectric fiber production. Yet, only limited fiber diameters and structures can be produced with melt spinning compared to other methods. This limitation can affect the versatility of the process for specific applications[53]. Electrospinning is another novel technology that can produce continuous TENG fiber. However, the major obstacle to this process is the need for electrode deposition as a separate process[54].

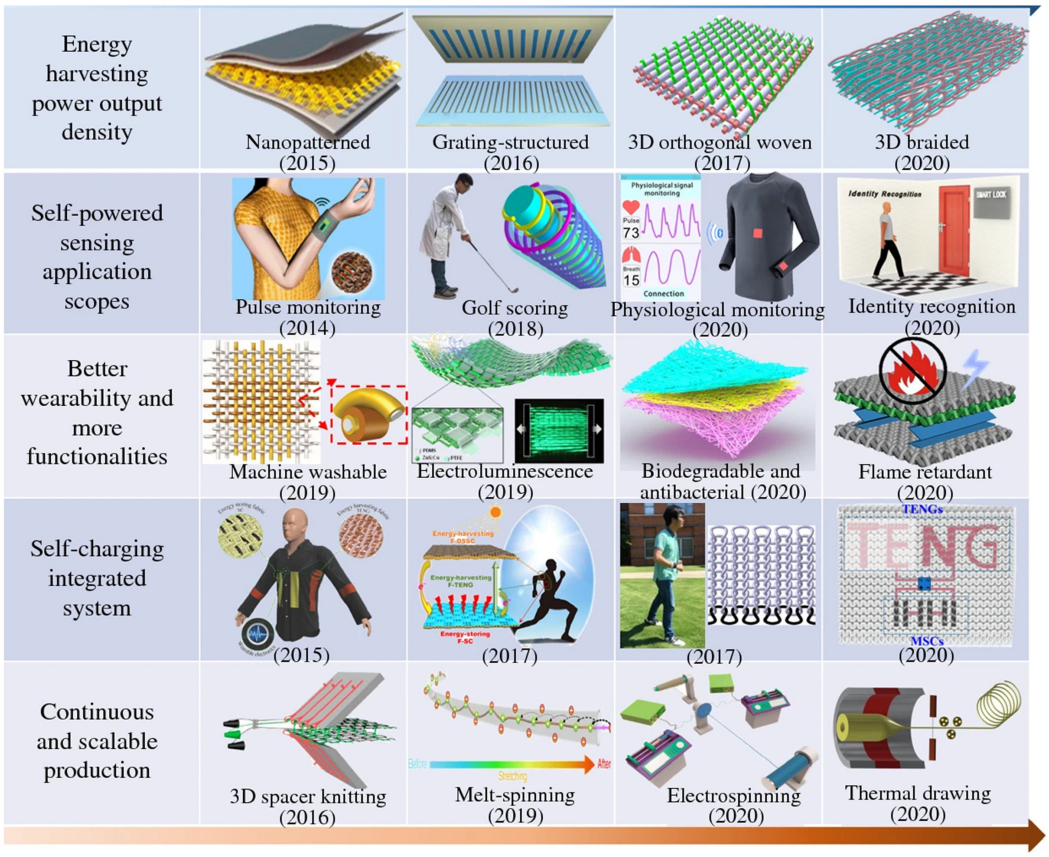

Figure 1.6: Recent development trend of TENG integrated with textile[7].(Reproduced with permission. Copyright © 2021, Springer.)

The thermal drawing process (TDP) has appeared as the most recent continuous TENG fiber fabrication technology to retain the design of a multi-material preform from the macroscopic level down to the microscopic and even nanoscopic length scales. Furthermore, TDP can address current challenges by co-drawing electrode and triboelectric material into kilometer-long fibers in a single draw, completing the process within a few hours when employing a suitable preform[55]. Thermal drawing, with its high precision, multi-material integration ability, versatility, industrial scale scalability, and cost-effectiveness, is envisioned to dominate over other production methods for continuous textile-grade TENGs manufacturing. However, the energy density produced by TENG fibers at the current state is still very low, hindering its widespread use with textiles. Low dimensional material integrated planner TENG devices have been reported to produce high

triboelectric power output. Even though research has been reported on 1D material (CNT, CNF), piezoceramics, and rod-shaped 1D nanomaterials, integration of low dimensional material integrated thermally drawn TENG is only limited to MXene[56, 57, 58]. This thesis aims to expand the library of thermally drawn low dimensional materials by integrating graphene nanoplatelet and MoS_2 with PVDF.

Chapter 2 of this thesis showcases an effective approach to improve electromechanical conversion efficiency by incorporating graphene nanoplatelets with PVDF TENG and employing thermal drawing to fabricate textile-compatible long-length triboelectric nanogenerator fibers. The flexible woven fabric structure demonstrates superior energy harvesting and sensing capability. These fibers exhibit stability in harsh environmental conditions, making them suitable for energy harvesting and biomotion analysis applications.

Chapter 3 demonstrates further improvement of the energy conversion efficiency of the PVDF TENG by incorporating bulk MoS_2 and subsequent thermal drawing to produce long-length nanocomposite TENG fiber. The chemical and electrical properties of the thermally drawn MoS_2- PVDF fibers are analyzed in detail. The superior sensitivity of the MoS_2-integrated TENG allows it to be implemented in self-powered respiration monitoring, biomotion sensing, and analysis.

Throughout the thesis, we have concentrated our work on the material perspective. We also analyzed the relation between nanoparticle concentration and corresponding triboelectric output to optimize the preferred concentration for TENG fiber applications. The sub-micrometer scale modification of PVDF using GNP and MoS_2 and subsequent demonstration of thermal drawing of triboelectric fiber represents the one of the initial explorations of large-scale fabrication of triboelctric fibers embedded with conductive and semi-conductive nanomaterials. This work may enable the study of PVDF's interactions with nanomaterials while emphasizing rheological considerations as a key factor in the single-step production of electronic textiles at an industrial scale. This research will drive the advancement of wearable and flexible electronics, offering lightweight, durable,

and high-performance materials for energy generation. Additionally, understanding the synergy between low dimensional materials and thermally drawn fibers will open new avenues for multifunctional textiles that will combine energy harvesting with other capabilities, such as sensing, communication, and actuation, thereby advancing the field of smart textiles and wearable technology.

Chapter 2

Graphene nanoplatelet integrated thermally drawn PVDF triboelectric nanocomposite fibers for biomotion sensing

[1]Triboelectric nanogenerators (TENGs) utilize the synergetic effect of triboelectrification and electrostatic induction to guide electrons through an external circuit, enabling low-frequency mechanical and biomechanical energy harvesting and self-powered sensing. Integrating low dimensional material with a high specific surface area into flexible ferroelectric polymers such as polyvinylidene difluoride (PVDF) has proven to be an efficient strategy to improve the performance of TENG devices. Scalable fabrication of graphene-integrated PVDF nanocomposite fiber using thermal drawing process has been demonstrated for the first time in this study. The open circuit voltage and short circuit current show 1.41 times and 1.48 times improvement with the integration of 5% graphene in the PVDF fibers, respectively. The TENG fabric shows a maximum power output of 32.14

[1]The work has been published in Advanced Electronic Materials (© 2023 Wiley-VCH GmbH) titled "Graphene Nanoplatelet Integrated Thermally Drawn PVDF Triboelectric Nanocomposite Fibers for Extreme Environmental Conditions". The author has taken appropriate permission to add the published work in the thesis.

μW at a matching load of 7 $M\Omega$ and a power density of 53.57 mWm^{-2}. The fibers exhibit excellent stability in harsh environmental conditions such as alkaline medium, high/low temperature, multi-washing cycle, and long-time usage.

2.1 Introduction

The progress in nanoscience and nanotechnology has led to significant advancements in flexible and wearable electronic sensors and equipment. The appeal of wearable devices and sensors stems from their potential applications across a broad spectrum of areas, including implants, prostheses, health monitoring, motion tracking, human-machine interaction, and artificial intelligence[59, 60, 61, 62]. The utilization of textiles and textile-based wearable devices holds particular significance due to their capability to gather substantial amounts of psychological data[63]. Several textile-based sensors have been reported for continuous monitoring, namely capacitive, piezoresistive, optical, and nanogenerator-based[42, 43, 64, 65, 66, 67, 68, 69, 70]. However, a key challenge for the sustainable application of wearable devices remains the necessity of low-profile power systems, which is particularly daunting in implanted and textile-based wearables to untether them from rigid and heavy power sources[71, 72]. In this respect, nanogenerator-based energy sources that work on several principles, including piezoelectric (PENG)[73], triboelectric (TENG)[74], thermoelectric (TEG)[75], magnetoelastic(MEG)[76] and electromagnetic (EMG)[77] are capable of harvesting mechanical motion eliminating the need of additional power source for the operation. TENGs are low-cost, lightweight, and highly efficient at low frequency compared to other nanogenerators[78].

Polyvinylidene difluoride (PVDF), one of the most widely used ferroelectric polymers, has distinctive polymorphs (α, β, γ, δ, and ϵ), and it stands out from other polymers due to its excellent flexibility, piezoelectric coefficient, electronegativity, spontaneous yet stable and tunable polarization, polarization stability, and high electron affinity[79]. These properties make PVDF an excellent candidate for usage in a triboelectric system[80, 81, 82]. Several methodologies have

been investigated to improve the triboelectric output of PVDF, including surface functionalization[83], ion injection[31], spontaneous polarization[84], addition of charge trapping interlayer[35], and dielectric constant increment[85]. The addition of low dimensional materials that provide charge-trapping sites is an effective way to tune composite materials' dielectric properties[8].

Low-dimensional materials are crystalline materials with strong covalent bonds that provide in-plane stability. Their weak interlayer interaction allows exfoliation to an atomically thin layer that exhibits exceptional electrical, optical, thermal, and mechanical properties[86]. Low dimensional materials such as transition metal dichalcogenides (TMDs), transitional metal carbides/nitrides (MXenes), graphene, and graphene oxide have been utilized for triboelectric nanogenerator due to their unique electronic properties[37]. Even though the power density of carbon-based TENGs is relatively lower than metal-based ones[37], graphene and its derivatives have attracted tremendous interest due to their high electrical conductivity, optical transparency, gas barrier property, robustness, flexibility, and environmental stability[87, 88, 89]. Moreover, graphene can store electrical charge for a considerable period, which is desired for increasing charge density in triboelectric materials[90, 91, 92].

Herein, we have demonstrated the scalable fabrication of graphene nanoplatelet (GNP) integrated thermally drawn PVDF nanocomposite fiber for the first time. A comprehensive study on the fabrication and characterization of GNP-PVDF under harsh environmental and wear conditions was performed. The addition of GNP and subsequent thermal draw of nanocomposite fiber improves the β phase transformation of PVDF upto 13% compared to unprocessed PVDF films, an indicative parameter for the potential of improved triboelectric performance. The fabric sensor exhibited a power density of 53.57 mWm^{-2}, and the open circuit voltage (V_{oc}) and short circuit current (I_{sc}) output increased to 1.41 and 1.48 times compared to pristine PVDF fiber, respectively. The fiber demonstrated stable output during multi-cycle heating, cooling, washing, and long-time usage.

2.2 Experimental Section

2.2.1 Chemicals and films

Polyvinylidene difluoride (PVDF) and Polycarbonate (PC) were purchased from Ajedium Films. Dimethylformamide (DMF) was purchased from Carlo Erba Reagents S.A.S. and DCM from Merck KGaA. Cotton yarn (60% Cotton and 40% Acrylic) was bought from local suppliers. Graphene Nanoplatelet (Purity: 99.9%, Size: 3 nm, S.A: 800 m^2/g, Dia: 1.5 μm) was purchased from Nanografi. Commercially available detergents were used for the washing test.

2.2.2 Sensor Fabrication

Sensor fabrication starts with the fabrication of nanocomposite film. 25 wt.% PVDF was dissolved in dimethylformamide (DMF) by constant mechanical stirring in the hot plate at 60°C for 1 hr. At the same time, graphene was subjected to ultrasonication in DMF solution for 1 hr. Afterward, the graphene- DMF solution was transferred to the PVDF solution and the mechanical stirring process continued for 7 hr. After that, the PVDF- graphene solution was cast onto a glass petridish and the DMF solution was evaporated by treating at 80°C for 8 hr. to get graphene-PVDF nanocomposite film of 1.%, 3.%, and 5.% concentrations. The electrode used for the fabrication was CPE in continuous film form. It was subjected to mechanical compression inside a mold at 170°C to get a cylindrical-shaped CPE rod of 12 mm. Then, PVDF nanocomposite film was rolled over the CPE to get the desired tribonegative layer in the preform stage. An additional sacrificial PC layer was rolled over the PVDF nanocomposite layer to ensure uniform thermal drawing. The final diameter of the preform was 15 mm without the PC layer and 25 mm with the PC layer. The prepared preform was annealed at 90°C in a vacuum for 24h. Then, it was consolidated using a three-stage process inside a custom-built furnace - i) annealing at 150°C in a vacuum for 2hr, ii) consolidating at 190°C for 45 min and iii) subsequent cooling at room temperature.

Fiber draw was carried out in a custom-built thermal draw tower at 240°C. At the same time, applying controlled tension by capstone pulling ensured uniform diameter enabling continuous draw of tens of meters of fiber. Later, the PC sacrificial layer was dissolved in DCM to get graphene-integrated PVDF TENG fiber. The fabric sensor was woven together with cotton yarn using a handloom.

2.2.3 Materials Characterization

The morphological structure of the fiber was investigated using FEI QUANTA 200F field emission SEM. FTIR spectroscopy was performed using Bruker alpha Platinum-ATR FTIR 256 scan steps with a scan resolution of $0.5cm^{-1}$. Laser DIC images were taken using Keyence VK-X100 3D Laser Scanning Confocal Microscope. The XRD analysis was performed with Pananalytical X'pert Pro XRD using Cu $K\alpha$ radiation. Raman spectroscopy was performed using WITec α300RSplus.

2.2.4 Electrical Characterization

For the electrical measurement of the drawn fiber, 12 cm of fiber was cut, and 2 cm of the electrode was exposed and wrapped with conductive tape. Open circuit voltage was measured in a single electrode (SE) set up using an oscilloscope (Agilent Technologies DSO1014A) and short circuit current was measured using a low noise current preamplifier (Stanford Research Systems SR570). A custom-made tapping device of varied contact areas (2/4/6/8 cm^2) was used for cycling tapping.

2.2.5 High-Temperature Electrical Characterization

The 12 cm cut length of PVDF-graphene TENG fiber was placed over a hot plate inside a closed chamber to characterize TENG fiber at elevated temperature.

Each fiber was allowed to be heated for two hours before the measurement. A small custom-made tapping device of contact area (2 cm^2) was used, which was powered by a Waveform generator (Agilent 33210A).

2.2.6 Durability test

To test the washability of fiber, a 12 cm long PGr-5 TENG fiber was cut, immersed in a 0.5% commercial detergent solution, and subjected to continuous stirring at 60°C for 2hr. Then, the fiber was removed from the solution, rinsed in DI water twice, followed by drying in the oven for 10 min, and then its output voltage was measured. The cycle continues for five more times. Further, the fabric sensor is subjected to high-speed rotation-induced stress inside a washing machine (Arcelik 7100 M, at 1000 rpm and 60°C). After that, the fabric sensor was rinsed in DI water twice, dried in an oven at 75°C for 1 hr, and the output voltage was measured. The cycle was repeated five more times.

Fiber durability against salt water was tested at room temperature by immersing the fiber in 4% salt solution (4 gm table salt in 100 ml DI water). The fiber was rinsed three times with DI water and dried before measuring the V_{oc} output after immersion.

The cooling cycle was performed by cooling the fiber in -80°C refrigerator. After cooling, the fiber was allowed to relax at room temperature for 10 min, and output voltage was measured.

The heating cycle was conducted by keeping the sample inside a furnace at 100°C. After heating, the fiber was allowed to relax at room temperature for 10 min, and output voltage was measured.

2.2.7 Surface Roughness Measurement

The surface roughness of the triboelectric fiber was measured using Keyence VK-X100 3D Laser Scanning Microscope. The surface images were taken using 0.01 z pitch at 100x focus. Area roughness was measured using a cut-off value λc of $0.25mm$ (selecting of individual measuring paths/cut-off according to DIN EN ISO 4288 periodic table).

2.3 Fabrication of Triboelectric Fibers

Figure 2.1 a, b shows a detailed schematic for fabricating triboelectric nanocomposite film and fiber. First, PVDF sheets were dissolved into dimethylformamide (DMF) by continuous stirring on a hot plate, and an ultrasonicated GNP-DMF solution was added to the PVDF-DMF solution. The stirring was continued until a uniform GNP-PVDF nanocomposite solution was obtained. The solution was then cast on a glass plate, and DMF was allowed to evaporate to form a GNP-PVDF nanocomposite film. The dry film was peeled off from the glass plate and rolled over a CPE rod (prepared by hot pressing). Finally, a sacrificial PC layer was rolled over the tribo-negative layer to assist during the thermal drawing. By this process, four separate fibers were prepared for comparative study - PVDF fiber without GNP, 1% GNP-PVDF fiber (PGr-1), 3% GNP-PVDF fiber (PGr-3), and 5% GNP-PVDF fiber (PGr-5). This method promotes the electroactive phase transition of α phase to β phase, enhancing triboelectric charge generation[93].

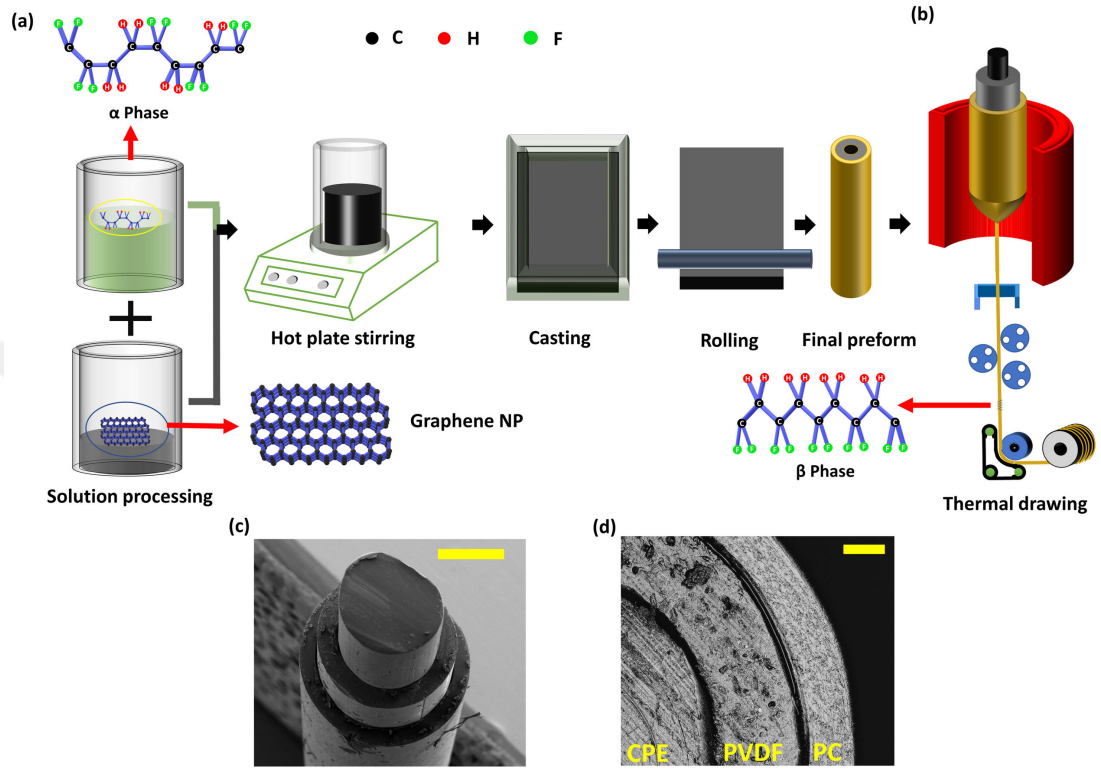

Figure 2.1: Fabrication procedure for GNP-PVDF triboelectric fiber. (a) Solution processing of GNP and PVDF to produce a dry nanocomposite film. (b) Schematic of the thermal drawing process for continuous TENG fiber. Fiber cross sectional image. (c) SEM image of the drawn fiber. Scale bar: 500 μm. (d) LSCM image of the drawn fiber's cross-section. Scale bar: 100 μm.

In the TDP, a macroscale preform is drawn to a long-length fiber at elevated temperature by axial stress application[94, 95]. The diameter of the fiber is governed by the feed speed, drawing speed, and preform dia, which is expressed by the following equation[94]:

$$D_{\text{fiber}} = D_{\text{preform}} \sqrt{\frac{v_{\text{feed}}}{v_{\text{draw}}}} \tag{2.1}$$

where v_{feed} is the feed speed and v_{draw} is the drawing speed. Complex shear viscosity, storage modulus, and loss modulus are the important criteria during

the multi-material thermal draw[96].

Complex shear viscosity (η^*) is a rheological attribute of a material that describes the relation of stress to strain rate in viscoelastic fluid in the case of oscillatory shear stress[97]. A material's elastic behavior is presented by storage modulus (G'), described as the ability of a material to store and recover energy during deformation. On the other hand, the material's viscous behavior is expressed by loss modulus (G") and described as the material's ability to dissipate energy during deformation. For thermoplastic polymers, G' dominates over G" at room temperature. A stable draw can be achieved in the vicinity of a temperature range where the G" slowly increases with the increase of temperature and the G' decreases rapidly[49]. Thus, choosing a material with similar glass transition temperature and comparable complex share viscosity is essential for the multi-material thermal draw.

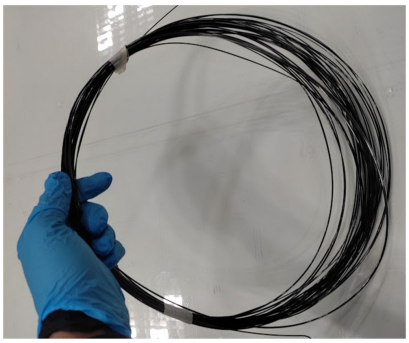

Figure 2.2: Continuously drawn long-length nanocomposite fiber.

Moreover, multi-material fiber draw experience axial and radial velocity mismatches due to the parabolic temperature field experienced by preform in the radial direction during thermal drawing, which tends to disrupt uniform flow profile[98]. Thus, the drawing temperature was needed to be optimized. For this drawing, optimum fiber draw parameters were determined at 240°C and 80 g tension, facilitating mostly uniform fiber draw. This process made it possible to continuously draw tens of meters long fiber (Figure 2.2). The scanning electron microscope (SEM) and laser scanning confocal microscope (LSCM) image of the

fiber showed the presence of a three-layer structure of the preform: CPE core (650 μm), GNP-PVDF nanocomposite (diameter 970 μm, thickness 160 μm) and PC (diameter 1170 μm, thickness 100 μm) (Figure 2.1c, d).

2.4 Materials Characterization

Raman spectroscopy is used to acquire information about the vibrational modes of a molecule[99]. It is an effective tool for determining carbon-based material's D-band, G-band, and 2D band[100]. Raman spectroscopy of GNP proved the presence of D band, G band, and 2D band, respectively, for wavenumbers 1350cm^{-1}, 1570cm^{-1}, and 2700cm^{-1} (Figure 2.3). The presence of the G band and 2D band confirmed the presence of graphene[101, 102].

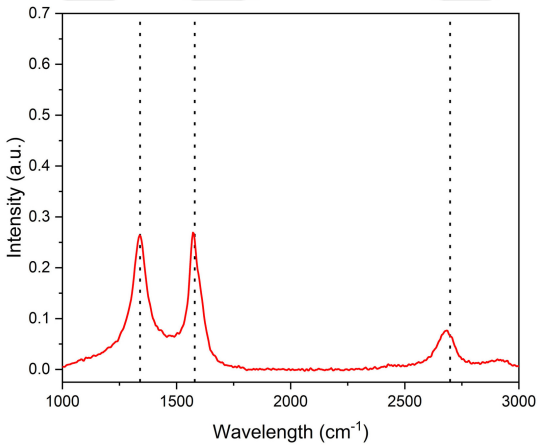

Figure 2.3: Raman spectra of multilayered GNP.

Additionally, it was possible determine multi-layred nature of GNP by analyzing the I_{2d} and I_g peaks. The intensity ratio of I_{2d} and I_g decreases with the increase of layer number[103]. $I_{2d}/\ I_g$ for single-layer GNP is 3.3; its value is 0.5 for seven-layer GNP[103]. The $I_{2d}/\ I_g$ value obtained was 0.29, proving the multilayer GNP structure's presence. The characteristic peaks of the three crystal phases of PVDF (α, β, and γ) in FTIR spectra were detected as α phase

peaks at 763,795, 854, and 870cm^{-1}, insignificant β phase peaks at 510, 840, and 1234$cm^{-1}$and γ phase peaks at 833 and 1279cm^{-1} (Figure 2.4)[104].

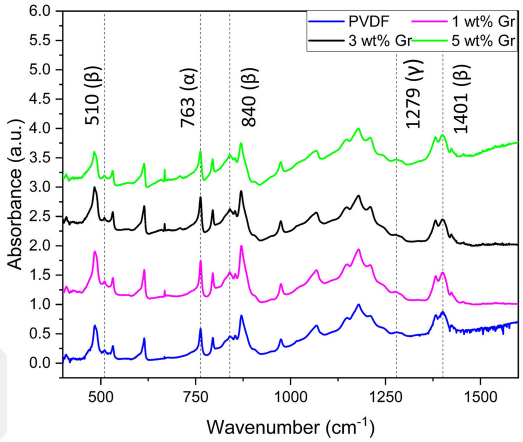

Figure 2.4: Material characterization of thermally drawn fibers. FTIR spectra of the PVDF fiber and GNP-PVDF nanocomposite fibers with various wt.%

Post thermal drawing FTIR spectroscopy of the pure PVDF fiber to PVDF nanocomposite fibers of varied concentration demonstrated a decrease of α peak intensity and an increase of β peak intensity, manifesting the transition of α phase to β phase. β phase can be calculated using the following formula[105]:

$$F(\beta) = \frac{A(\beta)}{\left(\frac{K(\beta)}{K(\alpha)}\right) A(\alpha) + A(\beta)} \tag{2.2}$$

where $F(\beta)$ represents the relative fraction of β phase content; $A\alpha$ and $A\beta$ are the absorbance at 763 and 840cm^{-1}, which are associated with non-polar α phase and electroactive β phase, respectively; $K\alpha$ (6.1×10^4 cm^2 mol^{-1}) and $K\beta$ (7.7×10^4 cm^2 mol^{-1}) are the absorption coefficients at the respective wavenumbers. The β phase is calculated in the commercially available PVDF film as 30% (Figure 2.5).

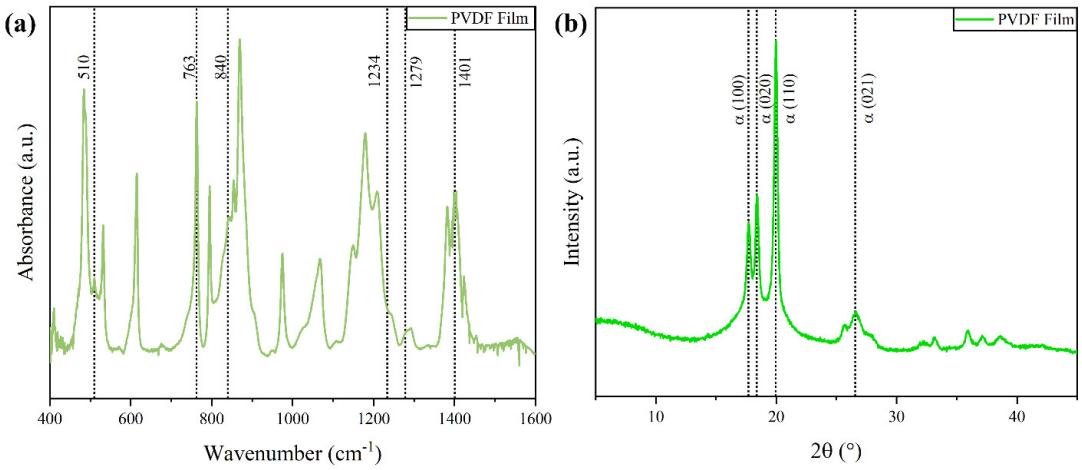

Figure 2.5: (a) FTIR and (b) XRD spectra of PVDF film[8].

After the thermal drawing of only PVDF-TENG fiber, the β phase increased to 35%. This 5% increment can be attributed to thermal drawing at 80 gm-wt drawing tension[106]. However, β phases of thermally drawn nanocomposite fibers demonstrated significant improvement and were increased to 37.6%, 39.5%, and 43.3% for PGr-1, 3, 5% TENG fibers, respectively. The additional contribution of the β phase increment directly came from the addition of GNP at different concentrations[107]. β phase transition in polymer melt occurs due to the application of tensile stress as higher tensile stress promotes chain re-orientation from α phase to the electroactive β phase of PVDF. Higher tensile stress induces higher β-phase content[108]. Further increment of the β phase is restricted due to the polymeric material's viscoelastic nature, which changes nonlinearly with increasing applied stress[109]. Each component's viscosity must be comparable at optimum drawing parameters for multilateral thermal drawing. At very high drawing stress, viscosity changes rapidly, resulting in discontinuous thermal drawing hampering the continuous long-length TENG fabrication at our desired fiber diameter.

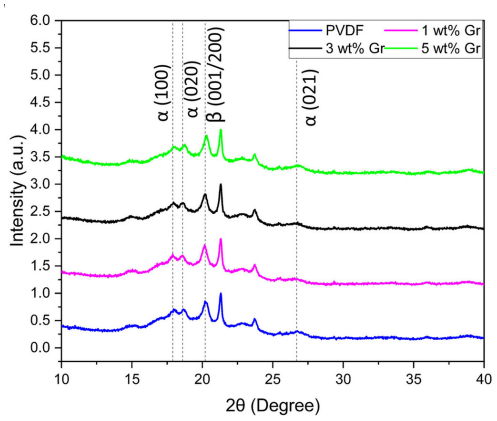

Figure 2.6: Material characterization of thermally drawn fibers. XRD spectra of the PVDF fiber and GNP-PVDF nanocomposite fibers with various wt.%

Moreover, XRD spectra of α phase PVDF locates at diffraction angles: 2θ = 17.7°, 18.3°, 19.9°, and 26.5°, corresponding to the (100), (020), (110), and (021) planes while high polarity β phase demonstrated peak diffraction angle 2θ = 20.2° corresponding to 110/200 plane[110]. The intensity of the α phase peaks showed a decreasing trend with the increased GNP percentage. On the contrary, the intensity of the β phase peak at 2θ = 20.2° increased with the addition of GNP (Figure 2.6). Even though, both FTIR and XRD proved the increment of the β phase, the α phase does not diminish completely as it is the most stable phase with the lowest free energy[111]. Thus, it coexists with an increased β phase percentage. Adding low-dimensional material like GNP acts as a nucleating agent, which assists the formation of the β phase during solution casting without any chemical modification or functionalization[107, 112]. During the ultrasonication and magnetic stirring process, localization of static charge occurs on the GNP surface. Due to this static charge generation, a weak electrostatic attraction occurs between the PVDF and GNP. This interaction re-orients the polymer chain of PVDF into a more crystalline structure by converting to β phase[112]. Evaporation of the solvent induces a polarization-locking effect, which prohibits the spontaneous regeneration of α phase from β phase[113, 114]. Furthermore, the thermal drawing of PVDF below its melting temperature exerts uniaxial stress on the polymer chain, aligning it towards the direction of the polymer flow, which

increases the degree of crystallinity and assists in conversion to the α phase[115].

Lastly, surface roughness also assists in triboelectric charge generation. Since triboelectrification is a phenomenon induced by physical contact between two surfaces, contact mechanics between two materials interface affects the generation of tribo charges[116]. Depending on the surface energy and material's mechanical properties, surface roughness can increase or decrease triboelectric output[117]. The real contact area between two materials can be maximized when a soft material is pressed against another soft material (Figure 2.7).

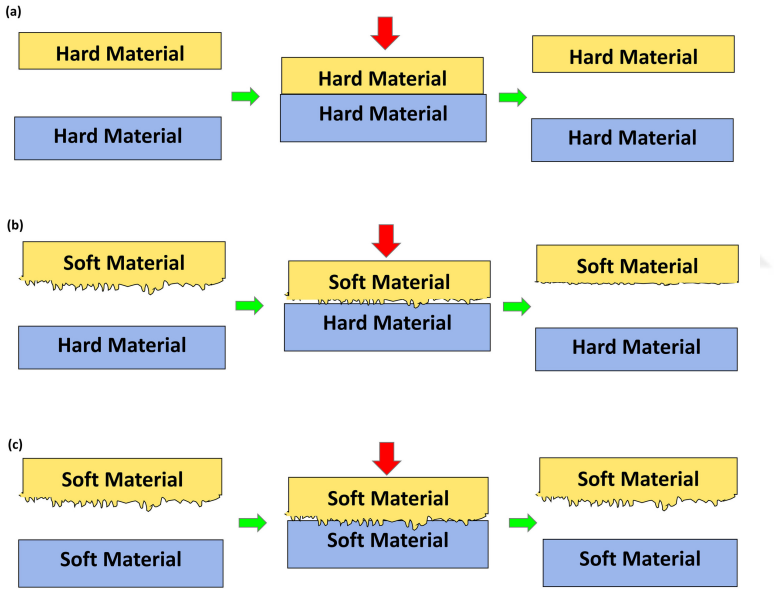

Figure 2.7: Contact area maximization due to surface roughness. (a) Contact between two flat hard surfaces. No increment of real contact area occurs. (b) Contact between a hard-flat surface and a soft-rough surface. A decrease in real contact area occurs due to the flattening of the soft, rough surface. (c) Contact between a soft flat surface and a soft-rough surface. An increase in the real contact area occurs.

In the case of our system, PEI and PVDF are soft and flexible polymeric materials (Young's modulus $\approx$ 3 GPa) that allow an increase of triboelectric output with the increase of surface roughness due to the increment of real contact area[118, 119]. Furthermore, the surface profile was measured for pure PVDF and

PGr-5 fibers along the fiber's longitudinal axis by the maximum height of profile (Rz) and arithmetical mean height (Ra), (Figure 2.7 a, b)[120].

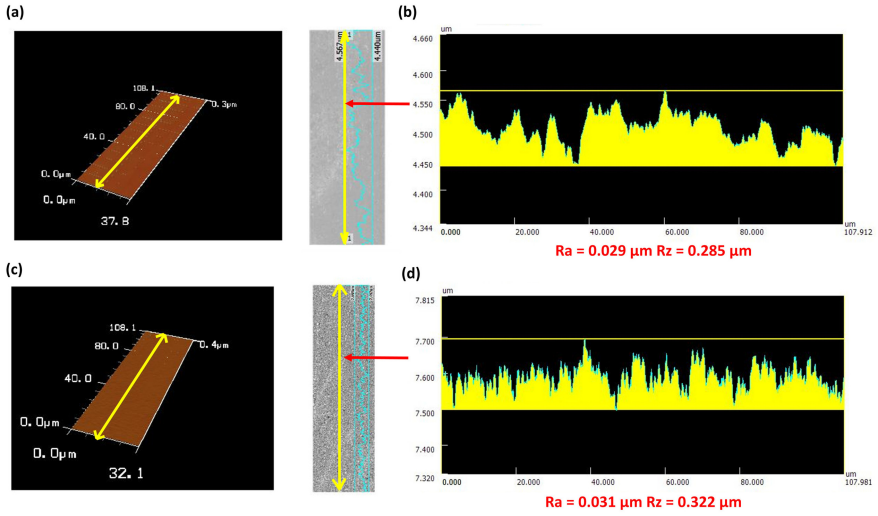

Figure 2.8: Surface profile and surface roughness measurement. (a) and (b) surface profiles of pure PVDF fiber. (c) and (d) surface profiles of PGr-5 fiber.

Pure PVDF fiber demonstrated Ra= 0.029 μm, Rz = 0.285 μm while PGr - 5 demonstrated increased surface roughness (Ra = 0.031 μm and Rz = 0.322 μm) (Figure 2.7 c, d). LSCM imaging of the pure PVDF fiber and PGr-5 further demonstrated the increased surface roughness as well as uniform distribution of GNP at the surface of PGr-5 fiber (Figure 2.8,2.9).

2.5 Electrical Characterization

The working mechanism of the fabricated TENG fiber was based on the fundamental single electrode (SE) mode, and the coupling effect of contact charging and electrostatic induction produces the output[121]. In this SE mode, only one triboelectric layer is directly in contact with the electrode, leaving the opposite layer free. The contact and separation between two layers create an electrostatic imbalance that induces charge exchange between the ground and the electrode[122].

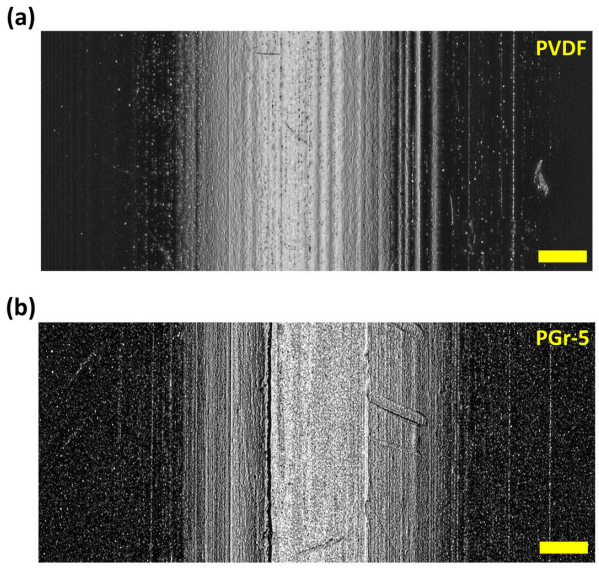

Figure 2.9: LSCM surface images of pure PVDF fiber and PGr-5 fiber. Scale bar 50 μm.

At the initial state (non-contact state), the system is in a balanced state, i.e., there is no charge transfer between PEI and PVDF and no potential difference generated between electrode and ground (Figure 2.10a-i). When PEI comes in contact with PVDF due to external mechanical force, charge transfer occurs between two materials depending on their triboelectric polarities[123]. Electrons from PEI get injected into PVDF, creating a net negative charge on PVDF and a net positive charge on the PEI surface. As the two opposite charge is confined to the surface at the compressed stage, it resulted in a net zero electrical potential difference. Thus, the system is still balanced state as the PEI carries a positive charge and PVDF carries the same amount of negative charge (Figure 2.10a-ii). Polymeric materials are also insulators, and can retain the charge for a long time[124]. However, as the separation between PEI starts to take place, V_{oc} starts to increase until it reaches a maximum value. Thus, the electrostatic balance of the system breaks and a potential difference is created under the open circuit condition, which triggers instantaneous electron flow from CPE to the ground due to electrostatic induction (Figure 2.10a-iii). After, electron is released from

CPE, electrostatic balance is established and no electron flow is observed at this stage (Figure 2.10a-iv).

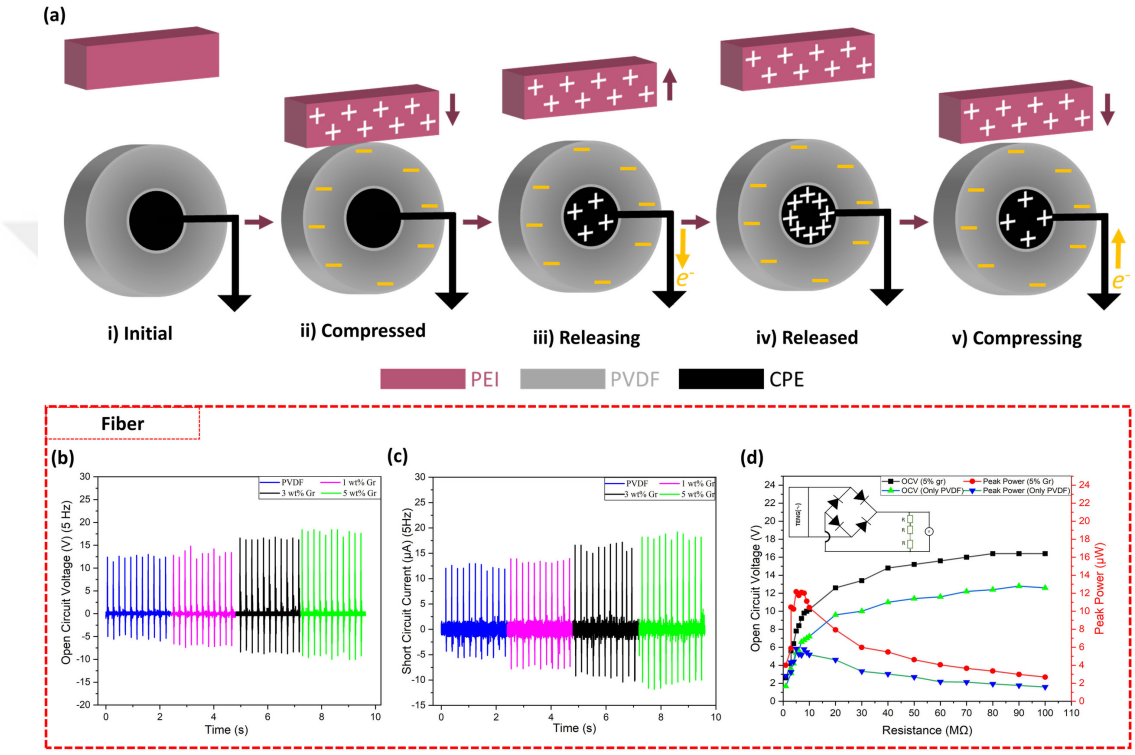

Figure 2.10: Electrical characterization of thermally drawn TENG fiber. (a) Working principle of a single electrode (SE mode) TENG fiber. (b) Open circuit voltage (V_{oc}) and (c) Short circuit current (I_{sc}) of pristine and PGr-(1-5%) TENG fiber (contact length: 3 cm and frequency: 5 Hz). (d) Peak power output for PGr-5 fiber and only PVDF fiber with equivalent circuit connection for measuring power output.

Next, the top PEI starts to lower again towards the PVDF surface, and as a result, equilibrium is lost again as the primary electrode possesses a lower electrical potential. Thus, electron will move back from ground to electrode producing instantaneous current from opposite direction (Figure 2.10a-v). When two-layer touches again, electrostatic equilibrium is re-established. By the nature of electron flow in two opposite direction, an AC signal is generated after the completion of one contact separation cycle.

Electrical characterization was carried out using a custom-made tapping device, an oscilloscope and a current preamplifier (Figure A.1). The output of a TENG can vary depending on the materials, contact area, and the frequency of the applied mechanical motion[125]. Figure 2.10b, c represent V_{oc} and I_{sc} for PVDF fiber with different GNP concentrations at a 3 cm contact area a 5 Hz frequency. PGr-5 fiber demonstrated V_{oc} up to 18.4 V, which was 1.41 times higher than pure PVDF fiber (V_{oc} for PVDF only fiber is up to 13 V). PGr-1 and PGr-3 showed similar trends increasing V_{oc} up to 1.13 and 1.29 times, respectively. I_{sc} also presented a similar trend by increasing 1.09, 1.34, and 1.48 times for PGr-1, 3, and 5, respectively. Figure 2.10d represents the peak power output of PGr-5 and pure PVDF TENG fibers when subject to tapping at 5 Hz with a 3 cm contact area. The PGr-5 fiber showed a peak power of 12 μW, which is 2.08 times higher than pure PVDF fiber. Several factors contribute to the increase of the triboelectric output for an increased percentage of GNP. The following equations gives the open circuit voltage (V_{oc}), short circuit current (I_{sc}) and short circuit charge transfer (I_{sc}) by this cyclic contact separation process[126]:

$$V_{\mathrm{OC}} = \frac{\sigma S}{2C_0} \tag{2.3}$$

$$Q_{\mathrm{SC}} = \frac{\sigma S}{2} \tag{2.4}$$

$$I_{\mathrm{SC}} = \frac{dQ}{dt} \tag{2.5}$$

where σ is the average surface charge density of the materials, S is the contact area of the device, and C_0 is capacitance using vacuum as the dielectric[127]. Equation (3) and (4) reveal the dependency of the triboelectric output on contact area and surface charge density. Moreover, the charge density of the surface depends on the capacitance and the dielectric property of the functional surface and is expressed as follows[128]:

$$\sigma = \frac{CV}{S} = \frac{\varepsilon_0 \varepsilon_r V}{t} \tag{2.6}$$

$$C = \frac{\varepsilon_0 \varepsilon_r S}{t} \tag{2.7}$$

Here, C is the capacitance, ϵ_0 is the permittivity of the vacuum, ϵ_r is the relative permittivity, V is the fiber's surface potential, and t is the thickness of the fiber. Thus, the performance enhancement of a TENG depends on improving the functional surface's capacitive property, dielectric property, and surface charge density. Pure PVDF only facilitates electron displacement polarization and dipole orientation polarization. However, along with electron displacement and dipole orientation polarization, the GNP-PVDF nanocomposite also demonstrates the enhancement of the interfacial polarization, further increasing the composite's dielectric property[118]. Evenly dispersed GNP in PVDF matrix forms micro capacitor where the electroactive β phase of PVDF is sandwiched between parallel GNP layers forming a parallel plate capacitor setup (Figure 2.11)[118, 129, 130].

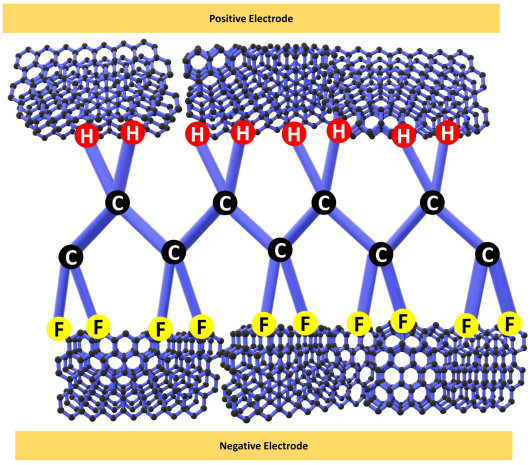

Figure 2.11: Micro-capacitor formation due to interaction between GNP and PVDF enhancing electron trapping.

Furthermore, surface charge density in a TENG device is determined by the combined effect of surface charge generation and charge decay. Charge decay

can occur in three modes: air breakdown, triboelectric charge drift, and diffusion (Figure 2.12)[131]. Air breakdown occurs when the triboelectric layer surface is discharged due to interaction with N_2 gas in the air, which renders them ionized[132]. Triboelectric charge drift occurs when surface charge follows the electric field created between positive and negative surfaces which promotes triboelectric charge to escape the negative surface and get neutralized. Lastly, charge diffusion occurs due to the electron concentration gradient. Thus, electrons diffuse into the bottom electrode[133]]. Stable output is observed when a dynamic equilibrium is reached through the simultaneous effect of charge generation and decay[131]. The micro capacitors in GNP-PVDF nanocomposite acts as a charge trapping site which improves the capacitive property and surface charge density[134]. Furthermore, the highest occupied molecular orbital (HOMO) and lowest unoccupied molecular orbital (LUMO) levels also affect triboelectric output. Deformation of molecular orbital (lowering LUMO energy level) can increase triboelectric output as it improves the electron-accepting ability of the material by facilitating electrons in a lower energy state[135]. Graphene and graphene-based materials are known to decrease LUMO energy levels in Gr-PVDF nanocomposite materials[136].

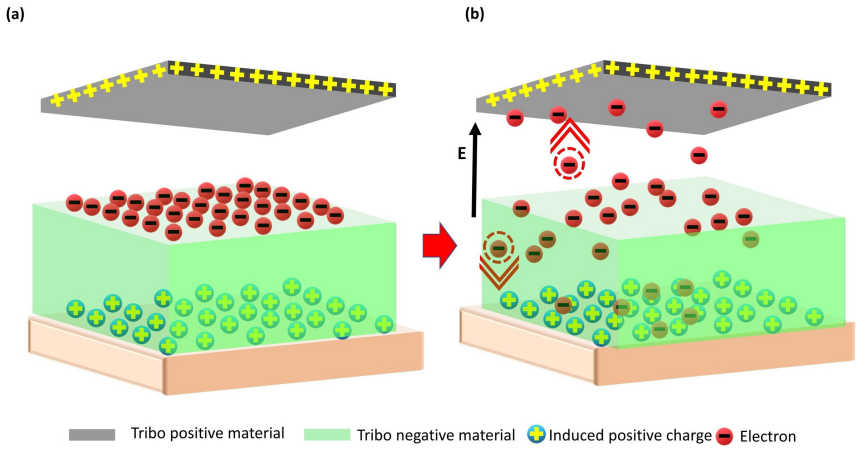

Figure 2.12: Charge decay in a tribonegative surface. (a) Generation of negative charge in tribonegative surface. (b) Depletion of charge density due to charge decay.

Figure 2.13, represents the V_{oc} and I_{sc} for PGr-5 fiber for different contact lengths at 5 Hz frequency. For 1 cm contact length, the output voltage reached 10.2 V. With the increase of contact area, output voltage increased successively and reached 23.2 V for a contact length of 4 cm. I_{sc} followed a similar trend increasing from 11.6 μA for 1 cm contact length to 23.6 μA for a contact length of 4 cm. Contact area determines the amount of charge transferred between two materials. An increase in contact area increases the charge density by increasing the total amount of charge transfer between two materials[137].

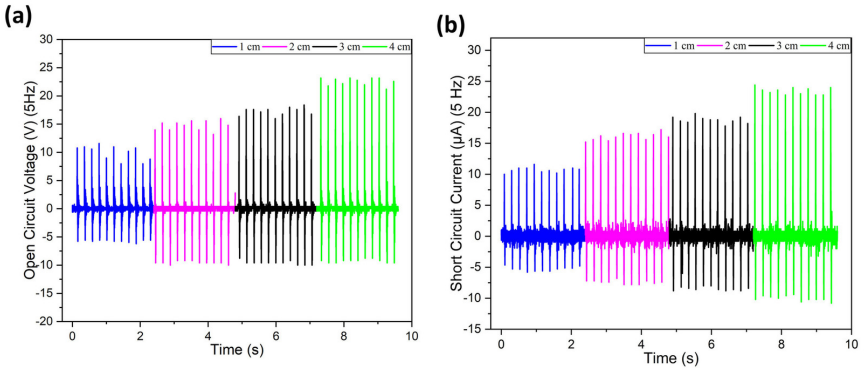

Figure 2.13: (a) Output voltage V_{oc} and (b) current I_{sc} of PGr-5 TENG fiber at varied contact lengths (1-4 cm) at 5 Hz frequency.

The effect of contact frequency on triboelectric output is shown in Figure 2.14.

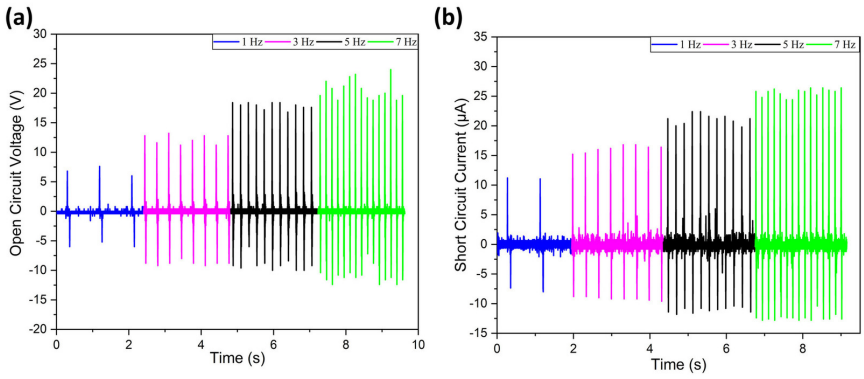

Figure 2.14: (a) Output voltage V_{oc} and (b) current I_{sc} of PGr-5 fiber TENG at varied frequencies (1, 3, 5, and 7 Hz) with a 3 cm contact length.

For PGr-5, V_{oc} was observed at 7.6 V for 1 Hz tapping frequency with 3 cm contact length. With increased tapping frequency, output voltage increased successively, demonstrating a value of 24 V at 7 Hz frequency. I_{sc} also followed a similar trend with an output current of 26.4 μA at 7 Hz. A faster contact separation cycle enhances triboelectric charge density during a high-frequency tapping cycle by keeping high surface charge density as it allows lower charge decay time. On the contrary, lower contact frequency leads to increased charge decay during the contact separation cycle, which affects the total triboelectric output. The overall performance of the fiber indicated its potential in self-powered sensing and energy harvesting due to human motion.

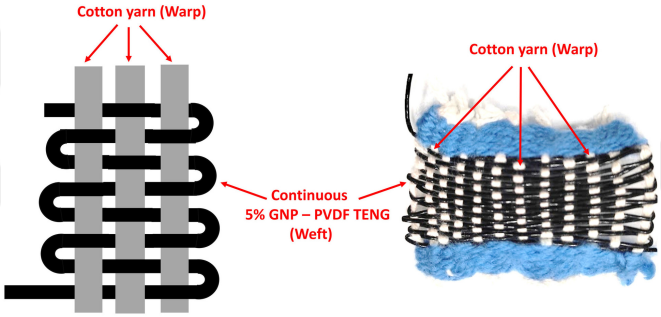

Figure 2.15: Construction of plain-woven fabric. Cotton warp placed in the warp direction and continuous PGr-5 TENG fiber in the weft direction.

Flexible TENG fibers have the potential to be integrated directly to the clothes through weaving, knitting or braiding process for continuous monitoring of human motion and harvesting energy generated during human motion. For the quantitative assessment on the sensing and energy harvesting capability of the fabricated PGr-5 TENG fiber, 1 meter of TENG fiber was weaved into a hybrid cotton-synthetic fabric structure where cotton yarn was used as the warp yarn and continuous TENG fiber was employed as a weft yarn to make a 5×2 cm^2 woven plain fabric structure (Figure 2.15).

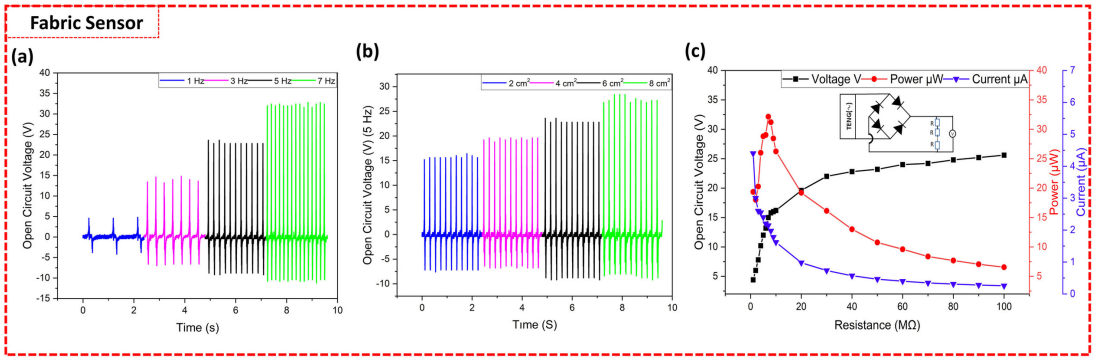

Figure 2.16: Electrical characterization of thermally drawn TENG fabric. (a) V_{oc} of PGr-5 TENG fabric at varied frequencies (1, 3, 5, and 7 Hz) with a 3 cm contact length. (b) V_{oc} of PGr-5 TENG fabric at varied contact areas at 5 Hz frequency. (c) The power output of PGr-5.

Figure 2.16a and 2.17a, demonstrate the fabricated sensor's V_{oc} and I_{sc} waveform with different contact frequencies. With the increasing frequency, the V_{oc} increased from 4.8 V for 1 Hz to 32.8 V for 7 Hz, while I_{sc} followed a similar trend and increased up to 36 μA for 7 Hz frequency. An increase in contact area also increases V_{oc} and I_{sc}. For the 2 cm^2 contact area, the V_{oc} and I_{sc} were 16 V and 16.4 μA, respectively while for an increase in contact area up to 8 cm^2, the V_{oc} and I_{sc} increased to 28.4 V and 30 μA, respectively (Figure 2.16 b and 2.17b). The output power of the Fabric TENG was investigated by varying the load resistance in series from 1 $M\Omega$ to 100 $M\Omega$. The output power of the fabric sensor can be calculated as $P = V^2/R$. Considering the inherent capacitive behavior of the sensor, the power output can be represented as[55]:

$$P = \frac{V_{\mathrm{OC}}^2 R_L}{|Z_C|^2 + R_L^2} \tag{2.8}$$

Here, Z_c is the magnitude of its internal impedance. Peak power is achieved in matching load conditions. Maximum power of 32.14 μW was obtained at a matching load of 7 $M\Omega$. Thus, the impedance of the fabric sensor was estimated to be 7 $M\Omega$ (Figure 2.16c).

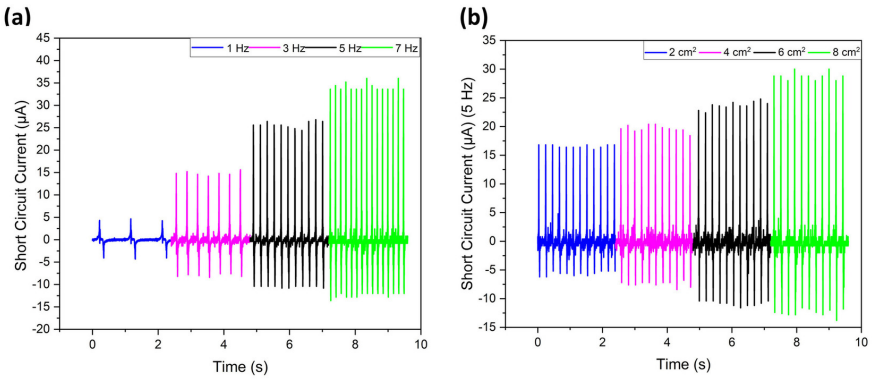

Figure 2.17: (a) I_{sc} of PGr-5 TENG fabric at varied frequencies (1, 3, 5, and 7 Hz) with 3 cm contact length (b) I_{sc} of PGr-5 TENG fabric at varied contact area (2,4,6 and 8cm2) at 5 Hz frequency.

Regarding the variation of contact frequency and contact area, fabric TENG followed an output trend similar to fiber, as evident in electrical characterization. However, the increment of contact total area does not result in a proportional increase of triboelectric output of fabric as compared to fiber. The marginal performance improvement of the devised TENG fiber occurred due to increasing the total continuous fiber length for fabric TENG, which also increased the equivalent series resistance of the electrode, as evident by Ohm's law[138]. Thus, the effect of contact area increase on triboelectric output is suppressed. This shortcoming can be addressed by attaching short lengths of TENG fiber in an equivalent parallel circuit. However, it will diminish the advantages of scalability, a significant advantage of the TDP. One method of performance improvement of the polymer electrode can be adopted using highly conductive filler materials. Metallic and carbon-based materials are widely used to impart conductive properties on polymer electrodes. Metallic fillers are reported to demonstrate higher conductivity compared to carbon-based materials[139]. Thus, integrating metallic nanomaterials can significantly improve the performance of the electrode. Another approach can be considered using a highly conductive core by convergence drawing of metal wires that will limit the flexibility of the fiber[140]. Lastly, liquid metal can be an option for an ideal core material to preserve the fiber's flexibility. However, liquid metals may need supercooling to maintain their liquid state over the entire

service temperature range[141].

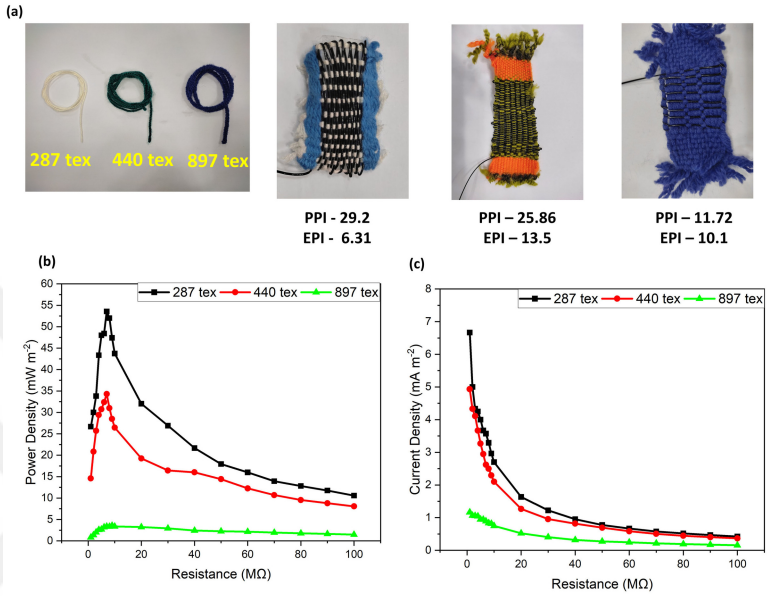

Figure 2.18: (a) Prepared fabric with varied cotton yarn thickness. (b) Power density and (c) current density of TENG fabric prepared from varied cotton yarn thickness.

Next, to quantify the effect of support warp yarn's thickness on tribo electric output, three fabric sensors were fabricated with three different support yarns (287, 440, and 897 *tex*) (Figure 2.18a). With the increasing thickness of the warp yarn, the power density and current density of the fabric TENG decreased rapidly. TENG fabric with 287 *tex* warp yarn showed a peak current density of 6.67 mAm^{-2} and a power density of 53.57 mWm^{-2}. These values decreased successively with increasing cotton thickness and reached a peak current density of 1.16 mAm^{-2} and power density of 3.36 mWm^{-2} for 897 *tex* warp (Figure 2.18b and 2.18c). The power output also decreased with increasing warp yarn thickness (Figure 2.19). This occurred due to the fact that increasing cotton yarn thickness resulted in wider spacing between warp and weft thread, decreasing picks per inch (PPI) that describes the number of weft threads per inch of woven fabric[142].The ratio of PPI to EPI for fabric woven with 287 *tex* yarn was 4.62. But, this ratio dropped to 1.16 for fabric woven with 897 *tex* cotton yarn. This effectively

reduced the triboelectric output by decreasing the total available contact area.

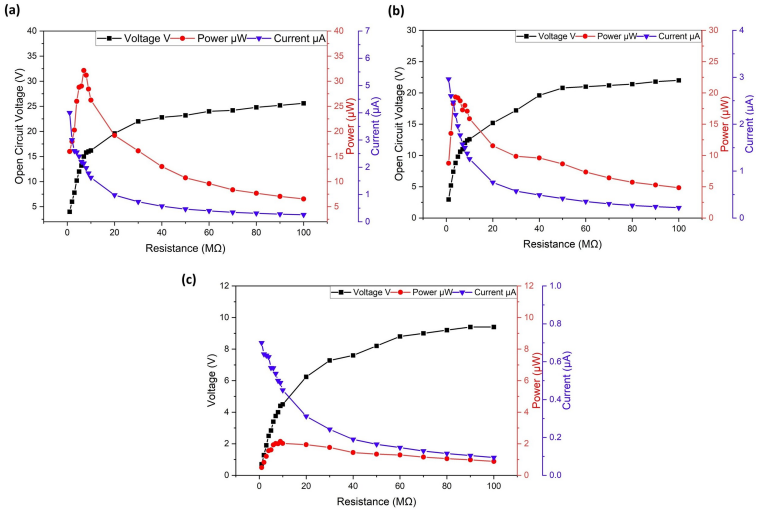

Figure 2.19: Power output for fabric sensor prepared with (a) 287 *tex*, (b) 440 *tex* and (c) 897 *tex* cotton warp.

Table 2.1: Summary of the performance of textile based TENGs (single electrode mode).

Structure	Power output	Load resistance	Reference
Single fiber	53.57 mWm^{-2}	7 MΩ	This work
Single fiber	40.8 mWm^{-2}	8 MΩ	2023[8]
Core-shell	15.8 mWm^{-2}	70 MΩ	2021[143]
Single fiber	40mWm^{-2}	300 MΩ	2021[144]
Single fiber	15.59 mWm^{-2}	80 MΩ	2021[145]
Core-shell	25 μWm^{-1}	400 MΩ	2021[146]
Core-sheath	44 mWm^{-2}	60 MΩ	2022[147]
Core-sheath	12.5 μWm^{-1}	20 MΩ	2019[53]
Coaxial	1.12 μW	100 MΩ	2018[148]
Single fiber	8.43 mWm^{-2}	1 GΩ	2018[149]
Core-shell	60 mWm^{-2}	200 MΩ	2017[150]

2.6 Durability Test

Throughout its lifetime, a textile TENG sensor may need to undergo thousands of tapping cycles due to cyclic contact separation movement between the sensor and the human body by maintaining mechanical stability when it is utilized as a wearable device. The fabric sensor was subjected to tapping cycles up to 75000 times to determine its performance. No crack or deformation was visible over the fiber surface even after 75000 tapping cycle (Figure 2.20a).

Moreover, the V_{oc} of the fabric sensor was tested up to 75000 tapping cycles, demonstrating a relatively constant output voltage of 30 V (Figure 2.20b). PVDF is known for its superior physical and chemical durability as it shows excellent resistance to degradation to various chemical and environmental conditions[16]. Chemically, PVDF is resistance to oxidation and corrosion, including organic acids, salts, weak bases, and aliphatic, aromatic, and chlorinated solvents, proving its potential as an ideal material for wearable applications[16]. PVDF and GNP-PVDF nanocomposites are inherently hydrophobic materials that exibit low wetting ability[8, 151].

Another major requirement of a TENG fabric sensor is washability, including multiple washing cycles, being subjected to friction with constituent support yarn (cotton, polyester, wool, etc.). Moreover, the fabric sensor must be resistant to the mildly alkaline environment ($pH10$) created by a standart detergent solution, which constitutes anionic groups, long-chain hydrocarbons, and a single non-ionic group[152]. To exemplify its ability to withstand washing conditions, the PGr-5 fiber was first subjected to a soap solution test in an alkaline medium (Figure A.2).

A 12-cm-long TENG fiber was immersed in 0.5% detergent solution and stirred continuously at 60°C for 2 hr. The output voltage of the fiber was measured after each washing cycle which was repeated for 6 times. The washing cycle produced fairly constant output indicating the ability of PGr-5 fiber for stability in alkaline medium. Furthermore, during high-speed rotation inside a washing

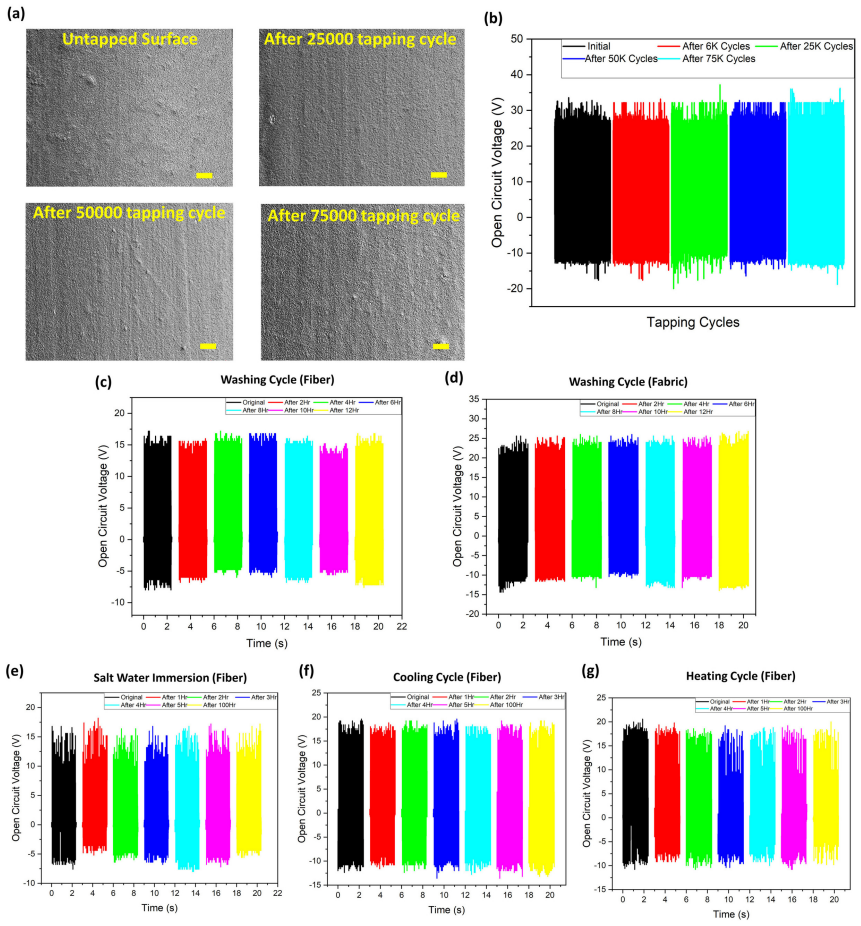

Figure 2.20: Durability test for PGr-5. (a) PGr-5 fiber's surface image at different stages of thousands of tapping cycles Scale bar: 10 μm. (b) Reliability of output voltage for thousands of tapping cycles. Washability test for (c) fiber and (d) fabric. Both fiber and fabric demonstrated stable output during multiple washing cycles. (e) Saltwater stability for PGr-5 fiber. Voltage output of the PGr-5 fiber during multiple (f) cooling and (g) heating cycles.

machine, fabric faces centrifugal force (pushes the fabric outwards against the walls of the drum during the spin cycle), friction force (opposes the motion of the fabric against the walls of the drum), G-force (due to spinning of the drum) and water pressure[153]. The fabric sensor's ability to withstand these forces to sustain constant output was manifested by subjecting it to high-speed rotation-induced stress inside a washing machine at 60°C with 1000 rpm for 2 hr and output voltage was measured. The cycle was continued for a total of 12 hr. In both cases (soap solution and washing machine test), the fiber and fabric sensor produced fairly constant output during multiple washing cycles (Figure 2.20c, 2.20d). In addition, during day-to-day usage, the fabric sensor has to get in contact with sweat. The long-term stability of the triboelectric output should not be degraded due to contact with sweat, which contains electrolytes like dissolved sodium and chloride secreted from sweat glands[154]. To determine its salt water stability, PGr-5 fiber was immersed in 4% salt water solution and after 100 hr of immersion, the output remained fairly constant (Figure 2.20e). Multiple cooling and heating cycles also produced sustained output (Figure 2.20f, 2.20g). This work proved the durability of wearable TENG in harsh weather conditions. Further details of the tests were provided in the experimental section. In addition, PGr-5 TENG fiber‘s superior flexibility made it compatible with basic textile processing, such as bending and knotting which are necessary requirements to weave or knit fabric structure. The fabric sensor preserved flexibility in the horizontal and vertical directions even after weaving (Figure 2.21).

2.7 Temperature Dependence of the Triboelectric Output

Wearable devices are frequently subjected to outdoor environments, often experiencing freezing cold or extreme heat. Temperature can fluctuate rapidly at different hours throughout the day. Moreover, the temperature inside a shoe can increase up to 8°C after 15-20 min of running[155]. Thus, standardizing TENG output at a wide temperature range is necessary before integrating it with

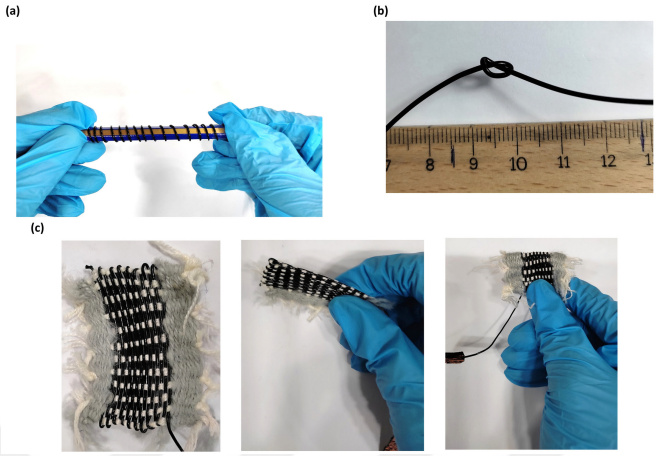

Figure 2.21: (a) TENG fiber wrapped around a pencil demonstrating its flexible property. (b) The knotting of TENG fiber demonstrates its applicability in textile processing. (c) Bending of TENG fabric in the horizontal and vertical direction.

wearable equipment. In PGr-5 TENG, charge transfer from PEI to GNP-PVDF composite film occurs due to triboelectrification. On the contrary, reverse charge transfer from PGr composite to PEI occurs due to thermal fluctuation[156]. Constant charge quantity in the triboelectric surface is achieved after a dynamic equilibrium is established due to electron' s forward and backward movement. At high temperatures, this backward movement tends to rise significantly, reducing the triboelectric surface's charge density and overall triboelectric output[157, 158]. For determining temperature dependence on the triboelectric output of PGr-5 fiber, a small custom motor-driven tapping device (2 cm $\times$ 1 cm contact area) was used inside a closed heated chamber (Figure A.3).

PGr-5 fiber showed high triboelectric output at room temperature due to the small extent of this thermal fluctuation. V_{oc} and I_{sc} output remained stable until 80°C, and further increase in the temperature caused lower outputs (Figure 2.22a, 2.22b). The power output at room temperature was significantly higher than at 100°C (Figure 2.22c, 2.22d). The peak power output at 100°C decreases by 46% (1.18 μW) compared to the room temperature peak power output of 2.2 μW (Figure 2.22e). This phenomenon occurred due to the greater extent of thermal fluctuation, which promoted the backward movement of energetic electrons to surpass barrier height[159]. At low temperatures, the electron cannot acquire

sufficient energy to surpass the barrier; thus, produced stable triboelectric output over a large temperature range for PGr-5 TENG.

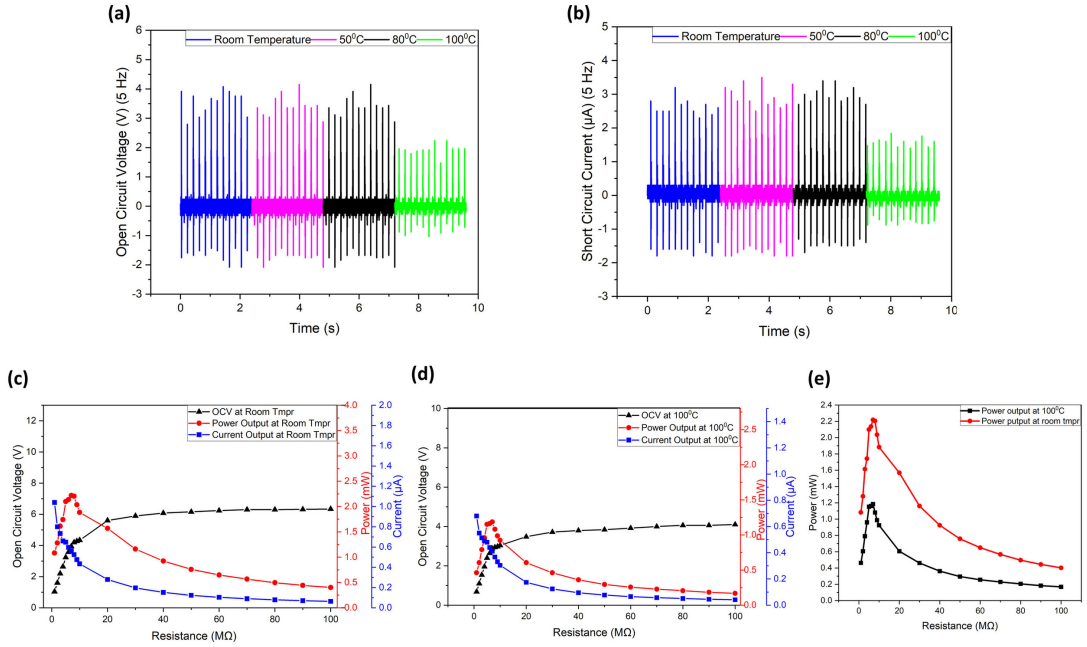

Figure 2.22: Temperature dependence of triboelectric output. (a) V_{oc} and (b) I_{sc} of the PGr-5 fiber at different temperatures. Power output for PGr-5 (c) at room temperature and (d) 100°C. (e) Peak power output for PGr-5 at room temperature and 100°C.

2.8 TENG Fabric for Self-Powered Sensing and Energy Harvesting

Evaluating the fabric TENG performance in the case of basic human motion like walking, hand movement, arm bending, and grasping is a way to estimate its applicability for real-world application. The ability of pattern detection is essential for any physical movement monitoring sensor as it helps to analyze and understand deviation from the desired motion of interest in case of an anomaly[160].

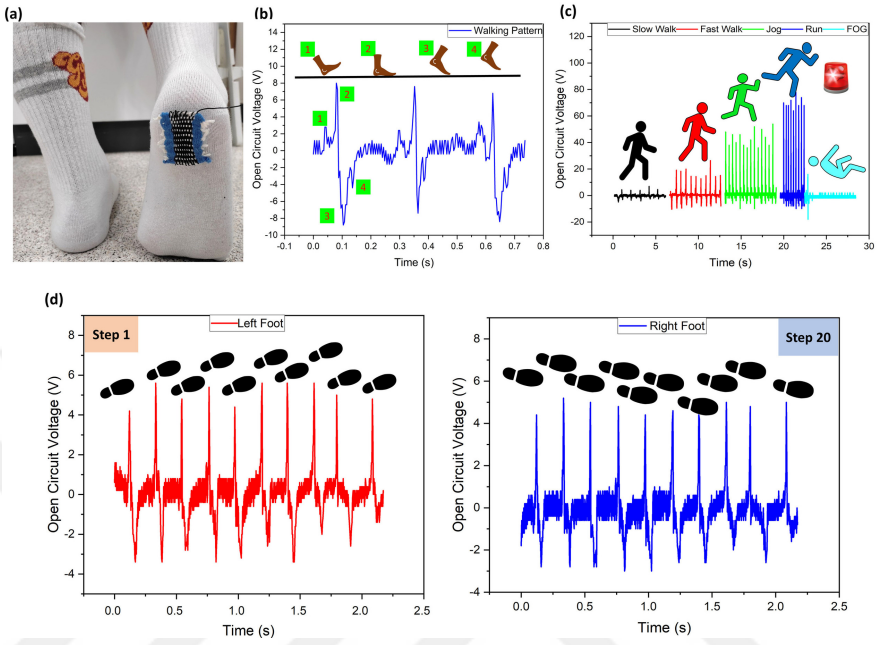

Figure 2.23: Demonstration of real-world applications with TENG sensor. (a) Smart TENG sock prepared by TENG fabric attachment at the heel region. (b) Detection of walking pattern using TENG output. (c) Variation of open circuit voltage at varied human movement speed (sensor was attached on right sock only). (d) Step count measurement (sensor was attached to both socks).

For real-world applications, first, the lower panel of heel portion of a sock was replaced with the flexible PGr-5 fabric sensor demonstrating its ability to integrate with textiles (Figure 2.23a). The devised smart sock was successfully employed for gait analysis for a regular gait cycle which include heel contact, toe contact, heel leave, and toe leave[161].

During a complete walking cycle, the first two peaks represent heel contact and toe contact causing successive positive peaks. The following two peaks represent heel separation and tow separation causing successive negative peaks. As depicted in Figure 2.23b, the smart sock detected all four movements during a walking cycle separately, demonstrating its superior sensitivity and selectivity. Thus, the sensor can be used to study abnormal movement patterns caused by a variety of neurologic or orthopedic such as Parkinson's[162], runners dystonia[163] and musculoskeletal abnormality, and it can be utilized for initial disease detection and

subsequent rehabilitation process. Furthermore, the smart sock detected movement at various speeds characterized by the variable output voltage. At walking speed, the force exerted over the sensor was much smaller. This corresponds to a lower contact area and lower voltage output[164]. However, in the case of jogging and running, the exerted force increased the overall output voltage (Figure 2.23c). Moreover, human footsteps can be counted by attaching the sensor on both socks, as each peak in the voltage output corresponds to a footstep during human motion (Figure 2.23d).

The sensor also detected the freezing of gait (FOG) characterized by a sharp bottom peak with high negative amplitude and successive irregular peaks without generating any high positive peak indicating that the feet are still off the ground (Figure 2.24). Other information related to walking movement, like cadence[165] (number of steps taken per minute, for slow walk $\sim$ 2, for fast walk $\sim$ 4), can be analyzed from the signal generated by the smart sock through the period of walking cycle (Figure 2.25).

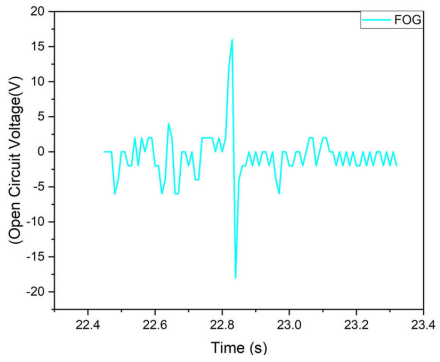

Figure 2.24: Characteristic output voltage for failing of gate (FOG).

After that, two fabric sensors were fitted between the forearm and upper arm region on both hand which demonstrated detection ability of arm movement separately (Figure 2.26).

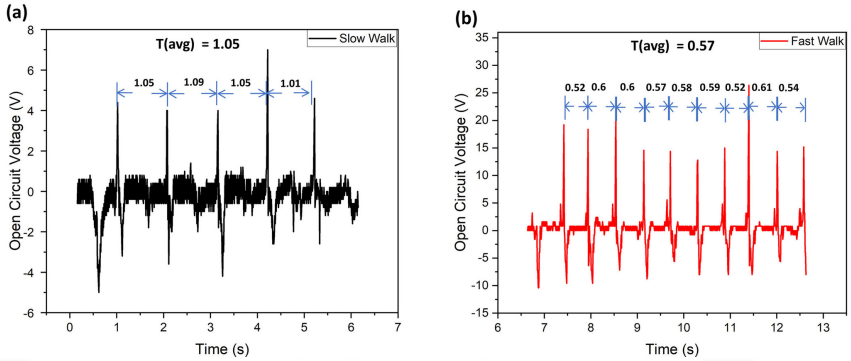

Figure 2.25: Output voltage for (a) slow walk, (b) fast walk with period T between each cycle (sensor was attached on right sock only).

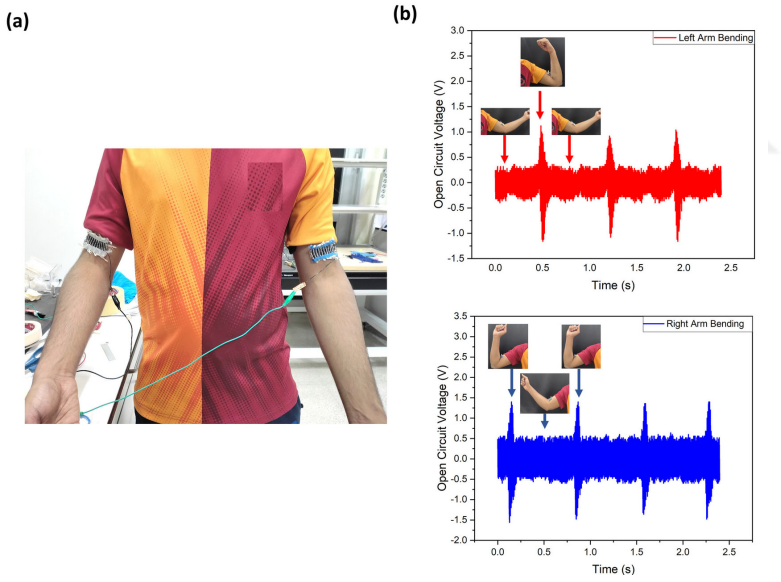

Figure 2.26: TENG sensor attached between the forearm and upper arm region for arm movement monitoring. (a) Sensor attachment. (b) Arm bending detected through monitoring of output.

Furthermore, the sensor was subjected to hang grasping by fitting the sensor in the palm of two hands and a higher grasping force was applied for right-hand grasping. The sensor could detect the difference of applied pressure by larger voltage output, as evidenced by Figure 2.27.

This demonstration proves the fabric TENG's potential of direct integration with human clothing in the form of socks, gloves, knee sleeves, elbow sleeves, and so on for physiological monitoring. However, due to non-intimate irregular contact of the fabric sensor with the body, the voltage output presents a high amount of noise.

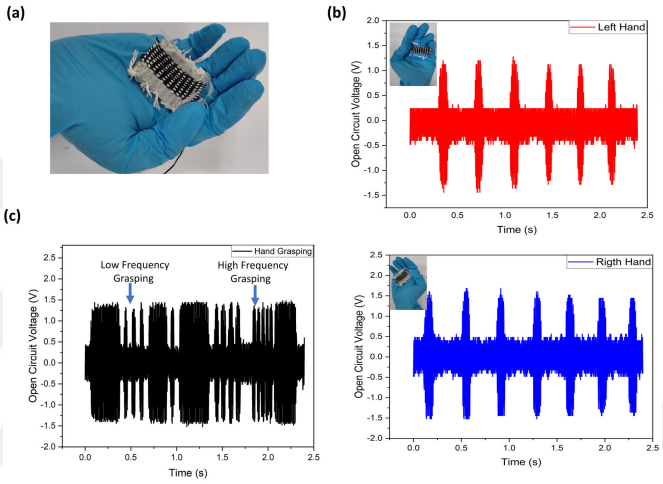

Figure 2.27: Hand grasping test for PGr-5 TENG. (a) Sensor placement on palm. (b) Detection of hand grasping by the Fabric TENG. (c) Detection of high and slow-frequency grasping.

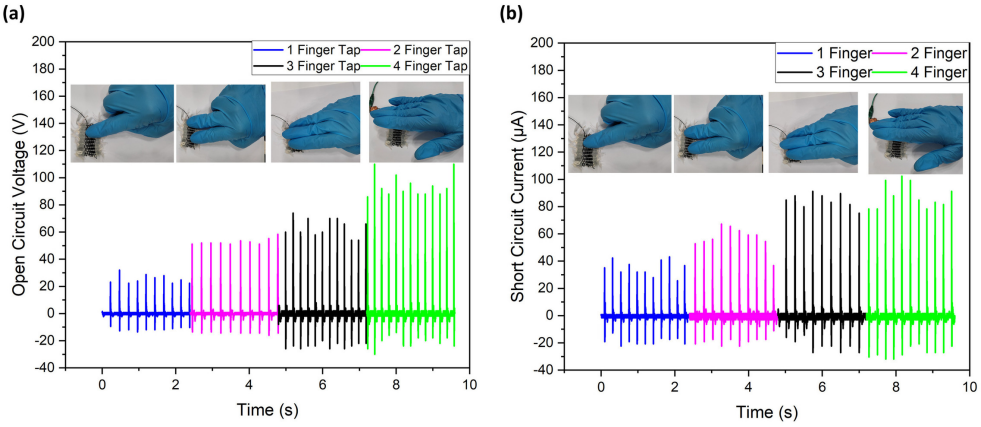

Figure 2.28: (a) V_{oc} and (b) I_{sc} for hand tapping with one to four fingers.

TENG sensors integrated with clothing provide an excellent opportunity to

scavenge mechanical energy from human motion and convert it to electrical energy. Figure 2.28, shows that full hand tapping on the fabric sensor can lead to an V_{oc} of 110 V and a I_{sc} of 100 μA. However, TENG produces alternating current and a rectifier circuit is essential for AC to DC conversion as AC output is unsuitable for many electronic devices[166]. For this reason, a bridge rectifier was connected to the fabric sensor for AC to DC modulation.

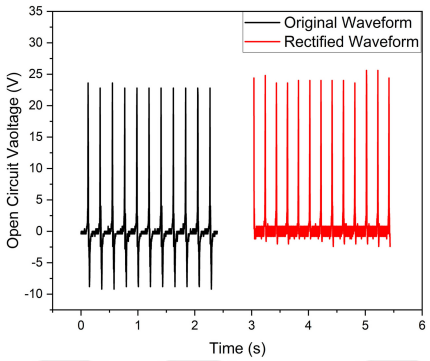

Figure 2.29: Rectified output voltage using a bridge rectifier.

Figure 2.29. shows the conversation of the AC signal generated from the sensor to the DC signal as desired which can be utilized to charge commercial capacitors. The fabric sensor was connected to a 10 μF capacitor through a bridge rectifier to confirm its ability to charge energy storage devices. The fabric sensor demonstrated sufficient energy generation due to human motion to run a portable electronic device (table clock). Hand tapping of the sensor for 1 min stored enough charge in the capacitor (10 μF) to run the clock for 7 sec (Figure 2.30).

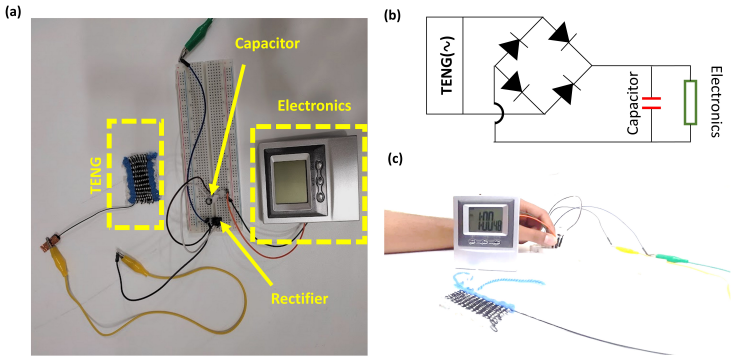

Figure 2.30: (a) Setup for powering up simple electronic instrument. (b) Equivalent circuit. (c) Hand tapping to power up a table clock.

2.9 Summary

In this study, successful fabrication of GNP integrated PVDF triboelectric fiber through thermal drawing was presented. In this process, we can fabricate potentially kilometer-long fiber that proves its applicability in industrial-scale production. Moreover, the fiber output increases with increased GNP content as 2D materials enhance PVDF's β phase and surface roughness. The peak power output of the PGr-5 increased by 208% compared to pure PVDF fiber. The fabricated sensor can generate a power density of 53.57 $\mu W m^{-2}$, enough to power up electronic devices like table clocks. The power density was higher compared to recently devised textile based TENGs in SE mode (Table 1). Additionally, the fiber is durable enough to endure textile processing and rough weather conditions, maintaining relatively constant output. The fiber demonstrated long-term stability in various harsh weather conditions. We have shown that the thermally drawn GNP-integrated PVDF TENG fiber has the potential to be directedly integrated with textiles for psychological monitoring and energy harvesting. We envision that this work will contribute to functional fiber processing, energy harvesting, sensing and pave the way for advancing low-dimensional material-integrated triboelectric fiber and textile-based electronics.

Chapter 3

Thermal drawing of MoS_2 integrated PVDF triboelectric fibers for continuous respiration monitoring

[1] Triboelectric nanogenerators (TENGs) are environmentally sustainable energy harvesting devices that can convert mechanical and biomechanical energy into electrical output through the synergistic process of triboelectrification and electrostatic induction. Incorporating polyvinylidene fluoride (PVDF) and its copolymers into flexible TENG is particularly advantageous because of the abundance of highly electronegative fluorine ions and high dielectric constant. MoS_2 can interact with PVDF dipoles to improve PVDF's β phase content, thereby improving the triboelectric property of the polymer nanocomposite fibers. In this study, thermally drawn PVDF TENG fibers are fabricated, incorporating various concentrations of MoS_2 for the first time. The enhanced β phase property in the nanocomposite fiber improves the triboelectric output where 3 wt.% MoS_2 -

[1] At the time of submission of the thesis, the content of this chapter is under review in Advanced Sensor Research for publication. The authors are Md Sazid Bin Sadeque, Mahmudur Rahman, Md Mehdi Hasan, and Mustafa Ordu. The work is equally contributed between 1st and 2nd authors.

PVDF fiber demonstrates a maximum peak power output of 17.64 μW, exhibiting a 3-fold increment compared to 0 wt.% MoS_2 - PVDF fiber. Simultaneous integration of multiple nanomaterials (MoS_2 and graphene nanoplatelet) is also investigated to analyze the triboelectric fiber's β phase formation and electrical performance. Harnessing the superior sensitivity of the MoS_2 integrated triboelectric fiber, a self-powered wearable mask is designed for continuous human respiration monitoring.

3.1 Introduction

Flexible electronic fibers and functional textiles capable of capturing physiological data have become a promising platform for diverse applications encompassing human motion tracking,[69, 70, 167, 168, 9, 169] human-machine interface[170], artificial intelligence[171, 172], implants and prostheses, and body-adaptive healthcare monitoring[173, 174, 175, 176]. A key challenge for the sustainable application of functional fibers in wearable applications is the requirement for a battery-free, flexible power system. The utilization of energy-harvesting triboelectric nanogenerator devices (TENGs) has recently attracted significant interest due to their promising electrical power output and a wide range of lightweight material choices that provide clean energy for wearable devices[127, 169, 177, 178, 179, 180]. TENG devices combine contact-electrification and electrostatic induction effects to generate triboelectric output from mechanical and biomechanical motions, such as vibration, rotation, friction, expanding/contracting motions, and human movements[181, 182, 183, 184, 185].

Significant development has been made in the planar TENG devices, integrating low-dimensional materials, chemical functionalization, and microstructure for improved performance in energy harvesting and sensing applications[186]. However, the main drawback of planar TENG devices is the lack of scalability and breathability, hindering widespread TENG integration into wearable devices[187]. Fiber-based flexible TENGs are convenient in wearable applications due to their ability to be directly integrated into clothing as a self-energy generating and

sensing device during human motion[188, 189, 190]. To date, twisted[191], coaxial[192, 193, 194], and interlaced[195] fiber TENG configurations have been proposed, but the performance and applications remain limited in critical physiological vitals monitoring due to poor electrical performance of the device sensors. Liquid metal core has recently been demonstrated to improve electrical output and flexibility[55, 196]; however, maintaining liquid metal in the fluidic state over the entire service temperature range may require supercooling[141]. Thus, overcoming limitations of materials, designs, and manufacturing technologies to fabricate industrially relevant all-polymer flexible high-performance triboelectric fibers in single-step manufacturing is essential for widespread applications of triboelectric fibers in wearable applications. With its scalable production capability, thermal fiber drawing process has become a suitable alternative in this respect.

A wide range of polymeric materials has recently been investigated as friction layers in triboelectric nanogenerators[28]. Ferroelectric fluoropolymers like polyvinylidene fluoride (PVDF) have garnered significant interest due to their high electronegativity, flexibility, and tunable polarizability[29, 30]. Different strategies, including ion injection[31], increment of dielectric constant[32], spontaneous polarization[33], surface functionalization[34], and inclusion of charge trapping interlayer[35]] have been reported to increase triboelectric output. Integration of low dimensional material has been widely utilized as an effective strategy to tune the dielectric property of a polymer nanocomposite to improve the charge density of the friction layer[36]. Various low dimensional nanomaterials have been reported with TENGs, for example, graphene, graphene oxide, MXenes, transition metal dichalcogenides (TMDs), black phosphorus (BP), layered metal-organic frameworks (MOFs), hexagonal boron nitride (h-BN), layered covalent-organic frameworks (COFs), and layered metals[39, 40, 41, 42, 43, 44, 45]. Among TMDs, MoS_2 is reported to demonstrate the highest triboelectric output due to its superior electronegativity[37]. Moreover, the presence of surface termination groups in MoS_2 assists in attracting and trapping free electrons to improve the overall charge density of the nanocomposite[197].

In this study, we present the scalable fabrication of MoS_2 integrated thermally

drawn PVDF triboelectric fibers for the first time, which shows improved performance in sensing applications due to its superior triboelectric property compared to previously reported thermally drawn PVDF nanocomposite fibers. The β phase of 3 wt.% MoS_2 integrated PVDF fiber increased to 47.5%, the highest reported for thermally drawn PVDF nanocomposite fiber to date. Moreover, dual nanocomposite fiber was also studied by combining MoS_2 with graphene nanoplatelet (GNP) to investigate the β phase property. Harnessing the improved sensitivity of the fabricated TENG fibers, a wearable face mask was developed by integrating the TENG fiber to monitor real-time respiration parameters. A single fiber TENG sensor was also interfaced with the eyelid and index finger to demonstrate its ability to detect and analyze biomotion.

3.2 Experimental Section

3.2.1 Chemicals and films

Polycarbonate (PC) and Polyvinylidene difluoride (PVDF) were sourced from Ajedium Films. Conductive polyethylene (CPE) was purchased from Goodfellow. Bulk Molybdenum disulfide nanopowder (MoS_2) (purity: 99.95%, size: 100 nm) and graphene nanoplatelet (GNP) (purity: 99.9%, size: 3 nm, S.A: 800 $m^2\ g^{-1}$, dia: 1.5 μm) were acquired from Nanografi, Turkiye. Dimethylformamide (DMF) was purchased from Carlo Erba Reagents S.A.S. and dichloromethane (DCM) from Merck KGaA.

3.2.2 Preparation of triboelectric nanocomposite film

First, the commercially sourced PVDF was dissolved in DMF at 25 wt.% by constant magnetic stirring at 60 °C for 1 hour. Simultaneously, MoS_2/ MoS_2-GNP nanoparticles are ultrasonicated for 1 hour. Then, two solutions were mixed

and subjected to magnetic stirring for 3 hours. After that, the uniform polymer nanocomposite solution was poured onto a glass plate, and the solvent was evaporated by storing the glass plate inside the heated chamber at 80 °C for 8 hours. Finally, the extracted nanocomposite film was put into a vacuum chamber at 90°C for 1 day to remove any residual DMF and moisture.

3.2.3 Preparation of triboelectric fiber

The preform was prepared using a thermal consolidation process. In this process, multiple layers of PVDF nanocomposite were wrapped over a CPE rod prepared by a hot press molding process. An additional sacrificial layer was rolled over the nanocomposite layer to ensure a stable thermal draw. The rolled preform was then annealed in a furnace at 150°C for 2 hours, followed by consolidation at 190°C for 45 minutes inside the furnace. Finally, the preform was cooled and prepared for thermal draw.

The thermal drawing was conducted in a custom-built draw tower with a furnace of two heating zones. The stable drawing was obtained at 240°C temperature. The diameter of the fiber was controlled by varying the feed and capstan speed. The drawn fiber was finally collected on a spool. Later, the outer PC layer was removed by dissolving it in a DCM solution to get an exposed triboelectric layer.

3.2.4 Materials characterization

For β phase analysis of the triboelectric fibers, Fourier Transform Infrared Spectroscopy (FTIR) was performed in Bruker ALPHA Platinum-ATR FTIR with 128 scan steps and 4 cm^{-1} resolution. Fiber's morphological structure and EDS spectra were analyzed by FEI QUANTA 200F field emission SEM. Pananalytical X'pert Pro XRD using Cu $K\alpha$ radiation was used for X-ray diffraction spectroscopy (XRD) analysis. X-ray photoelectron spectroscopy (XPS) analysis was

performed with Thermo Fisher Scientific $K\alpha$. Keyence VK-X100 3D Laser Scanning Confocal Microscope was used to acquire the Laser DIC images.

3.2.5 Electrical characterization

For the electrical characterization of the triboelectric nanocomposite fiber, 12 cm was cut from a continuous fiber. Later, a 20 mm CPE electrode portion was exposed to attach the electrical wire with measuring instruments. Open circuit voltage measurement was conducted using an oscilloscope (Agilent Technologies DSO1014A), and short circuit current was measured using a low noise current preamplifier (Stanford Research Systems SR570). Cyclic tapping was delivered over the fiber using a custom-made tapping device.

3.3 Fabrication of Triboelectric Fibers

As demonstrated in Figure 3.1, the thermal drawing process (TDP)[68]] was utilized to fabricate triboelectric nanocomposite fibers. The fabrication involved three steps: solution processing, preform preparation, and thermal drawing. The PVDF films were dissolved in Dimethylformamide (DMF) in the first step. At the same time, MoS_2 nanoparticles were ultrasonicated in DMF at different concentrations. This process facilitated the breaking of weak van der Waals force between nanoparticle interlayers to form uniform nanoparticle dispersion[198]. Later, the two solutions were mixed and subjected to continuous magnetic stirring to prepare a uniform nanocomposite solution (Figure 3.1a). Then, the solution was poured into a glass plate and placed inside a heated chamber for solvent evaporation to obtain nanocomposite film. The film was later peeled off from the glass plate and annealed in a vacuum oven to remove the residual DMF within the film. A conductive polyethylene (CPE) rod was prepared separately as the electrode part of the fiber through hot pressing inside a Teflon mold. The nanocomposite film was tightly wrapped around the CPE rod with an outer sacrificial polycarbonate (PC) layer to assist the fiber drawing (Figure

3.1b). PVDF has a glass transition (T_g) and melting temperature (T_m) of -40°C and 171–180°C respectively, while T_g and T_m of polyethylene are -100°C and 120-140°C[79, 199, 200]. Given the large mismatch of thermal properties of the PVDF and CPE, the sacrificial PC layer ensured uniform thermal drawing of the multi-material nanocomposite fiber. The initial preforms underwent a thermal consolidation process to ensure the solidification of PVDF and PC layers before the drawing. The elevated temperature with controlled feed rate (V_{feed}) and drawing speed (V_{draw}) using a capstan motor ensured uniform fiber diameter by controlling the draw-down ratio (DDR) in a fiber draw tower (Figure 3.1c). DDR is expressed as,

$$DDR = \sqrt{\frac{V_{\text{feed}}}{V_{\text{draw}}}} \tag{3.1}$$

For polymers to be co-drawn, they need to have similar T_g and complex shear viscosity (η^*), while loss modulus (G") should dominate storage modulus (G') at drawing temperature. The ideal drawing parameters vary from polymer to polymer depending on the viscous behavior of the polymers, making multi-material thermal drawing challenging. Moreover, excessive filler content in nanocomposites also contributes further to the complexity of the thermal drawing process due to the alteration of flow viscosity at elevated temperatures[201]. Applying elevated temperature above T_g with drawing tension allowed the preform to deform into a thinner diameter. The experimental procedure led to uniform continuous nanocomposite fibers (PVDF - MoS_2, PMx; where x=0-5 wt.%) via TDP at 240°C (Figure 3.1d). The polymer structure was intact in the fiber's cross-section, proving the uniformity of the thermal drawing process (Figure 3.1e). The detailed fabrication protocol is described in the experimental section.

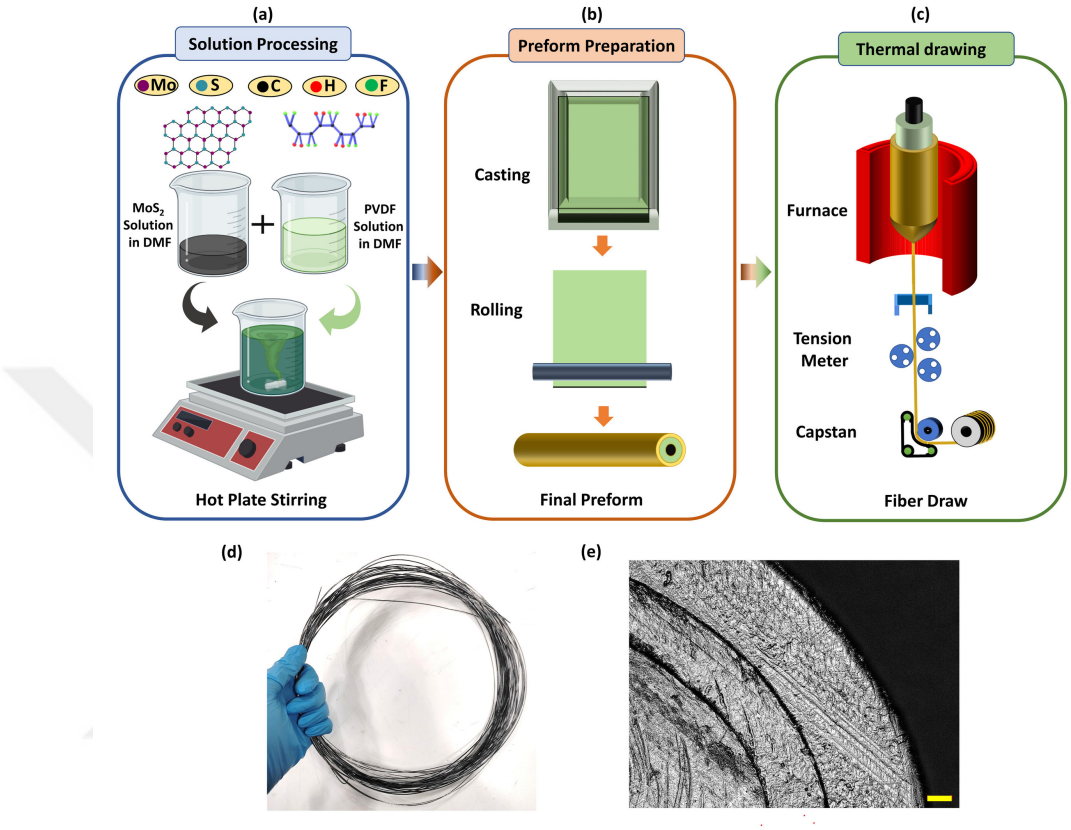

Figure 3.1: Fabrication procedure for MoS_2 - PVDF nanocomposite fibers. (a) Solution processing of MoS_2 and PVDF to produce uniform nanocomposite solution. (b) Preparation of final preform by casting and rolling. (c) Schematic of the thermal drawing process for continuous TENG fiber. (d) Continuous TENG fiber acquired from the thermal drawing process. (e) LSCM image of the drawn fiber's cross-section (Scale bar: 50 μm).

3.4 Materials Characterization

The incorporation of MoS_2 in PVDF improves the triboelectric property of the polymer nanocomposite. MoS_2 can act as a charge-trapping site at the interface of other materials, significantly impacting its electrical properties[202, 203], As received, bulk MoS_2 was used to prepare nanocomposite triboelectric fibers of different concentrations.

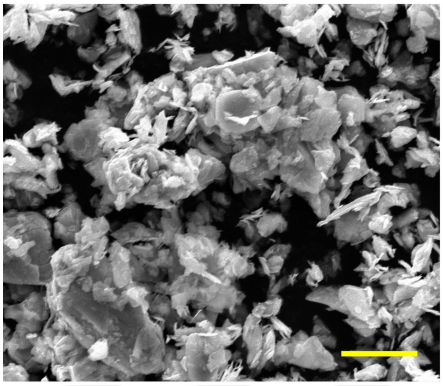

Figure 3.2: SEM image of the as-received bulk MoS_2 (Scale bar: 50 μm).

Figure 3.2 represents the scanning electron microscopy (SEM) of the as-received bulk MoS_2, showing the presence of MoS_2 nanoflakes.

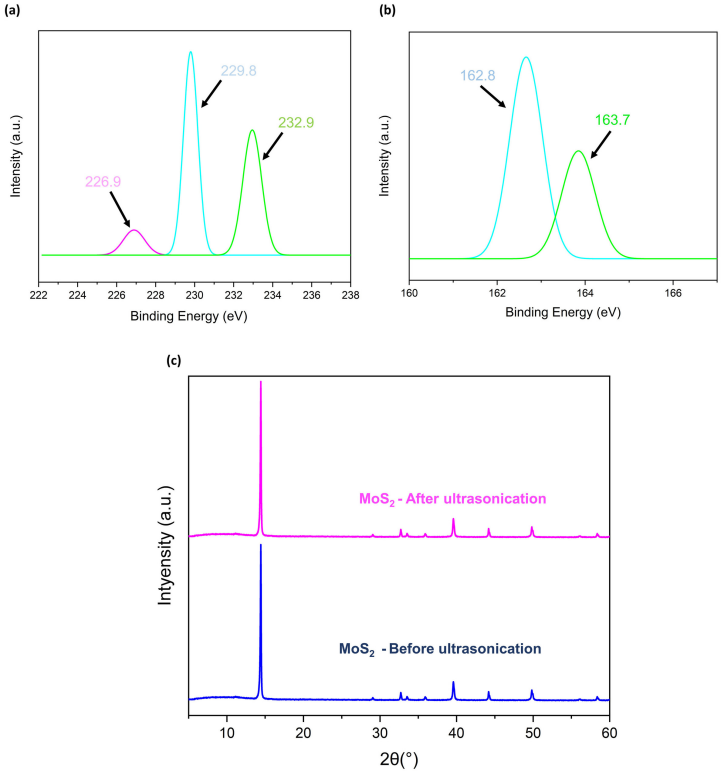

Figure 3.3: (a) and (b) XPS analysis of the as-received bulk MoS_2. (c) XRD spectra of bulk MoS_2 before and after ultrasonication.

S2s and Mo3d high-resolution spectra of X-ray photoelectron spectroscopy (XPS) were demonstrated in Figure 3.3a,b, where peaks at 226.9 eV, 229.8 eV, and 232.9 eV represent S2s, Mo3d5/2, and Mo3d3/2 orbitals, respectively[204], while, the binding energies of 162.8 eV and 163.7 eV in the S2p region correspond to S2p3/2 and S2p1/2[205].

The X-ray diffraction analysis (XRD) of the as-received bulk MoS_2 and ultrasonicated MoS_2 nanoparticles demonstrated similar spectra, presenting an unchanged crystalline structure and lattice parameters of MoS_2 before and after the ultrasonication process (Figure 3.3c).

PVDF demonstrates five different polymorphs - (α, β, γ, δ, ϵ), among them, (β, γ, δ) demonstrate electroactive properties (Figure 3.4)[93, 206]. The triboelectric output of PVDF is strongly affected by its electroactive phase content, and a higher β phase percentage facilitates increased triboelectric output[29, 207, 208]. In nonpolar α (TGTG') configuration, the polar dipole groups align in opposite directions, achieving a net zero dipole moment. However, for β (TTTT) phase configuration, all the dipoles align in the same direction, facilitating a net non-zero dipole moment, improving the dielectric property of the polymer nanocomposite[209].

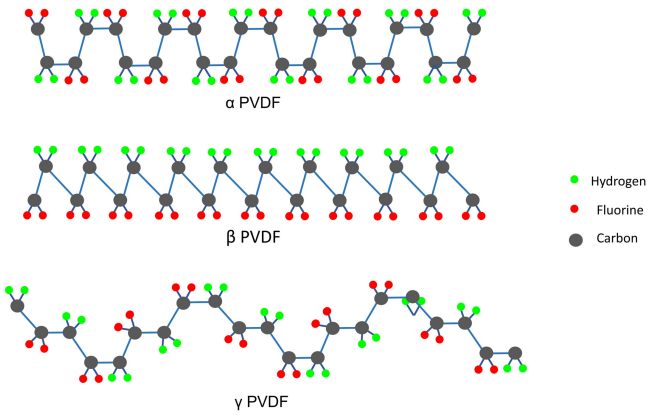

Figure 3.4: α, β and γ configurations of PVDF.

XRD and Fourier transform infrared spectroscopy (FTIR) analysis revealed

the electroactive phase transition due to the addition of nanomaterials and subsequent thermal drawing. Figure 3.5a shows the XRD spectra of 0 wt.% MoS_2 - PVDF (PM0) and MoS_2-PVDF nanocomposite fibers (PM1, PM2, PM3, PM4 and PM5). The crystalline α-phase of the PVDF polymer was represented by the diffraction peaks at 18.6° and 26.5° corresponding to (020) and (110) planes, respectively. The peak at 20.2° corresponds to the β phase at the (110)/(200) plane[210]. With the addition of nanomaterials, the α-phase of PVDF started to diminish, indicating the suppression of the α-phase with increasing filler content. In addition, a sharp peak at 20.2° confirmed the increment of the β phase due to the addition of MoS_2. The β phase enhancement can be attributed to nanofillers causing interfacial interaction through the surface charge of MoS_2 sheets and the positive CH_2 group of PVDF[211, 212].

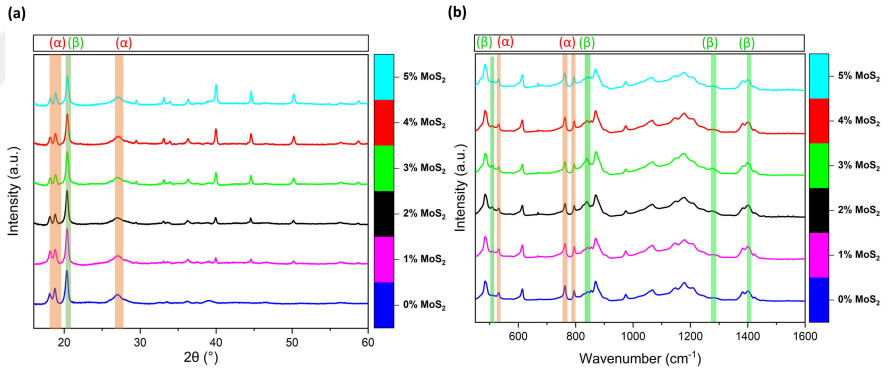

Figure 3.5: Material characterization of thermally drawn MoS_2-PVDF nanocomposite fibers. (a) XRD and (b) FTIR spectra of the 0 wt% MoS_2 - PVDF fiber and MoS_2-PVDF nanocomposite fibers with various wt%.

Figure 3.5b shows the FTIR spectra of the PM0-5 nanocomposite fibers. Different absorption bands in the FTIR spectra signify PVDF's nonpolar α, polar β, and γ phases. The vibrational bands observed at 532, 614, 763, and 795 cm^{-1} are attributed to the formation of α phase, whereas peaks at 510, 840, 1279, and 1401 cm^{-1} demonstrated the presence of β phase. In addition, γ phase peaks were observed at 833 and 1279 cm^{-1}[198]. The following equation calculates the relative proportion of β phase in PVDF:

$$F(\beta) = \frac{A_\beta}{\left(\frac{K_\beta}{K_\alpha}A_\alpha + A_\beta\right)} \times 100\% \tag{3.2}$$

where A_α and A_β represent the absorbance values at 763 cm^{-1} and 840 cm^{-1}, k_α andk_β represent the coefficient values of 6.1×10^4 and 7.7×10^4 cm^2 mol^{-1} at the wavenumber related to respective peaks.

The nonpolar α phase is the most dominant in commercially sourced untreated PVDF polymer film, with β phase content of only 30% (Figure 3.6).

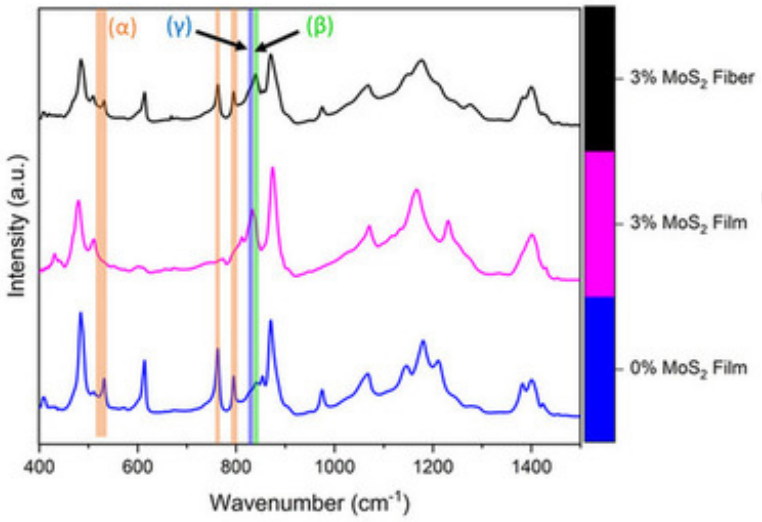

Figure 3.6: FTIR spectra of 0% MoS_2 film, 3% MoS_2 film and 3% MoS_2 fiber.

The α configuration in PVDF is the lowest energy conformer and, thus, the most stable, facilitating longer chain growth in pristine PVDF films. Ultrasonication and magnetic stirring promote static charge generation on the nanoparticle, which reorients the configuration of PVDF through a weak electrostatic interaction, contributing to the formation of the electroactive phases[112]. However, preparing nanocomposite films through solution processing facilitated the formation of slightly lesser electroactive γ phases (than the β phase) into nanocomposite, signified by a sharp γ phase peak at 833 cm^{-1} (Figure 3.6). The subsequent

thermal drawing process with axial stretching aligned the polymer chain, improving the crystalline property and assisting in β phase formation, suppressing the γ phase simultaneously (Figure 3.6). Moreover, the filler concentration also affected the formation of the β phase in thermally drawn fibers. As presented in Figure 5b, the intensity of the absorbance peak at 840 cm^{-1} (TTTT configuration) continued to increase with increasing filler content. In contrast, the absorption peak of the nonpolar α phase gradually decreased at 763 cm^{-1} with the addition of MoS_2. β phase content is calculated as 37.6% for 1 wt% MoS_2 addition and 47.5% for 3 wt% MoS_2 addition. However, contrary to previously reported thermally drawn PVDF fibers, it started to decrease with the further increment of MoS_2 and decreased to 36.4% for 5 wt% MoS_2 (Figure 3.7)[8, 9].

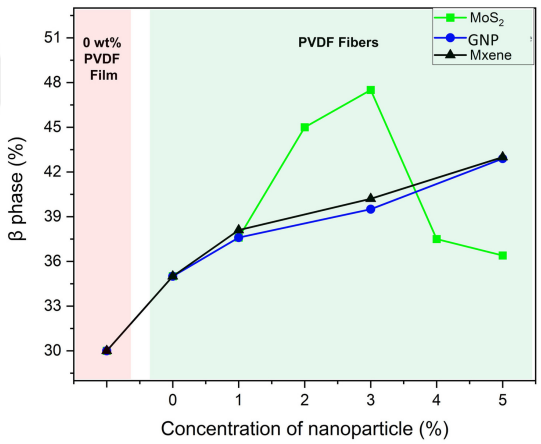

Figure 3.7: Comparative analysis of the β-phase formation between MoS_2, GNP and MXene ($Ti_3C_2T_x$) integrated nanocomposite TENG fibers[8, 9].

Elemental mapping analysis by energy-dispersive spectrometry (EDS) was conducted on the surface of the PM3 fiber to analyze the elemental composition of the sample (Figure 3.8a). EDS mapping of the PM3 fiber proved the uniform distribution of MoS_2 and the presence of Mo, S, and F groups in the PVDF matrix (Figure 3.8b). Energy signals from carbon and fluorine were obtained at 0.24 and 0.5 KeV, proving the presence of PVDF in the nanocomposite, while the energy signal of Mo and S was obtained at 2.5 KeV (Figure 3.8c).

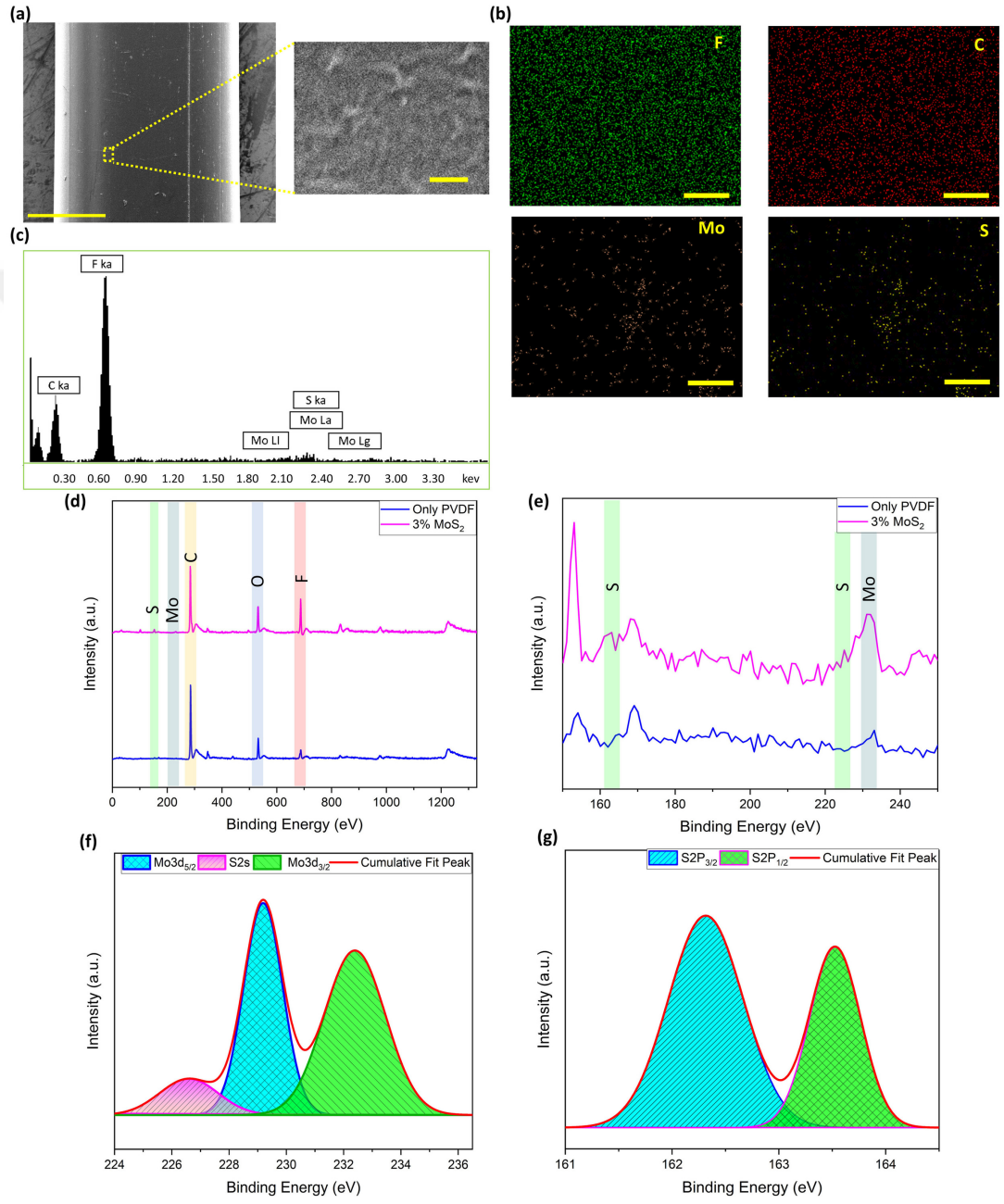

Figure 3.8: SEM and XPS analysis of PM3 nanocomposite fiber. (a) SEM image (Scale bar: 500 μm) and zoomed-in view of the mapping point (Scale bar: 2 μm). (b) EDS element maps of F, C, Mo and S. (c) EDX spectra of PM3 fiber. (d) XPS survey of PM0 and PM3 fibers. (e) Zoom-in view of the XPS survey from 150 to 250 eV. High-resolution XPS spectra of (f) Mo3d and (g) S2p.

An XPS survey was performed on the PM0 and PM3 fibers to understand the nanocomposite fibers' bonding characteristics and surface compositional elements, as shown in Figures 3.8d, 3.8e (zoomed-in view). The presence of C, F, Mo, and S was detected in the PM3 fiber. In the deconvoluted peak of Mo high-resolution spectra, Mo^{4+} 3d5/2 and Mo^{4+} 3d3/2 were detected at 229.3 eV and 232.5 eV, respectively, while the S2s peak was observed at 226.6 eV (Figure 3.8f). Moreover, a high-resolution scan of the S2p region detected the presence of S^{2-} 2p3/2 and S^{2-} 2p1/2 bonds represented by the deconvoluted peaks at 162.3 and 163.5 eV, respectively (Figure 3.8g). Furthermore, the high-resolution survey of C1s and F1s proved the conservation of the original chemical composition of PVDF in the nanocomposite fiber (Figure 3.9). 284.6, 285.6, 287.7 and 290.5 eV peaks of deconvoluted C1s scan represent -C, C=C, C-F, -CH2-CH2-, and -CF3- bonds, respectively (Figure 3.9a), while peak at 687.3 eV corresponds to C-F bonds for F1s (Figure 3.9b)[213].

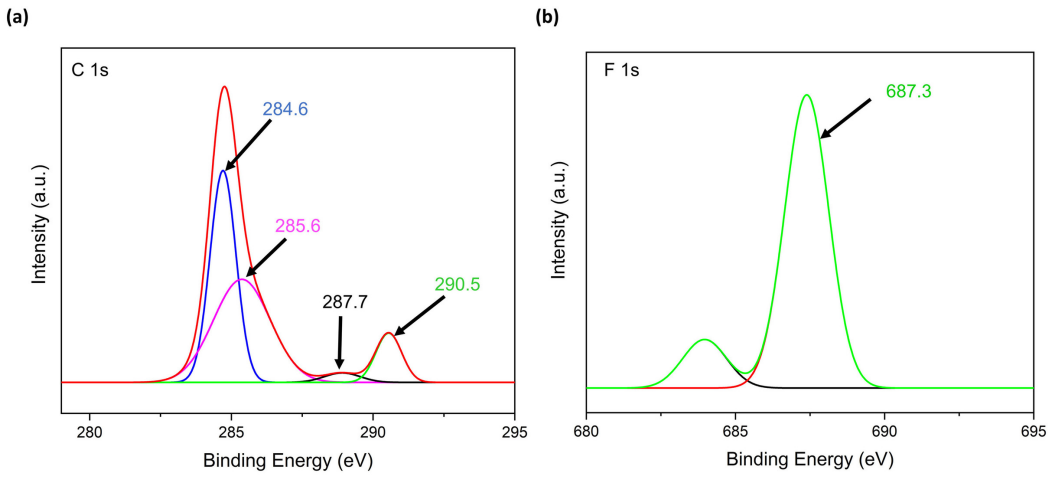

Figure 3.9: High-resolution XPS spectra of PM3 fiber for (a) C1s and (b) F1s.

To better understand the reason for the aggravating β phase content at higher concentrations of MoS_2, EDS analysis was conducted on the surface of the PM1-5 fibers. As demonstrated in Figure 3.10a-c, MoS_2 distribution remained relatively uniform until 3 wt.% concentration and agglomerated beyond 3 wt.% concentration (Figure 3.10d-e).

SEM imaging of the TENG (PM0-5) fiber's surface also confirmed the agglomeration states at higher MoS_2 concentrations (Figure 3.11a-f). Due to this agglomeration, MoS_2 fails to uniformly interact with PVDF to change the polar orientation from α-phase to β phase[214].

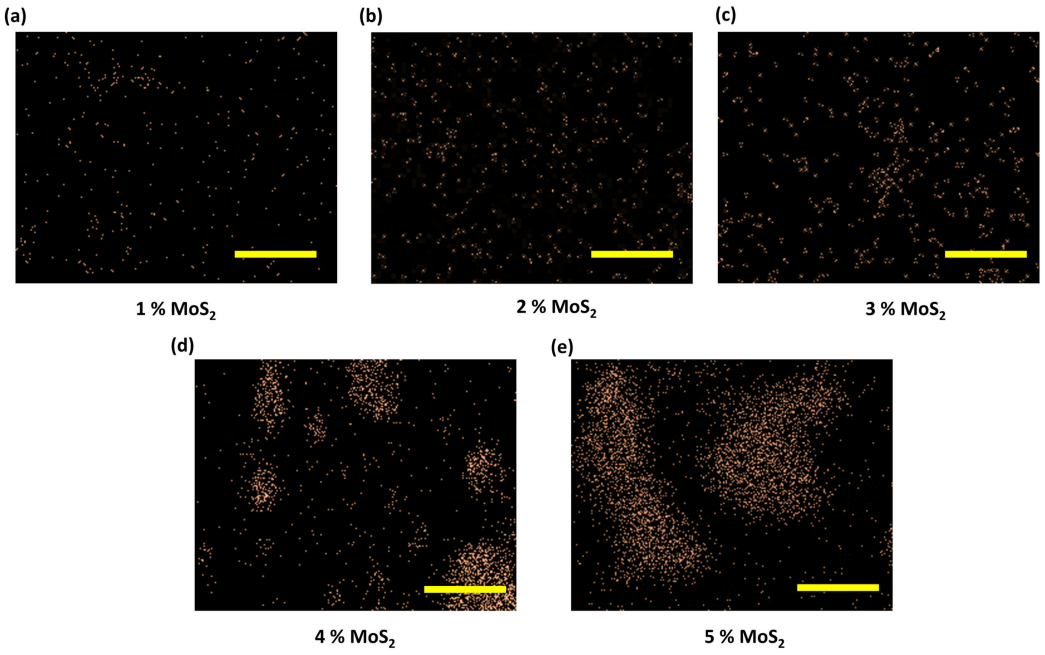

Figure 3.10: EDS elemental mappings for the surface agglomeration of MoS_2 in PVDF fibers at different nanoparticle concentrations: (a) 1 wt% MoS_2, (b) 2 wt% MoS_2, (c) 3 wt% MoS_2, (d) 4 wt% MoS_2 and (e) 5 wt% MoS_2 (Scale bar: 2 μm).

To improve β phase content beyond 47.5% and, at the same time, inhibit the agglomeration, a 2D material, GNP, was added in different concentrations (1-2 wt.%) with PVDF nanocomposite while MoS_2 concentration was kept lower or equal to 3 wt.%. However, adding multiple nanomaterials (MoS_2 and GNP) into PVDF triboelectric fiber was detrimental to β phase formation (Figure 3.12a, 3.12b and 3.12c).

The cross-sectional area of PVDF fiber with different dual nanoparticle concentrations was examined to understand the reason for this reduction. The addition

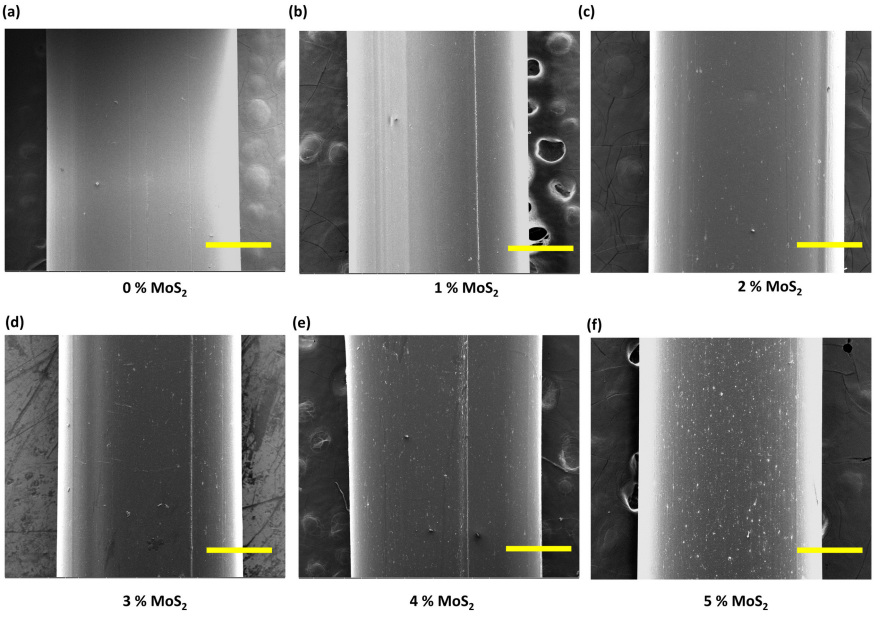

Figure 3.11: Surface morphologies of (a) PM0, (b) PM1, (c) PM2, (d) PM3, (e) PM4 and (f) PM5 fibers (Scale bar: 500 μm).

of GNP, even at lower concentrations with MoS_2, exhibited a clear tendency towards agglomeration. Figure 3.13a demonstrates that the PM0 fiber showed no nanoparticle at the fiber's cross-section. For PM3 fiber, the reasonably uniform distribution of MoS_2 is also visible as white spots, further indicating the reason for its improved triboelectric property (Figure 3.13b). However, when the GNP was added to the PVDF matrix, a large portion of dark spots appeared on the fiber cross-section (Figure 3.13c-f). This could be due to the mismatch of particle size between the utilized MoS_2 (size 100 nm) and GNP (Size: 3 nm) that are the available materials at the time of the work. Smaller nanoparticles tend to present increased surface area and stronger interaction potential, forming weak van der Waals forces with other nanoparticles[215, 216]. Thus, the GNP used in this experiment, having a much lower particle size, is prone to agglomeration compared to MoS_2. The addition of secondary nanoparticles with larger sizes may alter the properties positively.

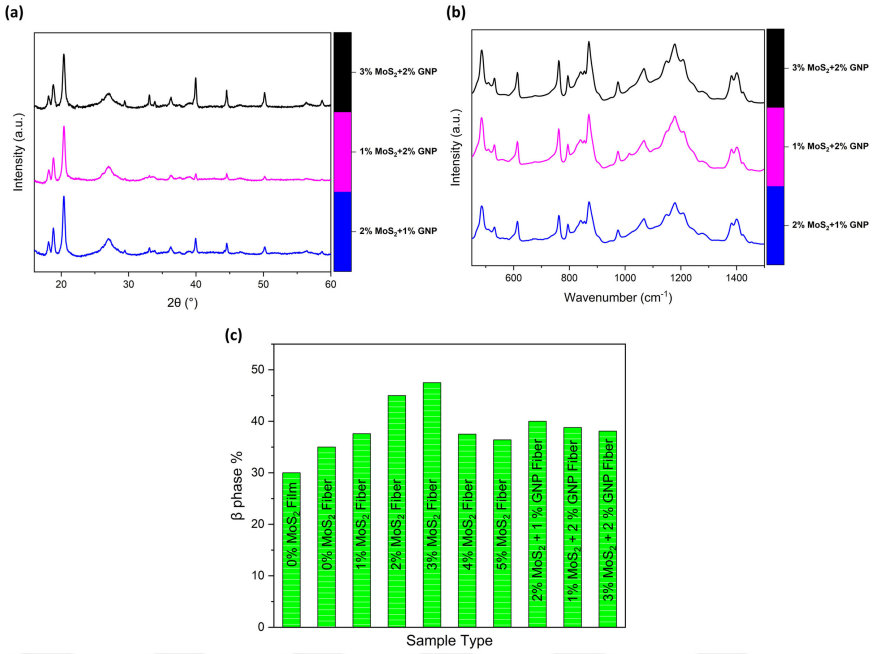

Figure 3.12: (a) XRD and (b) FTIR spectra of MoS_2 and GNP integrated PVDF TENG fibers and (c) their corresponding β-phase formations.

3.5 Electrical Characterization

The triboelectrification process operates on the fundamental principle of contact electrification and electrostatic induction[121]. The fabricated triboelectric fibers follow a single-electrode (SE) triboelectric model where only the inner side of the fiber stays in contact with the electrode, while the outer side is subjected to periodic contact separation with a tribopositive material. During the contact separation cycle, the triboelectrification process generates static charge on the surface of two materials. The generated electrostatic charge creates an electrostatic imbalance, which induces an exchange of electrical charge between the ground and the electrode. The detailed working mechanism of the triboelectrification process is demonstrated in Figure 3.14a. At the initial noncontact state, there is no charge transfer between PVDF nanocomposite (tribonegative) and PEI (tribopositive) materials, which causes a net zero potential difference between the electrode and ground (Figure 3.14a(i)). In the compressed stage, PEI comes in contact with

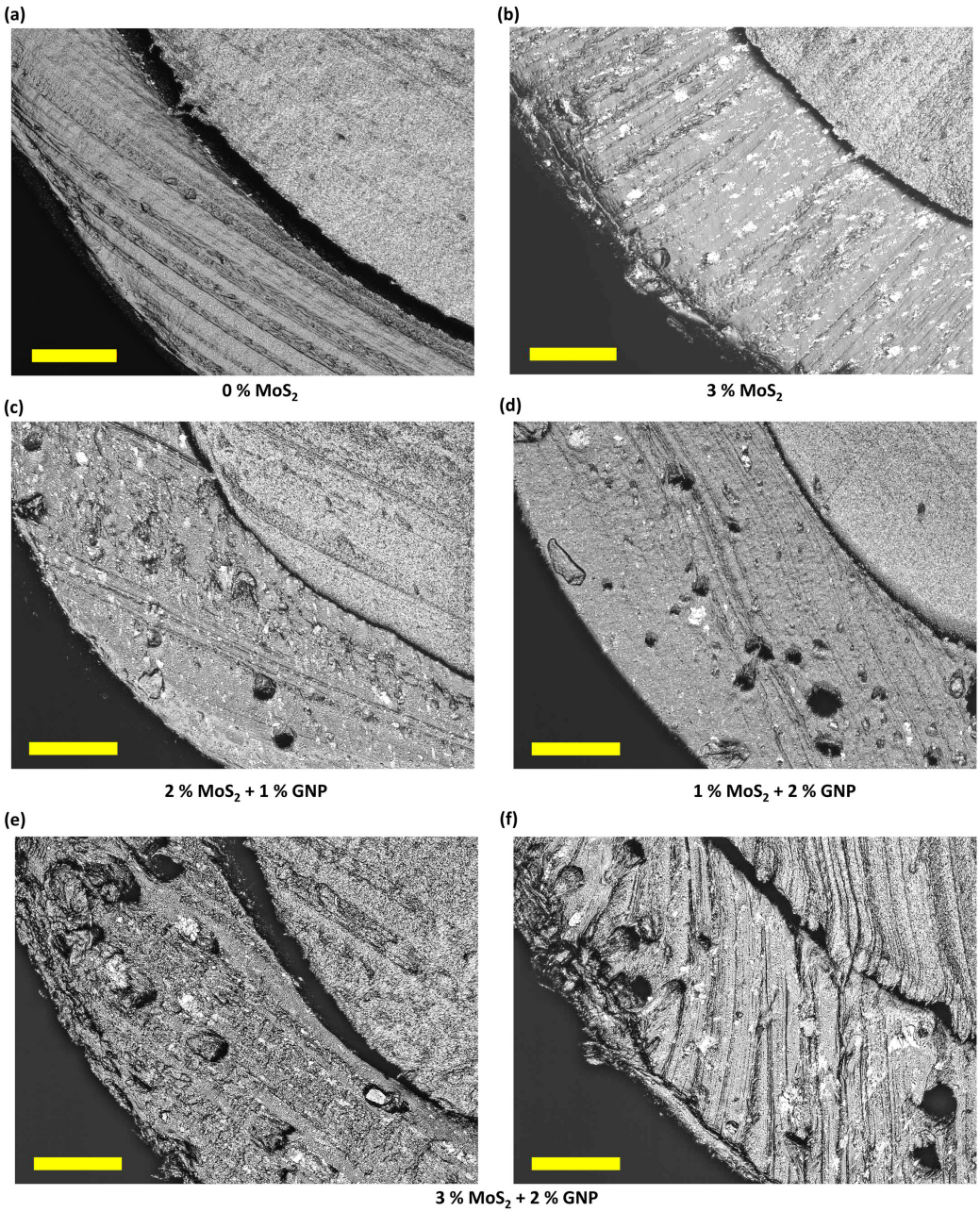

Figure 3.13: Comparative cross-sectional analysis of the pristine, single and dual nanoparticle integrated TENG fibers (a) 0 wt% MoS_2, (b) 3 wt% MoS_2, (c) 2 wt% MoS_2 and 1 wt% GNP, (d) 1 wt% MoS_2 and 2 wt% GNP and (e) 3 wt% MoS_2 and 2 wt% GNP.

PVDF nanocomposite fiber, and electron transfer occurs depending on the triboelectric polarity of the two materials[123]. Thus, a negative electrostatic charge is generated on the surface of the PVDF nanocomposite fibers due to charge injection from PEI. At this stage, there is still a net zero potential as two surfaces are in contact, neutralizing the opposite electrostatic potential (Figure 3.14a(ii)). In the releasing stage, when PEI starts to retract from the contact position with PVDF nanocomposite fiber, an electrostatic imbalance is induced between the electrode and ground, triggering an instantaneous flow of electrons from the electrode to the ground to neutralize the potential (Figure 3.14a(iii)). At the released stage, PEI is fully retracted, the electrostatic imbalance is fully neutralized, and the electron flow from the ground to the electrode ceases (Figure 3.14a(iv)). In the compressing stage, positively charged PEI again starts to descend towards the PVDF nanocomposite which again creates an electrostatic imbalance that is neutralized by the flow of electrons from the ground to the electrode, producing current flow from the opposite direction (Figure 3.14a(v)). Finally, when two layers contact again, equilibrium is reestablished. By this process, an AC signal is acquired from a complete contact separation cycle.

Enhancement of dipole orientation of PVDF to the conformation of the electroactive phase is directly related to the increment of triboelectric output of PVDF and PVDF-based nanocomposites[207, 217]. This alignment facilitates more charge transfers during the contact separation cycle, increasing the material's charge density. An increase in charge density results in an increment of triboelectric output[218]. A custom-made tapping device was used to conduct electrical characterization of the triboelectric fibers (Figure A1). An oscilloscope was used to measure open circuit voltage (V_{oc}), while short circuit current (I_{sc}) was measured using a current preamplifier setup. The PM0 fibers containing a β phase percentage of 35 demonstrated V_{oc} of 12.6 V at 5 Hz frequency (Figure 3.14b). The triboelectric fibers demonstrated an increasing triboelectric output with the increase of β phase percentage and reached 26.8 V for PM3 fiber at 5 Hz frequency (47.5% of β phase), a significant 2.12 times improvement compared to PM0 fiber. Moreover, the peak power output from the PM3 fiber increased to 17.64 μW at a matching load of 5 $M\Omega$, a three times increment compared to the

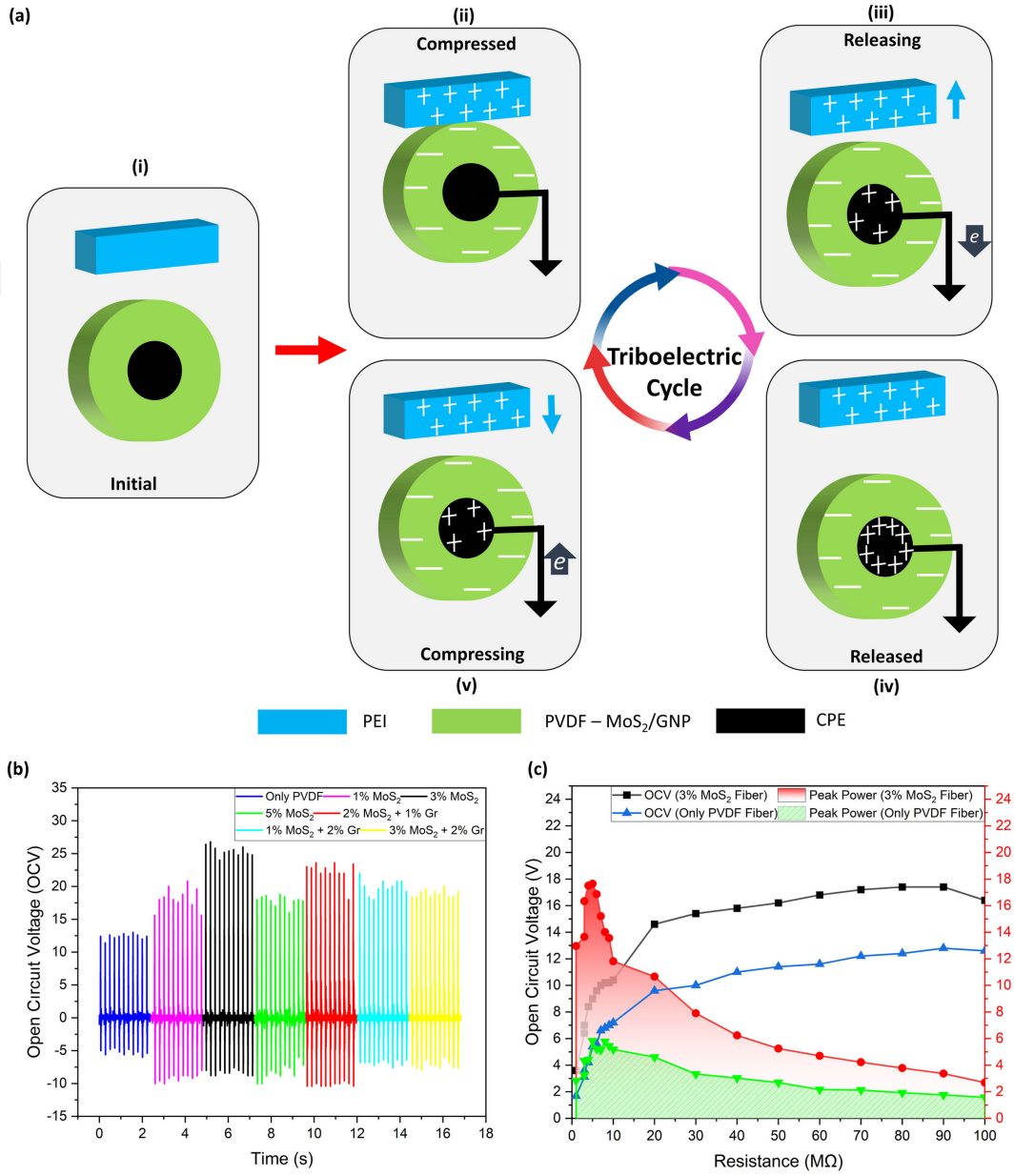

Figure 3.14: Electrical characterization of the TENG fiber. (a) The working mechanism of TENG fiber in the single electrode mode. (b) Open circuit voltage output of TENG fibers at different nanoparticle concentrations. (c) Peak power output comparison for 0 wt% and 3 wt% MoS_2 - PVDF fiber.

5.78 μW peak power output of PM0 fiber (Figure 3.14c). However, with further addition of nanoparticles, β phase formation decreased and reached 36.4% for PM5 fiber. Accordingly, the triboelectric output of PM5 fiber also experienced a reduction to 18.8 V. On the other hand, dual nanomaterial-integrated fibers with concentrations of 2 wt.% MoS_2 and 1 wt.% GNP showed slightly increased triboelectric output of 23.6 V. However, the further increase of GNP and MoS_2 showed a detrimental effect on the output, resulting in lower open circuit voltage values.

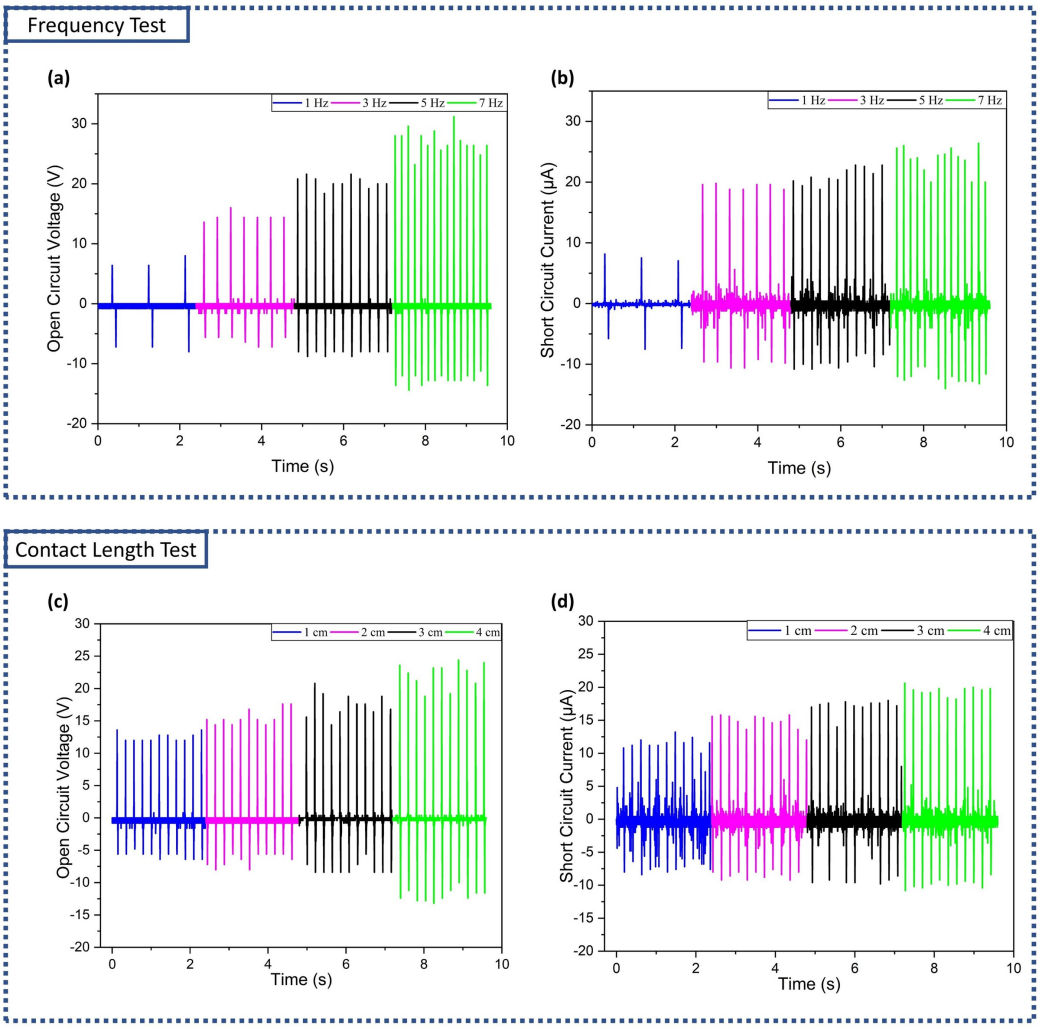

Figure 3.15: Electrical characterization of the PM3 fiber. (a) V_{oc} and (b) I_{sc} of the PM3 fiber at different frequencies. (c) V_{oc} and (d) I_{sc} or the PM3 fiber at different contact lengths.

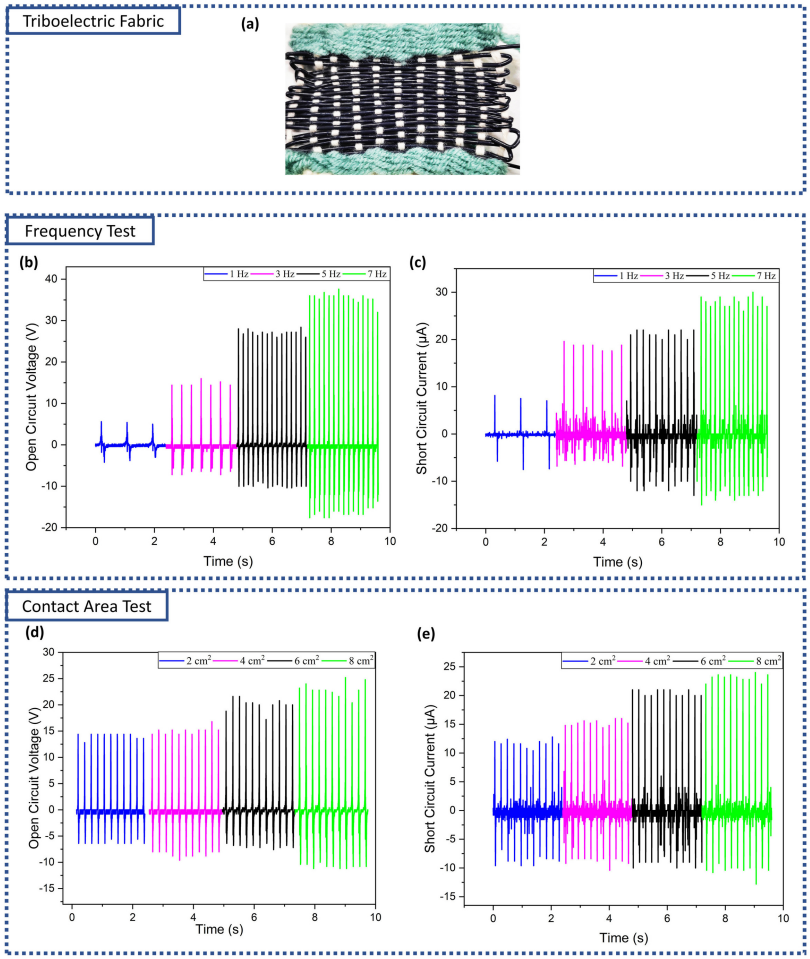

Figure 3.16: Electrical characterization of PM3 fabric. (a) Woven fabric structure comprised of PM3 fiber. (b) V_{oc} and (c) I_{sc} of the PM3 fabric at different frequency. (d) V_{oc} and (e) I_{sc} of the PM3 fabric at different contact area.

To further understand the electrical properties of PM3 fiber, contact frequency and contact area tests were carried out on the triboelectric fiber. V_{oc} was measured as 8 V for 1 Hz frequency, whereas it increased to 31.2 V at 7 Hz (Figure 3.15a). This significant increment can be attributed to the fact that, within the capacity of the tapping setup, an increase in contact frequency resulted in the exertion of an incremental force on TENG fiber, which resulted in an increase in contact area during the tapping cycle. The I_{sc} also demonstrated a similar

trend with 8.16 µA output at 1Hz and an increased output of 26.4 µA at 7 Hz contact frequency (Figure 3.15b). The increase in contact length also increased triboelectric output as an increment in contact length facilitates a higher number of electron transfers during tapping cycles. At 1 cm contact length, V_{oc} and I_{sc} were 13.6 V and 13.2 μA, respectively, which increased to 24.4 V and 20.6 μA for a 4 cm contact length (Figure 3.15c, 3.15d).

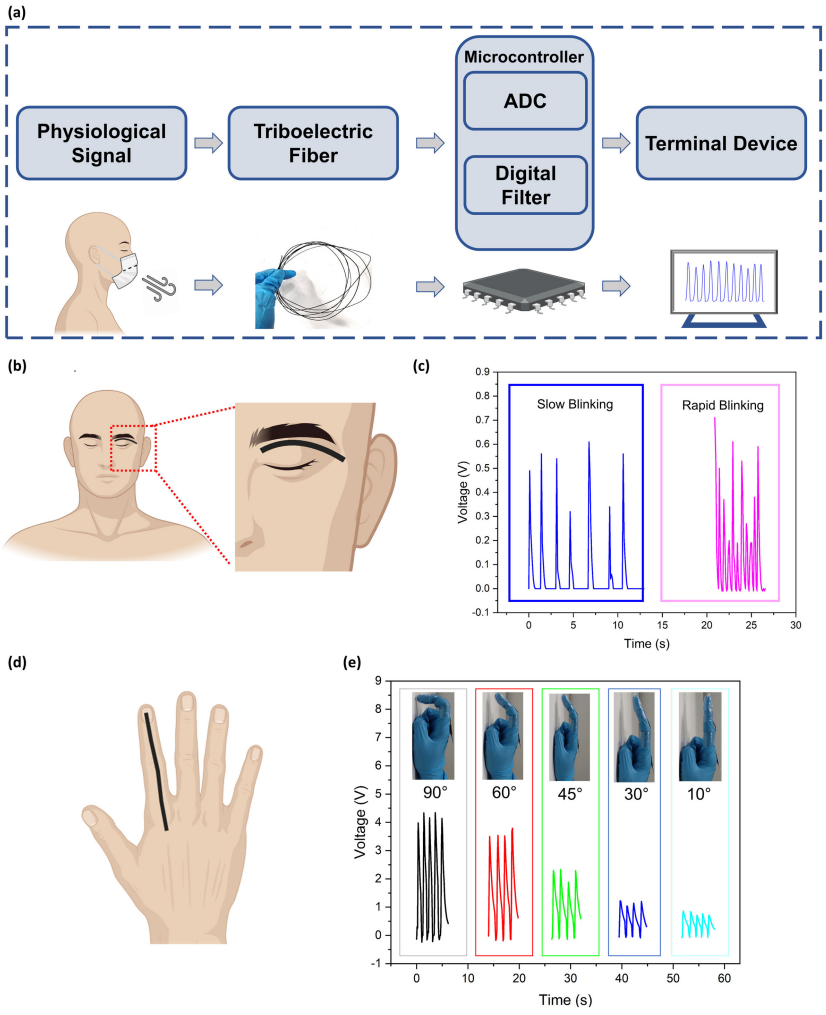

Figure 3.17: TENG fiber for skin interfaced sensor. (a) Schematic of the data acquisition and monitoring system. (b) Fiber sensor attached to the upper eyelid. (c) Sensor response during slow and fast blinking. (d) The fiber sensor is attached to the index finger. (e) Detection of various finger bending motions with attached sensor output.

Next, to determine the triboelectric output of the woven fabric structure, a 1-meter length of PM3 TENG was woven into the fabric and subjected to frequency and contact area tests (Figure 3.16a). The V_{oc} of the TENG fabric at 1 Hz frequency was 5.6 V, which increased to 37.6 v at 7 Hz (Figure 3.16b). Similarly, the I_{sc} value of 30 µA at 7 Hz frequency decreased to 8 µA at 1 Hz (Figure 3.16c). For the contact area test at 5 Hz, the V_{oc} for the 2 cm^2 contact area was 14.4 V. The value successively increased with the increment of contact area and reached 25.2 V for an 8 cm^2 contact area (Figure 3.16d). I_{sc} followed a similar pattern, demonstrating a value of 12.4 μA for a 2 cm^2 contact area, which increased to 24 μA for an 8 cm^2 contact area (Figure 3.16e).

3.6 Triboelectric Fiber for Wearable Sensors

Human gesture recognition with wearable devices is a research thrust that has gained massive popularity in recent decades[219, 220, 221, 222, 223, 224]. Metaverse, a futuristic iteration of the internet, where humans can interact, work, and socialize in a true virtual 3D space, requires human physical motion recognition more favorably in a wearable platform[225]. The current gold standard for physical motion recognition requires visual-based techniques integrating machine-learning algorithms, which are costly and energy-intensive[226]. Moreover, this process's effectiveness mainly depends on the availability of sufficient light and proper image acquisition, which requires a complex setup[227]. For this reason, wearable sensors have become an attractive alternative in this field, overcoming the limitations of the previous methods[228, 229, 230, 231, 232]. The superior electrical performance of the PM3 fiber paves the way for the utilization of the fiber as wearable sensors. The biocompatible nature of PVDF enables it to be directly interfaced with the skin without irritation[233, 234]. A data collection system was developed to continuously monitor signals from wearable sensors. The system includes three units - i) a triboelectric fiber for physiological signal acquisition, ii) a microcontroller device with analog-to-digital conversion (ADC) and digital signal filtering, and iii) a terminal device to visualize the data (Figure 3.17a). The fiber sensor was attached to the upper eyelid with adhesive tapes

to demonstrate PM3 fiber's performance in physical motion monitoring (Figure 3.17b). With the opening and closure cycle of the eyelid, the fiber touched the skin and created triboelectric output. It was possible to detect fast and slow blinking motion with the sensing setup (Figure 3.17c). Hand gesture recognition is another critical issue. The fabricated sensor showed superior performance in finger motion monitoring, demonstrating its potential on wearable gloves-based devices. For demonstration, the sensor was attached to the index finger with adhesive tapes on both ends (Figure 3.17d). With the finger bending motion, there was an increased strain on the fiber that allowed the sensor to increase contact area with the skin. Thus, at a higher angle of finger bending motion, the sensor produced higher output, indicating the extent of finger motion of an individual(Figure 3.17e).

3.7 Triboelectric Face Mask for Respiration Monitoring

Respiration is a vital physiological parameter indicative of lung-induced physiological disorders such as asthma, pneumonia, chronic obstructive pulmonary disease (COPD), cardiac arrest, coughing, and sleep apnea[235, 236, 237, 238, 239]. The respiration process provides oxygen for the cellular metabolic process, generating energy by breaking down glucose through glycolysis and the Krebs cycle. Increased demand in the metabolic process is accompanied by an increase in respiration frequency[240, 241, 242]. Sleep is another physiological activity deeply connected with respiration. At the rapid eye movements (REM) stage, sleeping is associated with the greatest cardiac and respiratory instability. On the other hand, respiration of non-rapid eye movements (NREM) sleep stage is regular and mostly under metabolic control[243, 244]. Furthermore, respiration rate is also an indication of intense physiological activity. During excessively higher muscle activity, the human body produces more carbon dioxide by using oxygen to generate energy. To cope with this physical demand, breathing rate increases[245]. Thus, continuous respiration monitoring during sleeping and waking hours can provide

an essential understanding of the health condition and physical activity[241]. Wearable surgical masks for respiration monitoring have recently gained popularity during the Covid-19 pandemic period for their ease of usage. One major advantage of using a triboelectric sensing element in surgical masks is that it can harness exhaled breath as an energy source to operate without requiring external power source. Previously reported respiration monitoring masks employed the triboelectric layer as a separate layer over the mask or changed the mask's design, significantly increasing the complexity and cost of the wearable device while promoting localized inhibition of the breathability of the mask's surface[246, 247, 248, 249, 250]. Thus, devising a surgical mask that can ensure simple and cost-effective continuous respiration monitoring is an essential limitation that has not been addressed yet. Herein, a simple method is proposed for weaving PM3 triboelectric fiber with commercially available surgical face masks. The mask comprised three separate layers: polypropylene, melt-blown filter, and polypropylene, as shown in Figure 3.18a.

Polypropylene (PP) is a tribopositive material that can donate electrons to PVDF nanocomposite fiber during contact separation[251]. The mask-based sensor can analyze the breathing cycle accurately to provide data related to human breathing (Figure 3.18b). At the resting position (when no respiration occurs), there was minimum contact between PP and PM3 (Figure 3.18c(i)). No output signal was acquired at this stage, denoted by the yellow portion of the signal output in Figure 3.18c (i). When the air was exhaled during a breathing cycle, it created an outward flow of air that pushed the nanocomposite fiber against the PP layer of the mask (Figure 18c (ii)). This phenomenon created an electrostatic imbalance in the triboelectric fiber, inducing an output signal denoted by the turquoise blue part in the signal output in Figure 3.18b. Finally, when the air was inhaled (Figure 3.18c (iii)), the fiber returned to its original relaxed position, and a downward slope was obtained in the triboelectric fiber denoted by the lawn green portion in the signal output in Figure 18b before reaching the ground state. The devised mask was experimented with various simulated breathing conditions to demonstrate its applicability in real-world conditions. Due to the superior sensitivity of the fiber, it can differentiate between various breathing conditions with

the change of signal peak output and frequency. During diaphragmatic breathing, 100% of the capacity of the lungs is utilized by exchanging the maximum air in one breathing cycle[252]. The high air pressure generated during the breathing allowed maximum contact between the fiber and PP, allowing a voltage output of 1.12 V (Figure 3.18d (i)). During relaxed breathing, the sensor also produced a stable output of 0.25 V (Figure 3.18d (ii)). Fast breathing or hyperpnea is a physical condition that requires an increase in depth and rate of breathing associated with physiological factors such as exercise or increased metabolic rate[253].

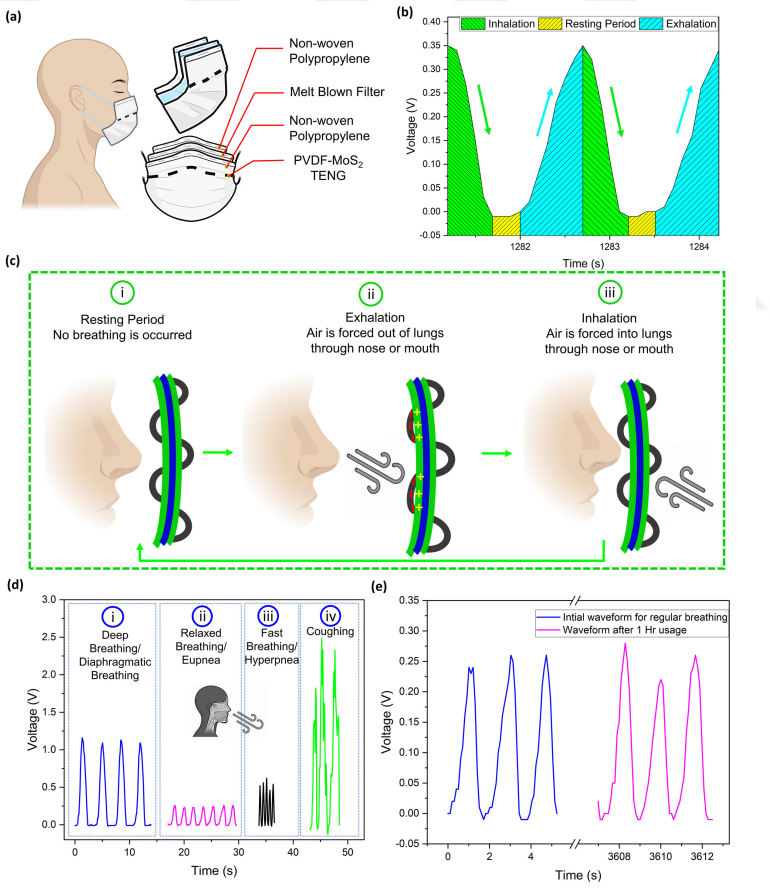

Figure 3.18: Wearable triboelectric mask for respiration monitoring. (a) The schematic of the commercial mask, TENG fiber directly woven into the mask. (b) Respiration cycle. (c) Respiration sensor working mechanism. (d) Detection of various respiration stages with TENG mask sensor. (e) Long-time stability of the signal output from the TENG sensor integrated with a wearable face mask.

The device mask can differentiate fast breathing from normal breathing by detecting increased breathing rate and increased depth of breathing with an output voltage of 0.6 V (Figure 3.18d (iii)). It was also possible to detect coughing signals from the wearable mask with multiple shoulder peaks that appeared on the signal in one breathing cycle due to coughing (Figure 3.18d (iv)). The wearable mask sensor's superior sensitivity, cost-effectiveness, and user-friendly properties set itself as a potential candidate for detecting various breathing disorders, such as dyspnea, orthopnea, bradypnea, tachypnea, and obstructive sleep apnea (OSA). Even though breathing disorders are not life-threatening by themselves, they are symptoms of various fatal diseases, including heart failure, acute myocardial ischemia, pulmonary embolism, obstruction of the upper airway by aspiration or anaphylaxis, pulmonary infection, cardiac tamponade, and pneumothorax[254]. Thus, their timely detection through breathing analysis is essential for reducing the suffering of the patients. This approach highlights the promising prospects of TENG-based wearable devices for physiological data collection, contributing to advancements in human well-being monitoring. The sensor output signal was also stable during continuous use of 1hr as a face mask (Figure 3.18e).

3.8 Summary

This study demonstrated the successful fabrication and characterization of the thermally drawn MoS_2-integrated triboelectric nanocomposite fibers for the first time. The β phase content in the fiber demonstrated a maximum improvement of 47.5% with only 3 wt% nanomaterial integration. The open circuit voltage and peak power output of PM3 fiber increased 2.12 and 3 times, respectively, compared to PM0 fiber. It was also observed that nanoparticle agglomeration of the triboelectric fiber beyond 3 wt% thresholds was responsible for reducing triboelectric property at higher concentrations of MoS_2. The superior triboelectric output of the PM3 fiber made it suitable for application in wearable sensing devices where high sensitivity is required. The sensor was utilized for blinking and hand gesture monitoring. Finally, a low-cost wearable mask was designed, which showed great potential for respiration monitoring.

Chapter 4

Conclusion and future prospective

This thesis demonstrates scalable fabrication of nanomaterial (GNP and MoS_2) integrated PVDF triboelectric fibers. The fibers are fabricated in a single step process decreasing the manufacturing cost of multilateral integrated TENGs. The addition of low dimensional materials and their interfacial interaction with PVDF significantly improves the electro-active phase in PVDF which increases triboelectric charge density in the functional layer by high charge generation and electron trapping effect. The fibers are flexible enough to be utilized as a regular textile yarn to weave textile structures. The fibers are also biocompatible allowing their use directly as on skin sensors without any skin irritation.

The first projects demonstrate, the scalable fabrication of graphene-integrated PVDF nanocomposite fiber using a thermal drawing process. With the integration of 5% graphene into the PVDF fibers, the open circuit voltage and short circuit current improved by 1.41 and 1.48 times, respectively. The TENG fabric achieved a maximum power output of 32.14 μW at a matching load of 7 $M\Omega$ and a power density of 53.57 $\mu W m^{-2}$. The high temperature stability of the triboelectric fiber is also studied as triboelectric fibers may experience high temperature depending on the user applications. The TENG fiber demonstrates excellent

output stability from room temperature to 80°C. Additionally, the fibers exhibited excellent stability under harsh environmental conditions, including alkaline medium, high/low temperatures, multiple washing cycles, and prolonged usage. Utilizing the flexible nature of the triboelectric PVDF nanocomposite fibers, a woven fabric structure is prepared which is used to fabricate a smart sock. The sock can detect and differentiate different walking and running stages and can be employed for gait analysis. The fibers can also be implemented with arm and knee sleeve to monitor and detect athletics movement in high intensity sports. Finally, the energy harvesting capability is also shown by hand tapping the woven fabric structure and transferred this energy to charge a capacitor which can run small low powered electronics.

The second work focuses on further improving the triboelectric property and output of the PVDF textile TENG. MoS_2 with its semiconducting nature and ability to interact with end groups of PVDF to modulate dielectric nanocomposite, is an ideal candidate for affecting further improvement of the PVDF nanocomposite TENG. The fabrication of thermally drawn PVDF TENG fibers incorporating various concentrations of MoS_2 is introduced. The enhanced β phase properties in the nanocomposite fiber improve the triboelectric output, with 3 wt% MoS_2 - PVDF fiber demonstrating a maximum peak power output of 17.64 μW, a threefold increase compared to 0 wt% MoS_2 - PVDF fiber. The study also explores the simultaneous integration of multiple nanomaterials, such as MoS_2 and graphene nanoplatelet, to analyze the β phase formation and electrical performance of the triboelectric fiber. Finally, the thermally drawn MoS_2 - PVDF TENG fiber is employed for respiration monitoring and as on skin sensor. A smart face mask is prepared with triboelectric fiber. Harnessing the superior sensitivity of the MoS_2 - PVDF TENG fiber, the mask can detect berating motion due to the periodic contact separation with mask fabric with MoS_2 - PVDF TENG fiber. The breathing analysis can provide enormous amount of physiological data that can be used to analyze and predict physiological condition. The fiber sensor is also used as on skin sensor for finer motion and blinking detection.

We hope that, the improved performance of our nanocomposite fibers will pave the way for further development that will make the TENG fiber based wearable

devices readily available to the user end. In the next stage of our development, we aim to introduce microstructure into the TENG fiber which will significantly increase the contact area and thus triboelectric charge transfer keeping the fiber diameter in the acceptable range for textile processing. We predict the current work on TENG fiber will bring significant gain in the decentralization of biomechanical analysis and healthcare facilities allowing real time monitoring opportunity for athletes and critical patients. Moreover, this endeavor may also replace many rigid expensive wearable and medical device making the wearables affordable for mass population. Over the next decade we envision that, smart textile TENGs will poise to become integrated components of daily life, offering sustainable all-in-one power supply systems and serving as essential support tools within the evolving landscape of the Internet of Things (IoT) and artificial intelligence (AI).

Bibliography

[1] C. Hou, T. Chen, Y. Li, M. Huang, Q. Shi, H. Liu, L. Sun, and C. Lee, "A rotational pendulum based electromagnetic/triboelectric hybrid-generator for ultra-low-frequency vibrations aiming at human motion and blue energy applications," *Nano Energy*, vol. 63, p. 103871, 2019.

[2] M. Salauddin, R. Toyabur, P. Maharjan, and J. Y. Park, "High performance human-induced vibration driven hybrid energy harvester for powering portable electronics," *Nano Energy*, vol. 45, pp. 236–246, 2018.

[3] S. Korkmaz and I. A. Kariper, "Batio3-based nanogenerators: fundamentals and current status," *Journal of Electroceramics*, vol. 48, no. 1, pp. 8–34, 2022.

[4] A. Libanori, J. Soto, J. Xu, Y. Song, J. Zarubova, T. Tat, X. Xiao, S. Z. Yue, S. J. Jonas, S. Li, *et al.*, "Self-powered programming of fibroblasts into neurons via a scalable magnetoelastic generator array," *Advanced Materials*, vol. 35, no. 7, p. 2206933, 2023.

[5] Y. Yang, K. C. Pradel, Q. Jing, J. M. Wu, F. Zhang, Y. Zhou, Y. Zhang, and Z. L. Wang, "Thermoelectric nanogenerators based on single sb-doped zno micro/nanobelts," *ACS nano*, vol. 6, no. 8, pp. 6984–6989, 2012.

[6] W. Zhang, Y. Shi, Y. Li, X. Chen, and H. Shen, "A review: Contact electrification on special interfaces," *Frontiers in Materials*, vol. 9, p. 909746, 2022.

[7] K. Dong, Y. Hu, J. Yang, S.-W. Kim, W. Hu, and Z. L. Wang, "Smart textile triboelectric nanogenerators: Current status and perspectives," *MRS Bulletin*, vol. 46, no. 6, pp. 512–521, 2021.

[8] M. M. Hasan, M. S. B. Sadeque, I. Albasar, H. Pecenek, F. K. Dokan, M. S. Onses, and M. Ordu, "Scalable fabrication of mxene-pvdf nanocomposite triboelectric fibers via thermal drawing," *Small*, vol. 19, no. 6, p. 2206107, 2023.

[9] M. S. B. Sadeque, M. Rahman, M. M. Hasan, and M. Ordu, "Graphene nanoplatelet integrated thermally drawn pvdf triboelectric nanocomposite fibers for extreme environmental conditions," *Advanced Electronic Materials*, vol. 10, no. 4, p. 2300643, 2024.

[10] Y. Wu, S. S. Mechael, and T. B. Carmichael, "Wearable e-textiles using a textile-centric design approach," *Accounts of Chemical Research*, vol. 54, no. 21, pp. 4051–4064, 2021.

[11] K. Du, R. Lin, L. Yin, J. S. Ho, J. Wang, and C. T. Lim, "Electronic textiles for energy, sensing, and communication," *IScience*, vol. 25, no. 5, 2022.

[12] V. Kaushik, J. Lee, J. Hong, S. Lee, S. Lee, J. Seo, C. Mahata, and T. Lee, "Textile-based electronic components for energy applications: Principles, problems, and perspective," *Nanomaterials*, vol. 5, no. 3, pp. 1493–1531, 2015.

[13] X. Li and Y. Sun, "Wearete: A scalable wearable e-textile triboelectric energy harvesting system for human motion scavenging," *Sensors*, vol. 17, no. 11, p. 2649, 2017.

[14] Z. L. Wang, G. Zhu, Y. Yang, S. Wang, and C. Pan, "Progress in nanogenerators for portable electronics," *Materials today*, vol. 15, no. 12, pp. 532–543, 2012.

[15] M. Ma, Z. Kang, Q. Liao, Q. Zhang, F. Gao, X. Zhao, Z. Zhang, and Y. Zhang, "Development, applications, and future directions of triboelectric nanogenerators," *Nano Research*, vol. 11, pp. 2951–2969, 2018.

[16] Z. Lin, J. Chen, and J. Yang, "Recent progress in triboelectric nanogenerators as a renewable and sustainable power source," *Journal of Nanomaterials*, vol. 2016, no. 1, p. 5651613, 2016.

[17] A. Chen, C. Zhang, G. Zhu, and Z. L. Wang, "Polymer materials for high-performance triboelectric nanogenerators," *Advanced Science*, vol. 7, no. 14, p. 2000186, 2020.

[18] H. Zou, Y. Zhang, L. Guo, P. Wang, X. He, G. Dai, H. Zheng, C. Chen, A. C. Wang, C. Xu, *et al.*, "Quantifying the triboelectric series," *Nature communications*, vol. 10, no. 1, p. 1427, 2019.

[19] J. W. Lee, S. Jung, T. W. Lee, J. Jo, H. Y. Chae, K. Choi, J. J. Kim, J. H. Lee, C. Yang, and J. M. Baik, "High-output triboelectric nanogenerator based on dual inductive and resonance effects-controlled highly transparent polyimide for self-powered sensor network systems," *Advanced Energy Materials*, vol. 9, no. 36, p. 1901987, 2019.

[20] S.-H. Shin, Y. H. Kwon, Y.-H. Kim, J.-Y. Jung, M. H. Lee, and J. Nah, "Triboelectric charging sequence induced by surface functionalization as a method to fabricate high performance triboelectric generators," *ACS nano*, vol. 9, no. 4, pp. 4621–4627, 2015.

[21] S. Li, Y. Fan, H. Chen, J. Nie, Y. Liang, X. Tao, J. Zhang, X. Chen, E. Fu, and Z. L. Wang, "Manipulating the triboelectric surface charge density of polymers by low-energy helium ion irradiation/implantation," *Energy & Environmental Science*, vol. 13, no. 3, pp. 896–907, 2020.

[22] A. Šutka, K. Mālnieks, A. Linarts, M. Timusk, V. Jurķāns, I. Gorņevs, J. Blūms, A. Bērziņa, U. Joost, and M. Knite, "Inversely polarised ferroelectric polymer contact electrodes for triboelectric-like generators from identical materials," *Energy & Environmental Science*, vol. 11, no. 6, pp. 1437–1443, 2018.

[23] W. Seung, H.-J. Yoon, T. Y. Kim, H. Ryu, J. Kim, J.-H. Lee, J. H. Lee, S. Kim, Y. K. Park, Y. J. Park, *et al.*, "Boosting power-generating performance of triboelectric nanogenerators via artificial control of ferroelectric

polarization and dielectric properties," *Advanced Energy Materials*, vol. 7, no. 2, p. 1600988, 2017.

[24] G. Cheng, Z.-H. Lin, L. Lin, Z.-l. Du, and Z. L. Wang, "Pulsed nanogenerator with huge instantaneous output power density," *Acs Nano*, vol. 7, no. 8, pp. 7383–7391, 2013.

[25] Y. Bai, L. Xu, S. Lin, J. Luo, H. Qin, K. Han, and Z. L. Wang, "Charge pumping strategy for rotation and sliding type triboelectric nanogenerators," *Advanced Energy Materials*, vol. 10, no. 21, p. 2000605, 2020.

[26] D. Liu, X. Yin, H. Guo, L. Zhou, X. Li, C. Zhang, J. Wang, and Z. L. Wang, "A constant current triboelectric nanogenerator arising from electrostatic breakdown," *Science advances*, vol. 5, no. 4, p. eaav6437, 2019.

[27] J. Chen, H. Guo, C. Hu, and Z. L. Wang, "Robust triboelectric nanogenerator achieved by centrifugal force induced automatic working mode transition," *Advanced Energy Materials*, vol. 10, no. 23, p. 2000886, 2020.

[28] J. Fu, G. Xu, H. Wu, C. Li, and Y. Zi, "Liquid-interfaces-based triboelectric nanogenerator: An emerging power generation method from liquid-energy nexus," *Advanced energy and sustainability research*, vol. 3, no. 9, p. 2200051, 2022.

[29] J. P. Lee, J. W. Lee, and J. M. Baik, "The progress of pvdf as a functional material for triboelectric nanogenerators and self-powered sensors," *Micromachines*, vol. 9, no. 10, p. 532, 2018.

[30] X. Chen, X. Han, and Q.-D. Shen, "Pvdf-based ferroelectric polymers in modern flexible electronics," *Advanced Electronic Materials*, vol. 3, no. 5, p. 1600460, 2017.

[31] J. Seo, S. Hajra, M. Sahu, and H. J. Kim, "Effect of cilia microstructure and ion injection upon single-electrode triboelectric nanogenerator for effective energy harvesting," *Materials Letters*, vol. 304, p. 130674, 2021.

[32] S. Cui, L. Zhou, D. Liu, S. Li, L. Liu, S. Chen, Z. Zhao, W. Yuan, Z. L. Wang, and J. Wang, "Improving performance of triboelectric nanogenerators by dielectric enhancement effect," *Matter*, vol. 5, no. 1, pp. 180–193, 2022.

[33] X. Yu, Z. Liu, X. Yang, Y. Wang, J. Zhang, J. Duan, L. Liu, and Q. Tang, "Crystal-plane controlled spontaneous polarization of inorganic perovskite toward boosting triboelectric surface charge density," *ACS Applied Materials & Interfaces*, vol. 13, no. 22, pp. 26196–26203, 2021.

[34] S. Wang, Y. Zi, Y. S. Zhou, S. Li, F. Fan, L. Lin, and Z. L. Wang, "Molecular surface functionalization to enhance the power output of triboelectric nanogenerators," *Journal of Materials Chemistry A*, vol. 4, no. 10, pp. 3728–3734, 2016.

[35] H. Jiang, H. Lei, Z. Wen, J. Shi, D. Bao, C. Chen, J. Jiang, Q. Guan, X. Sun, and S.-T. Lee, "Charge-trapping-blocking layer for enhanced triboelectric nanogenerators," *Nano Energy*, vol. 75, p. 105011, 2020.

[36] R. Zhang and H. Olin, "Advances in inorganic nanomaterials for triboelectric nanogenerators," *ACS Nanoscience Au*, vol. 2, no. 1, pp. 12–31, 2021.

[37] M. Seol, S. Kim, Y. Cho, K.-E. Byun, H. Kim, J. Kim, S. K. Kim, S.-W. Kim, H.-J. Shin, and S. Park, "Triboelectric series of 2d layered materials," *Advanced Materials*, vol. 30, no. 39, p. 1801210, 2018.

[38] Y. Nurmakanov, G. Kalimuldina, G. Nauryzbayev, D. Adair, and Z. Bakenov, "Structural and chemical modifications towards high-performance of triboelectric nanogenerators," *Nanoscale Research Letters*, vol. 16, no. 1, p. 122, 2021.

[39] Y. Liu, J. Ping, and Y. Ying, "Recent progress in 2d-nanomaterial-based triboelectric nanogenerators," *Advanced Functional Materials*, vol. 31, no. 17, p. 2009994, 2021.

[40] M. K. Ahmed, A. Bagheri Behboud, A. Kurucu, G. Kurt Çömlekçi, and M. Ordu, "Improved mechanical properties of the e-glass fibres through tio2

nanoparticle coating," *Materials Science and Technology*, vol. 39, no. 11, pp. 1304–1312, 2023.

[41] A. B. Behboud, M. K. Ahmed, A. Kurucu, G. K. Çömlekçi, and M. Ordu, "Zirconia nanoparticle coating for high-strength and alkali-resistant glass fibers," *Journal of Non-Crystalline Solids*, vol. 619, p. 122571, 2023.

[42] M. S. B. Sadeque, H. K. Chowdhury, M. Rafique, M. A. Durmuş, M. K. Ahmed, M. M. Hasan, A. Erbaş, İ. Sarpkaya, F. Inci, and M. Ordu, "Hydrogel-integrated optical fiber sensors and their applications: a comprehensive review," *Journal of Materials Chemistry C*, vol. 11, no. 28, pp. 9383–9424, 2023.

[43] S. T. Mahmud, M. M. Hasan, S. Bain, S. T. Rahman, M. Rhaman, M. M. Hossain, and M. Ordu, "Multilayer mxene heterostructures and nanohybrids for multifunctional applications: a review," *ACS Materials Letters*, vol. 4, no. 6, pp. 1174–1206, 2022.

[44] M. R. Repon, D. Mikučionienė, R. Milašius, T. K. Paul, C. M. Ahmed, S. Z. Hussain, and A. Haji, "Progress in mxene integrated wearable textile devices for thermotherapy," *Materials Today Communications*, p. 107251, 2023.

[45] M. A. Jalil, A. F. Halim, M. Moniruzzaman, M. T. Hossain, and S. Z. Hussain, "Nano materials in textile processing," in *Advanced Technology in Textiles: Fibre to Apparel*, pp. 323–344, Springer, 2023.

[46] D. L. Vu, C. D. Le, and K. K. Ahn, "Functionalized graphene oxide/polyvinylidene fluoride composite membrane acting as a triboelectric layer for hydropower energy harvesting," *International Journal of Energy Research*, vol. 46, no. 7, pp. 9549–9559, 2022.

[47] T. Huang, M. Lu, H. Yu, Q. Zhang, H. Wang, and M. Zhu, "Enhanced power output of a triboelectric nanogenerator composed of electrospun nanofiber mats doped with graphene oxide," *Scientific Reports*, vol. 5, no. 1, p. 13942, 2015.

[48] L. Shi, H. Jin, S. Dong, S. Huang, H. Kuang, H. Xu, J. Chen, W. Xuan, S. Zhang, S. Li, *et al.*, "High-performance triboelectric nanogenerator based on electrospun pvdf-graphene nanosheet composite nanofibers for energy harvesting," *Nano Energy*, vol. 80, p. 105599, 2021.

[49] G. Loke, W. Yan, T. Khudiyev, G. Noel, and Y. Fink, "Recent progress and perspectives of thermally drawn multimaterial fiber electronics," *Advanced Materials*, vol. 32, no. 1, p. 1904911, 2020.

[50] C. Han, Z. Cao, Z. Yuan, Z. Zhang, X. Huo, L. Zhang, Z. Wu, and Z. L. Wang, "Hybrid triboelectric-electromagnetic nanogenerator with a double-sided fluff and double halbach array for wave energy harvesting," *Advanced Functional Materials*, vol. 32, no. 36, p. 2205011, 2022.

[51] J. Jo, S. Panda, N. Kim, S. Hajra, S. Hwang, H. Song, J. Shukla, B. K. Panigrahi, V. Vivekananthan, J. Kim, *et al.*, "Hybrid nanogenerator for self-powered object recognition," *Journal of Science: Advanced Materials and Devices*, vol. 9, no. 2, p. 100693, 2024.

[52] M. Zhu, Y. Huang, W. S. Ng, J. Liu, Z. Wang, Z. Wang, H. Hu, and C. Zhi, "3d spacer fabric based multifunctional triboelectric nanogenerator with great feasibility for mechanized large-scale production," *Nano energy*, vol. 27, pp. 439–446, 2016.

[53] W. Gong, C. Hou, J. Zhou, Y. Guo, W. Zhang, Y. Li, Q. Zhang, and H. Wang, "Continuous and scalable manufacture of amphibious energy yarns and textiles," *Nature communications*, vol. 10, no. 1, p. 868, 2019.

[54] Z. Feng, S. Yang, S. Jia, Y. Zhang, S. Jiang, L. Yu, R. Li, G. Song, A. Wang, T. Martin, *et al.*, "Scalable, washable and lightweight triboelectric-energy-generating fibers by the thermal drawing process for industrial loom weaving," *Nano Energy*, vol. 74, p. 104805, 2020.

[55] C. Dong, A. Leber, T. Das Gupta, R. Chandran, M. Volpi, Y. Qu, T. Nguyen-Dang, N. Bartolomei, W. Yan, and F. Sorin, "High-efficiency super-elastic liquid metal based triboelectric fibers and textiles," *Nature communications*, vol. 11, no. 1, p. 3537, 2020.

[56] R. Nishimoto, Y. Sato, J. Wu, T. Saizaki, M. Kubo, M. Wang, H. Abe, I. Richard, T. Yoshinobu, F. Sorin, *et al.*, "Thermally drawn cnt-based hybrid nanocomposite fiber for electrochemical sensing," *Biosensors*, vol. 12, no. 8, p. 559, 2022.

[57] T. Iwama, Y. Guo, S. Handa, K. Y. Inoue, T. Yoshinobu, F. Sorin, and H. Shiku, "Thermally-drawn multi-electrode fibers for bipolar electrochemistry and magnified electrochemical imaging," *Advanced Materials Technologies*, vol. 7, no. 5, p. 2101066, 2022.

[58] I. Hwang, Z. Guan, C. Cao, W. Tang, C. O. Chui, and X. Li, "Nanoparticles suppress fluid instabilities in the thermal drawing of ultralong nanowires," *Nature communications*, vol. 11, no. 1, p. 5932, 2020.

[59] J. Andreu-Perez, D. R. Leff, H. M. Ip, and G.-Z. Yang, "From wearable sensors to smart implants—toward pervasive and personalized healthcare," *IEEE Transactions on Biomedical Engineering*, vol. 62, no. 12, pp. 2750–2762, 2015.

[60] S. Cheng, Z. Gu, L. Zhou, M. Hao, H. An, K. Song, X. Wu, K. Zhang, Z. Zhao, Y. Dong, *et al.*, "Recent progress in intelligent wearable sensors for health monitoring and wound healing based on biofluids," *Frontiers in Bioengineering and Biotechnology*, vol. 9, p. 765987, 2021.

[61] R. Yin, D. Wang, S. Zhao, Z. Lou, and G. Shen, "Wearable sensors-enabled human–machine interaction systems: from design to application," *Advanced Functional Materials*, vol. 31, no. 11, p. 2008936, 2021.

[62] L. Donisi, G. Cesarelli, N. Pisani, A. M. Ponsiglione, C. Ricciardi, and E. Capodaglio, "Wearable sensors and artificial intelligence for physical ergonomics: A systematic review of literature," *Diagnostics*, vol. 12, no. 12, p. 3048, 2022.

[63] A. Angelucci, M. Cavicchioli, I. A. Cintorrino, G. Lauricella, C. Rossi, S. Strati, and A. Aliverti, "Smart textiles and sensorized garments for physiological monitoring: A review of available solutions and techniques," *Sensors*, vol. 21, no. 3, p. 814, 2021.

[64] M. Su, P. Li, X. Liu, D. Wei, and J. Yang, "Textile-based flexible capacitive pressure sensors: A review," *Nanomaterials*, vol. 12, no. 9, p. 1495, 2022.

[65] G. Hossain, I. Z. Hossain, and G. Grabher, "Piezoresistive smart-textile sensor for inventory management record," *Sensors and Actuators A: Physical*, vol. 315, p. 112300, 2020.

[66] A. Leal-Junior, L. Avellar, A. Frizera, and C. Marques, "Smart textiles for multimodal wearable sensing using highly stretchable multiplexed optical fiber system," *Scientific Reports*, vol. 10, no. 1, p. 13867, 2020.

[67] L. Chen, T. Wang, Y. Shen, F. Wang, and C. Chen, "Stretchable woven fabric-based triboelectric nanogenerator for energy harvesting and self-powered sensing," *Nanomaterials*, vol. 13, no. 5, p. 863, 2023.

[68] M. Rahman and M. Ordu, "Long-length 3d printed hollow-core polymer optical fiber for wideband light guidance," *Optical Fiber Technology*, vol. 81, p. 103512, 2023.

[69] M. M. Hasan, M. M. Hossain, and H. K. Chowdhury, "Two-dimensional mxene-based flexible nanostructures for functional nanodevices: a review," *Journal of Materials Chemistry A*, vol. 9, no. 6, pp. 3231–3269, 2021.

[70] M. M. Hasan and M. M. Hossain, "Nanomaterials-patterned flexible electrodes for wearable health monitoring: a review," *Journal of Materials Science*, vol. 56, no. 27, pp. 14900–14942, 2021.

[71] J. A. Rogers, T. Someya, and Y. Huang, "Materials and mechanics for stretchable electronics," *science*, vol. 327, no. 5973, pp. 1603–1607, 2010.

[72] H. Sun, Y. Zhang, J. Zhang, X. Sun, and H. Peng, "Energy harvesting and storage in 1d devices," *Nature Reviews Materials*, vol. 2, no. 6, pp. 1–12, 2017.

[73] Q. Zhu, T. Wu, and N. Wang, "From piezoelectric nanogenerator to non-invasive medical sensor: A review," *Biosensors*, vol. 13, no. 1, p. 113, 2023.

[74] W.-G. Kim, D.-W. Kim, I.-W. Tcho, J.-K. Kim, M.-S. Kim, and Y.-K. Choi, "Triboelectric nanogenerator: Structure, mechanism, and applications," *ACS nano*, vol. 15, no. 1, pp. 258–287, 2021.

[75] G. Tian, Y. Shi, J. Deng, W. Yu, L. Yang, Y. Lu, Y. Zhao, X. Jin, Q. Ke, and C. Huang, "Low-cost, scalable fabrication of all-fabric piezoresistive sensors via binder-free, in-situ welding of carbon nanotubes on bicomponent nonwovens," *Advanced Fiber Materials*, vol. 6, no. 1, pp. 120–132, 2024.

[76] X. Zhao, A. Nashalian, I. W. Ock, S. Popoli, J. Xu, J. Yin, T. Tat, A. Libanori, G. Chen, Y. Zhou, *et al.*, "A soft magnetoelastic generator for wind-energy harvesting," *Advanced Materials*, vol. 34, no. 38, p. 2204238, 2022.

[77] X. Wang, S. Wang, Y. Yang, and Z. L. Wang, "Hybridized electromagnetic–triboelectric nanogenerator for scavenging air-flow energy to sustainably power temperature sensors," *ACS nano*, vol. 9, no. 4, pp. 4553–4562, 2015.

[78] R. Walden, C. Kumar, D. M. Mulvihill, and S. C. Pillai, "Opportunities and challenges in triboelectric nanogenerator (teng) based sustainable energy generation technologies: a mini-review," *Chemical Engineering Journal Advances*, vol. 9, p. 100237, 2022.

[79] R. Dallaev, T. Pisarenko, D. Sobola, F. Orudzhev, S. Ramazanov, and T. Trčka, "Brief review of pvdf properties and applications potential," *Polymers*, vol. 14, no. 22, p. 4793, 2022.

[80] L. Jin, X. Xiao, W. Deng, A. Nashalian, D. He, V. Raveendran, C. Yan, H. Su, X. Chu, T. Yang, *et al.*, "Manipulating relative permittivity for high-performance wearable triboelectric nanogenerators," *Nano Letters*, vol. 20, no. 9, pp. 6404–6411, 2020.

[81] S. K. Karan, R. Bera, S. Paria, A. K. Das, S. Maiti, A. Maitra, and B. B. Khatua, "An approach to design highly durable piezoelectric nanogenerator based on self-poled pvdf/alo-rgo flexible nanocomposite with high power density and energy conversion efficiency," *Advanced Energy Materials*, vol. 6, no. 20, p. 1601016, 2016.

[82] S.-R. Kim, J.-H. Yoo, and J.-W. Park, "Using electrospun agnw/p (vdf-trfe) composite nanofibers to create transparent and wearable single-electrode triboelectric nanogenerators for self-powered touch panels," *ACS applied materials & interfaces*, vol. 11, no. 16, pp. 15088–15096, 2019.

[83] H. H. Singh and N. Khare, "Improved performance of ferroelectric nanocomposite flexible film based triboelectric nanogenerator by controlling surface morphology, polarizability, and hydrophobicity," *Energy*, vol. 178, pp. 765–771, 2019.

[84] D. L. Vu, C. D. Le, and K. K. Ahn, "Polyvinylidene fluoride surface polarization enhancement for liquid-solid triboelectric nanogenerator and its application," *Polymers*, vol. 14, no. 5, p. 960, 2022.

[85] W. Tuichai, A. Karaphun, and C. Ruttanapun, "Improved dielectric properties of pvdf polymer composites filled with ag nanomaterial deposited reduced graphene oxide (rgo) hybrid particles," *Materials Research Bulletin*, vol. 145, p. 111552, 2022.

[86] J. L. Pura and J. Souto, "Optical and electrical properties of low-dimensional crystalline materials," 2023.

[87] K. Nomura, H. Ohta, A. Takagi, T. Kamiya, M. Hirano, and H. Hosono, "Room-temperature fabrication of transparent flexible thin-film transistors using amorphous oxide semiconductors," *nature*, vol. 432, no. 7016, pp. 488–492, 2004.

[88] S. Chun, W. Son, G. Lee, S. H. Kim, J. W. Park, S. J. Kim, C. Pang, and C. Choi, "Single-layer graphene-based transparent and flexible multifunctional electronics for self-charging power and touch-sensing systems," *ACS applied materials & interfaces*, vol. 11, no. 9, pp. 9301–9308, 2019.

[89] Z. Wu, Z. Chen, X. Du, J. M. Logan, J. Sippel, M. Nikolou, K. Kamaras, J. R. Reynolds, D. B. Tanner, A. F. Hebard, *et al.*, "Transparent, conductive carbon nanotube films," *Science*, vol. 305, no. 5688, pp. 1273–1276, 2004.

[90] Z. Wang and R. W. Scharstein, "Electrostatics of graphene: Charge distribution and capacitance," *Chemical Physics Letters*, vol. 489, no. 4-6, pp. 229–236, 2010.

[91] C. Liu, Z. Yu, D. Neff, A. Zhamu, and B. Z. Jang, "Graphene-based supercapacitor with an ultrahigh energy density," *Nano letters*, vol. 10, no. 12, pp. 4863–4868, 2010.

[92] V. Panchal, R. Pearce, R. Yakimova, A. Tzalenchuk, and O. Kazakova, "Standardization of surface potential measurements of graphene domains," *Scientific reports*, vol. 3, no. 1, p. 2597, 2013.

[93] L. Ruan, X. Yao, Y. Chang, L. Zhou, G. Qin, and X. Zhang, "Properties and applications of the β phase poly (vinylidene fluoride)," *Polymers*, vol. 10, no. 3, p. 228, 2018.

[94] I. Richard, A. K. Maurya, S. Shadman, E. Masquelier, L. S. Marthey, A. Neels, and F. Sorin, "Unraveling the influence of thermal drawing parameters on the microstructure and thermo–mechanical properties of multimaterial fibers," *Small*, vol. 18, no. 4, p. 2101392, 2022.

[95] M. Rahman, C. Dilsiz, and M. Ordu, "3d printed hollow-core polymer optical fiber with six-pointed star cladding for the light guidance in the near-ir regime," in *2022 International Conference on Information Science and Communications Technologies (ICISCT)*, pp. 1–3, IEEE, 2022.

[96] A. Leber, S. Laperrousaz, Y. Qu, C. Dong, I. Richard, and F. Sorin, "Thermally drawn elastomer nanocomposites for soft mechanical sensors," *Advanced Science*, vol. 10, no. 13, p. 2207573, 2023.

[97] D. A. Anderson, Y. M. Le Hir, J.-P. Planche, D. Martin, and A. Shenoy, "Zero shear viscosity of asphalt binders," *Transportation Research Record*, vol. 1810, no. 1, pp. 54–62, 2002.

[98] A. G. Page, M. Bechert, F. Gallaire, and F. Sorin, "Unraveling radial dependency effects in fiber thermal drawing," *Applied Physics Letters*, vol. 115, no. 4, 2019.

[99] V. Kumar, A. Kumar, D.-J. Lee, and S.-S. Park, "Estimation of number of graphene layers using different methods: a focused review," *Materials*, vol. 14, no. 16, p. 4590, 2021.

[100] A. C. Ferrari, J. C. Meyer, V. Scardaci, C. Casiraghi, M. Lazzeri, F. Mauri, S. Piscanec, D. Jiang, K. S. Novoselov, S. Roth, *et al.*, "Raman spectrum of graphene and graphene layers," *Physical review letters*, vol. 97, no. 18, p. 187401, 2006.

[101] G. Dovbeshko, V. Cherepanov, V. Boiko, A. Perederiy, M. Olenchuk, A. Negriyko, O. Posudievsky, V. Moiseyenko, and V. Romanyuk, "Raman modes and mapping of graphene nanoparticles on si and photonic crystal substrates," *Optical Materials: X*, vol. 15, p. 100163, 2022.

[102] A. C. Ferrari, "Raman spectroscopy of graphene and graphite: Disorder, electron–phonon coupling, doping and nonadiabatic effects," *Solid state communications*, vol. 143, no. 1-2, pp. 47–57, 2007.

[103] Y. Hwangbo, C.-K. Lee, A. E. Mag-Isa, J.-W. Jang, H.-J. Lee, S.-B. Lee, S.-S. Kim, and J.-H. Kim, "Interlayer non-coupled optical properties for determining the number of layers in arbitrarily stacked multilayer graphenes," *Carbon*, vol. 77, pp. 454–461, 2014.

[104] X. Cai, T. Lei, D. Sun, and L. Lin, "A critical analysis of the α, β and γ phases in poly (vinylidene fluoride) using ftir," *RSC advances*, vol. 7, no. 25, pp. 15382–15389, 2017.

[105] J. Choi, K. Lee, M. Lee, T. Kim, S. Eom, J. H. Sim, W. B. Lee, Y. Kim, C. Park, and Y. Kang, "High β-phase poly (vinylidene fluoride) using a thermally decomposable molecular splint," *Advanced Electronic Materials*, vol. 9, no. 1, p. 2200279, 2023.

[106] P. Sajkiewicz, A. Wasiak, and Z. Gocłowski, "Phase transitions during stretching of poly (vinylidene fluoride)," *European polymer journal*, vol. 35, no. 3, pp. 423–429, 1999.

[107] J. Yu, P. Jiang, C. Wu, L. Wang, and X. Wu, "Graphene nanocomposites based on poly (vinylidene fluoride): structure and properties," *Polymer composites*, vol. 32, no. 10, pp. 1483–1491, 2011.

[108] M. Kanik, O. Aktas, H. S. Sen, E. Durgun, and M. Bayindir, "Spontaneous high piezoelectricity in poly (vinylidene fluoride) nanoribbons produced by iterative thermal size reduction technique," *ACS nano*, vol. 8, no. 9, pp. 9311–9323, 2014.

[109] S. Castagnet, J.-L. Gacougnolle, and P. Dang, "Correlation between macroscopical viscoelastic behaviour and micromechanisms in strained α polyvinylidene fluoride (pvdf)," *Materials Science and Engineering: A*, vol. 276, no. 1-2, pp. 152–159, 2000.

[110] P. Martins, A. Lopes, and S. Lanceros-Mendez, "Electroactive phases of poly (vinylidene fluoride): Determination, processing and applications," *Progress in polymer science*, vol. 39, no. 4, pp. 683–706, 2014.

[111] G. Chen, M. Nie, and Q. Wang, "Microinjection of poly (vinylidene fluoride) in the presence of various additives," *Journal of Vinyl and Additive Technology*, vol. 24, no. 2, pp. 103–108, 2018.

[112] H. C. Bidsorkhi, A. G. D'Aloia, G. De Bellis, A. Proietti, A. Rinaldi, M. Fortunato, P. Ballirano, M. P. Bracciale, M. L. Santarelli, and M. S. Sarto, "Nucleation effect of unmodified graphene nanoplatelets on pvdf/gnp film composites," *Materials Today Communications*, vol. 11, pp. 163–173, 2017.

[113] A. Gebrekrstos, T. S. Muzata, and S. S. Ray, "Nanoparticle-enhanced β-phase formation in electroactive pvdf composites: a review of systems for applications in energy harvesting, emi shielding, and membrane technology," *ACS Applied Nano Materials*, vol. 5, no. 6, pp. 7632–7651, 2022.

[114] N. A. Shepelin, P. C. Sherrell, E. N. Skountzos, E. Goudeli, J. Zhang, V. C. Lussini, B. Imtiaz, K. A. S. Usman, G. W. Dicinoski, J. G. Shapter, *et al.*, "Interfacial piezoelectric polarization locking in printable ti3c2t x mxene-fluoropolymer composites," *Nature communications*, vol. 12, no. 1, p. 3171, 2021.

[115] N. Meng, X. Ren, G. Santagiuliana, L. Ventura, H. Zhang, J. Wu, H. Yan, M. J. Reece, and E. Bilotti, "Ultrahigh β-phase content poly (vinylidene fluoride) with relaxor-like ferroelectricity for high energy density capacitors," *Nature communications*, vol. 10, no. 1, p. 4535, 2019.

[116] D. Kim, I.-W. Tcho, I. K. Jin, S.-J. Park, S.-B. Jeon, W.-G. Kim, H.-S. Cho, H.-S. Lee, S. C. Jeoung, and Y.-K. Choi, "Direct-laser-patterned friction layer for the output enhancement of a triboelectric nanogenerator," *Nano Energy*, vol. 35, pp. 379–386, 2017.

[117] B. N. Persson, "Contact mechanics for randomly rough surfaces," *Surface science reports*, vol. 61, no. 4, pp. 201–227, 2006.

[118] H. Zhang, Y. Zhu, and L. Li, "Fabrication of pvdf/graphene composites with enhanced β phase via conventional melt processing assisted by solid state shear milling technology," *RSC advances*, vol. 10, no. 6, pp. 3391–3401, 2020.

[119] R. Korokhin, A. Shapagin, V. Solodilov, U. Zvereva, D. Solomatin, and Y. A. Gorbatkina, "Epoxy polymers modified with polyetherimide. part i: rheological and thermomechanical characteristics," *Polymer Bulletin*, vol. 78, pp. 1573–1584, 2021.

[120] M. Dobrzynski and K. Mietka, "Surface texture after turning for various workpiece rigidities," *Machines*, vol. 9, no. 1, p. 9, 2021.

[121] M. Dobrzynski and K. Mietka, "Surface texture after turning for various workpiece rigidities," *Machines*, vol. 9, no. 1, p. 9, 2021.

[122] W. Akram, Q. Chen, G. Xia, and J. Fang, "A review of single electrode triboelectric nanogenerators," *Nano Energy*, vol. 106, p. 108043, 2023.

[123] X. Zhang, L. Chen, Y. Jiang, W. Lim, and S. Soh, "Rationalizing the triboelectric series of polymers," *Chemistry of Materials*, vol. 31, no. 5, pp. 1473–1478, 2019.

[124] E. Németh, V. Albrecht, G. Schubert, and F. Simon, "Polymer tribo-electric charging: dependence on thermodynamic surface properties and relative humidity," *Journal of Electrostatics*, vol. 58, no. 1-2, pp. 3–16, 2003.

[125] X. Shen, W. Han, Y. Jiang, Q. Ding, X. Li, X. Zhao, and Z. Li, "Punching pores on cellulose fiber paper as the spacer of triboelectric nanogenerator for monitoring human motion," *Energy Reports*, vol. 6, pp. 2851–2860, 2020.

[126] T. Bhatta, S. Sharma, K. Shrestha, Y. Shin, S. Seonu, S. Lee, D. Kim, M. Sharifuzzaman, S. S. Rana, and J. Y. Park, "Siloxene/pvdf composite nanofibrous membrane for high-performance triboelectric nanogenerator and self-powered static and dynamic pressure sensing applications," *Advanced Functional Materials*, vol. 32, no. 25, p. 2202145, 2022.

[127] L.-B. Huang, W. Xu, C. Zhao, Y.-L. Zhang, K.-L. Yung, D. Diao, K. H. Fung, and J. Hao, "Multifunctional water drop energy harvesting and human motion sensor based on flexible dual-mode nanogenerator incorporated with polymer nanotubes," *ACS applied materials & interfaces*, vol. 12, no. 21, pp. 24030–24038, 2020.

[128] K. Shrestha, S. Sharma, G. B. Pradhan, T. Bhatta, S. S. Rana, S. Lee, S. Seonu, Y. Shin, and J. Y. Park, "A triboelectric driven rectification free self-charging supercapacitor for smart iot applications," *Nano Energy*, vol. 102, p. 107713, 2022.

[129] X. Xia, J. Chen, G. Liu, M. S. Javed, X. Wang, and C. Hu, "Aligning graphene sheets in pdms for improving output performance of triboelectric nanogenerator," *Carbon*, vol. 111, pp. 569–576, 2017.

[130] N. Maity, A. Mandal, and A. K. Nandi, "Hierarchical nanostructured polyaniline functionalized graphene/poly (vinylidene fluoride) composites for improved dielectric performances," *Polymer*, vol. 103, pp. 83–97, 2016.

[131] C. Wang, H. Guo, P. Wang, J. Li, Y. Sun, and D. Zhang, "An advanced strategy to enhance teng output: reducing triboelectric charge decay," *Advanced Materials*, vol. 35, no. 17, p. 2209895, 2023.

[132] Y. Liu, W. Liu, Z. Wang, W. He, Q. Tang, Y. Xi, X. Wang, H. Guo, and C. Hu, "Quantifying contact status and the air-breakdown model of charge-excitation triboelectric nanogenerators to maximize charge density," *Nature communications*, vol. 11, no. 1, p. 1599, 2020.

[133] N. Cui, L. Gu, Y. Lei, J. Liu, Y. Qin, X. Ma, Y. Hao, and Z. L. Wang, "Dynamic behavior of the triboelectric charges and structural optimization of the friction layer for a triboelectric nanogenerator," *ACS nano*, vol. 10, no. 6, pp. 6131–6138, 2016.

[134] Q. Su, S. Pang, V. Alijani, C. Li, X. Feng, and K. Müllen, "Composites of graphene with large aromatic molecules," *Adv. Mater*, vol. 21, no. 31, pp. 3191–3195, 2009.

[135] D. Kang, H. Y. Lee, J.-H. Hwang, S. Jeon, D. Kim, S. Kim, and S.-W. Kim, "Deformation-contributed negative triboelectric property of polytetrafluoroethylene: A density functional theory calculation," *Nano Energy*, vol. 100, p. 107531, 2022.

[136] M. Arjmand, S. Sadeghi, I. Otero Navas, Y. Zamani Keteklahijani, S. Dordanihaghighi, and U. Sundararaj, "Carbon nanotube versus graphene nanoribbon: impact of nanofiller geometry on electromagnetic interference shielding of polyvinylidene fluoride nanocomposites," *Polymers*, vol. 11, no. 6, p. 1064, 2019.

[137] S. Mishra, P. Supraja, D. Haranath, R. R. Kumar, and S. Pola, "Effect of surface and contact points modification on the output performance of triboelectric nanogenerator," *Nano Energy*, vol. 104, p. 107964, 2022.

[138] L. Lyons and T. Speiser, "Ohm's law for a current sheet," *Journal of Geophysical Research: Space Physics*, vol. 90, no. A9, pp. 8543–8546, 1985.

[139] Y. Huang, S. Kormakov, X. He, X. Gao, X. Zheng, Y. Liu, J. Sun, and D. Wu, "Conductive polymer composites from renewable resources: an overview of preparation, properties, and applications," *Polymers*, vol. 11, no. 2, p. 187, 2019.

[140] M.-J. Antonini, A. Sahasrabudhe, A. Tabet, M. Schwalm, D. Rosenfeld, I. Garwood, J. Park, G. Loke, T. Khudiyev, M. Kanik, *et al.*, "Customizing mri-compatible multifunctional neural interfaces through fiber drawing," *Advanced functional materials*, vol. 31, no. 43, p. 2104857, 2021.

[141] M. H. Malakooti, N. Kazem, J. Yan, C. Pan, E. J. Markvicka, K. Matyjaszewski, and C. Majidi, "Liquid metal supercooling for low-temperature thermoelectric wearables," *Advanced functional materials*, vol. 29, no. 45, p. 1906098, 2019.

[142] A. Majumdar, A. Ghosh, S. S. Saha, A. Roy, S. Barman, D. Panigrahi, and A. Biswas, "Empirical modelling of tensile strength of woven fabrics," *Fibers and Polymers*, vol. 9, pp. 240–245, 2008.

[143] X. Tian and T. Hua, "Antibacterial, scalable manufacturing, skin-attachable, and eco-friendly fabric triboelectric nanogenerators for self-powered sensing," *ACS Sustainable Chemistry & Engineering*, vol. 9, no. 39, pp. 13356–13366, 2021.

[144] T. Jing, B. Xu, and Y. Yang, "Organogel electrode based continuous fiber with large-scale production for stretchable triboelectric nanogenerator textiles," *Nano Energy*, vol. 84, p. 105867, 2021.

[145] Z. Wang, C. Luan, Y. Zhu, G. Liao, J. Liu, X. Li, X. Yao, and J. Fu, "Integrated and shape-adaptable multifunctional flexible triboelectric nanogenerators using coaxial direct ink writing 3d printing," *Nano Energy*, vol. 90, p. 106534, 2021.

[146] L. Ma, R. Wu, A. Patil, J. Yi, D. Liu, X. Fan, F. Sheng, Y. Zhang, S. Liu, S. Shen, *et al.*, "Acid and alkali-resistant textile triboelectric nanogenerator as a smart protective suit for liquid energy harvesting and self-powered monitoring in high-risk environments," *Advanced Functional Materials*, vol. 31, no. 35, p. 2102963, 2021.

[147] C. Ye, S. Yang, J. Ren, S. Dong, L. Cao, Y. Pei, and S. Ling, "Electroassisted core-spun triboelectric nanogenerator fabrics for intellisense and artificial intelligence perception," *ACS nano*, vol. 16, no. 3, pp. 4415–4425, 2022.

[148] Y. Yang, L. Xie, Z. Wen, C. Chen, X. Chen, A. Wei, P. Cheng, X. Xie, and X. Sun, "Coaxial triboelectric nanogenerator and supercapacitor fiber-based self-charging power fabric," *ACS Applied Materials & Interfaces*, vol. 10, no. 49, pp. 42356–42362, 2018.

[149] Y. Yang, N. Sun, Z. Wen, P. Cheng, H. Zheng, H. Shao, Y. Xia, C. Chen, H. Lan, X. Xie, *et al.*, "Liquid-metal-based super-stretchable and structure-designable triboelectric nanogenerator for wearable electronics," *ACS nano*, vol. 12, no. 2, pp. 2027–2034, 2018.

[150] A. Yu, X. Pu, R. Wen, M. Liu, T. Zhou, K. Zhang, Y. Zhang, J. Zhai, W. Hu, and Z. L. Wang, "Core–shell-yarn-based triboelectric nanogenerator textiles as power cloths," *ACS nano*, vol. 11, no. 12, pp. 12764–12771, 2017.

[151] L. Shen, S. Feng, J. Li, J. Chen, F. Li, H. Lin, and G. Yu, "Surface modification of polyvinylidene fluoride (pvdf) membrane via radiation grafting: novel mechanisms underlying the interesting enhanced membrane performance," *Scientific Reports*, vol. 7, no. 1, p. 2721, 2017.

[152] D. Bajpai, "Laundry detergents: an overview," *Journal of oleo science*, vol. 56, no. 7, pp. 327–340, 2007.

[153] C. Mac Namara, A. Gabriele, C. Amador, and S. Bakalis, "Dynamics of textile motion in a front-loading domestic washing machine," *Chemical engineering science*, vol. 75, pp. 14–27, 2012.

[154] A. Kilding, H. Tunstall, E. Wraith, M. Good, C. Gammon, and C. Smith, "Sweat rate and sweat electrolyte composition in international female soccer players during game specific training," *International journal of sports medicine*, pp. 443–447, 2009.

[155] H. Kinoshita and B. T. Bates, "The effect of environmental temperature on the properties of running shoes," *Journal of applied biomechanics*, vol. 12, no. 2, pp. 258–268, 1996.

[156] A. C. Wang, B. Zhang, C. Xu, H. Zou, Z. Lin, and Z. L. Wang, "Unraveling temperature-dependent contact electrification between sliding-mode triboelectric pairs," *Advanced Functional Materials*, vol. 30, no. 12, p. 1909384, 2020.

[157] X. Wen, Y. Su, Y. Yang, H. Zhang, and Z. L. Wang, "Applicability of triboelectric generator over a wide range of temperature," *Nano Energy*, vol. 4, pp. 150–156, 2014.

[158] B. Cheng, Q. Xu, Y. Ding, S. Bai, X. Jia, Y. Yu, J. Wen, and Y. Qin, "High performance temperature difference triboelectric nanogenerator," *Nature communications*, vol. 12, no. 1, p. 4782, 2021.

[159] Y. Zhou, W. Deng, J. Xu, and J. Chen, "Engineering materials at the nanoscale for triboelectric nanogenerators," *Cell Reports Physical Science*, vol. 1, no. 8, 2020.

[160] Y.-T. Jao, P.-K. Yang, C.-M. Chiu, Y.-J. Lin, S.-W. Chen, D. Choi, and Z.-H. Lin, "A textile-based triboelectric nanogenerator with humidity-resistant output characteristic and its applications in self-powered healthcare sensors," *Nano Energy*, vol. 50, pp. 513–520, 2018.

[161] Z. Zhang, T. He, M. Zhu, Q. Shi, and C. Lee, "Smart triboelectric socks for enabling artificial intelligence of things (aiot) based smart home and healthcare," in *2020 IEEE 33rd International Conference on Micro Electro Mechanical Systems (MEMS)*, pp. 80–83, IEEE, 2020.

[162] J.-N. Kim, J. Lee, H. Lee, and I.-K. Oh, "Stretchable and self-healable catechol-chitosan-diatom hydrogel for triboelectric generator and self-powered tremor sensor targeting at parkinson disease," *Nano Energy*, vol. 82, p. 105705, 2021.

[163] O. F. Ahmad, P. Ghosh, C. Stanley, B. Karp, M. Hallett, C. Lungu, and K. Alter, "Electromyographic and joint kinematic patterns in runner's dystonia," *Toxins*, vol. 10, no. 4, p. 166, 2018.

[164] Q. Zhang, T. Jin, J. Cai, L. Xu, T. He, T. Wang, Y. Tian, L. Li, Y. Peng, and C. Lee, "Wearable triboelectric sensors enabled gait analysis and waist motion capture for iot-based smart healthcare applications," *Advanced Science*, vol. 9, no. 4, p. 2103694, 2022.

[165] J. F. Hafer, A. M. Brown, P. DeMille, H. J. Hillstrom, and C. E. Garber, "The effect of a cadence retraining protocol on running biomechanics and efficiency: a pilot study," *Journal of sports sciences*, vol. 33, no. 7, pp. 724–731, 2015.

[166] X. Tian, S. Dong, M. Yang, H. Ng, Y. Liu, H. Hu, and T. Hua, "Textile-based triboelectric nanogenerators for smart wearable systems: Comfort, integration, and application," *Advanced Materials Technologies*, vol. 8, no. 8, p. 2201294, 2023.

[167] S. Lin, S. Hu, W. Song, M. Gu, J. Liu, J. Song, Z. Liu, Z. Li, K. Huang, Y. Wu, *et al.*, "An ultralight, flexible, and biocompatible all-fiber motion sensor for artificial intelligence wearable electronics," *npj Flexible Electronics*, vol. 6, no. 1, p. 27, 2022.

[168] M. Kang and T.-W. Kim, "Recent advances in fiber-shaped electronic devices for wearable applications," *Applied Sciences*, vol. 11, no. 13, p. 6131, 2021.

[169] Y. Zeng, H. Xiang, N. Zheng, X. Cao, N. Wang, and Z. L. Wang, "Flexible triboelectric nanogenerator for human motion tracking and gesture recognition," *Nano Energy*, vol. 91, p. 106601, 2022.

[170] D. Doganay, O. Demircioglu, M. Cugunlular, M. O. Cicek, O. Cakir, H. U. Kayaci, S. Ç. Aygün, and H. E. Unalan, "Wet spun core-shell fibers for wearable triboelectric nanogenerators," *Nano Energy*, vol. 116, p. 108823, 2023.

[171] G. Loke, T. Khudiyev, B. Wang, S. Fu, S. Payra, Y. Shaoul, J. Fung, I. Chatziveroglou, P.-W. Chou, I. Chinn, *et al.*, "Digital electronics in fibres enable fabric-based machine-learning inference," *Nature communications*, vol. 12, no. 1, p. 3317, 2021.

[172] D. Kim, Z. Yang, J. Cho, D. Park, D. H. Kim, J. Lee, S. Ryu, S.-W. Kim, and M. Kim, "High-performance piezoelectric yarns for artificial intelligence-enabled wearable sensing and classification," *EcoMat*, vol. 5, no. 8, p. e12384, 2023.

[173] Z. Yin, H. Lu, L. Gan, and Y. Zhang, "Electronic fibers/textiles for health-monitoring: fabrication and application," *Advanced Materials Technologies*, vol. 8, no. 3, p. 2200654, 2023.

[174] J. Liu, J. Zhang, J. Liu, W. Sun, W. Li, H. Shen, L. Wang, and G. Li, "Advances in fiber-based wearable sensors for personal digital health monitoring," *Materials*, vol. 16, no. 23, p. 7428, 2023.

[175] J. S. Meena, S. B. Choi, S.-B. Jung, and J.-W. Kim, "Electronic textiles: New age of wearable technology for healthcare and fitness solutions," *Materials Today Bio*, vol. 19, p. 100565, 2023.

[176] H. Tian, J. Ma, Y. Li, X. Xiao, M. Zhang, H. Wang, N. Zhu, C. Hou, and J. Ulstrup, "Electrochemical sensing fibers for wearable health monitoring devices," *Biosensors and Bioelectronics*, p. 115890, 2023.

[177] M. Chen, Y. Zhou, J. Lang, L. Li, and Y. Zhang, "Triboelectric nanogenerator and artificial intelligence to promote precision medicine for cancer," *Nano Energy*, vol. 92, p. 106783, 2022.

[178] M. Jiang, B. Li, W. Jia, and Z. Zhu, "Predicting output performance of triboelectric nanogenerators using deep learning model," *Nano Energy*, vol. 93, p. 106830, 2022.

[179] D. Yang, Y. Shang, Z. Li, and K. Wang, "Triboelectric nanogenerator assisted by machine learning," *ACS Applied Electronic Materials*, vol. 5, no. 12, pp. 6549–6570, 2023.

[180] Y. Xi, J. Hua, and Y. Shi, "Noncontact triboelectric nanogenerator for human motion monitoring and energy harvesting," *Nano Energy*, vol. 69, p. 104390, 2020.

[181] T. Kamilya and J. Park, "Highly sensitive self-powered biomedical applications using triboelectric nanogenerator," *Micromachines*, vol. 13, no. 12, p. 2065, 2022.

[182] I. Shabbir, N. Rubab, T. W. Kim, and S.-W. Kim, "Healthcare management applications based on triboelectric nanogenerators," *APL Materials*, vol. 9, no. 6, 2021.

[183] R. Gunasekhar, M. S. Reza, K. J. Kim, A. A. Prabu, and H. Kim, "Electrospun pvdf/aromatic hbp of 4th gen based flexible and self-powered teng for wearable energy harvesting and health monitoring," *Scientific Reports*, vol. 13, no. 1, p. 22645, 2023.

[184] S. Solanki, A. K. Gupta, U. Saha, A. V. Krasnoslobodtsev, R. K. Gupta, and B. D. Malhotra, "Triboelectric nanogenerator-based smart biomedical sensors for healthcare," *Sustainable Energy Technologies and Assessments*, vol. 57, p. 103233, 2023.

[185] S. Solanki, A. K. Gupta, U. Saha, A. V. Krasnoslobodtsev, R. K. Gupta, and B. D. Malhotra, "Triboelectric nanogenerator-based smart biomedical sensors for healthcare," *Sustainable Energy Technologies and Assessments*, vol. 57, p. 103233, 2023.

[186] J. Sun, L. Zhang, S. Gong, J. Chen, and H. Guo, "Device physics and application prospect of the emerging high-voltage supply technology arising from triboelectric nanogenerator," *Nano Energy*, p. 109010, 2023.

[187] D. Choi, Y. Lee, Z.-H. Lin, S. Cho, M. Kim, C. K. Ao, S. Soh, C. Sohn, C. K. Jeong, J. Lee, *et al.*, "Recent advances in triboelectric nanogenerators: from technological progress to commercial applications," *ACS nano*, vol. 17, no. 12, pp. 11087–11219, 2023.

[188] K. Chen, Y. Li, G. Yang, S. Hu, Z. Shi, and G. Yang, "Fabric-based teng woven with bio-fabricated superhydrophobic bacterial cellulose fiber for energy harvesting and motion detection," *Advanced Functional Materials*, vol. 33, no. 45, p. 2304809, 2023.

[189] K. Chen, Y. Li, G. Yang, S. Hu, Z. Shi, and G. Yang, "Fabric-based teng woven with bio-fabricated superhydrophobic bacterial cellulose fiber for energy harvesting and motion detection," *Advanced Functional Materials*, vol. 33, no. 45, p. 2304809, 2023.

[190] Y. Chen, Y. Ling, and R. Yin, "Fiber/yarn-based triboelectric nanogenerators (tengs): fabrication strategy, structure, and application," *Sensors*, vol. 22, no. 24, p. 9716, 2022.

[191] J. Zhong, Y. Zhang, Q. Zhong, Q. Hu, B. Hu, Z. L. Wang, and J. Zhou, "Fiber-based generator for wearable electronics and mobile medication," *ACS nano*, vol. 8, no. 6, pp. 6273–6280, 2014.

[192] X. Li, Z.-H. Lin, G. Cheng, X. Wen, Y. Liu, S. Niu, and Z. L. Wang, "3d fiber-based hybrid nanogenerator for energy harvesting and as a self-powered pressure sensor," *ACS nano*, vol. 8, no. 10, pp. 10674–10681, 2014.

[193] K. Dong, Y.-C. Wang, J. Deng, Y. Dai, S. L. Zhang, H. Zou, B. Gu, B. Sun, and Z. L. Wang, "A highly stretchable and washable all-yarn-based self-charging knitting power textile composed of fiber triboelectric nanogenerators and supercapacitors," *ACS nano*, vol. 11, no. 9, pp. 9490–9499, 2017.

[194] J. Ryu, J. Kim, J. Oh, S. Lim, J. Y. Sim, J. S. Jeon, K. No, S. Park, and S. Hong, "Intrinsically stretchable multi-functional fiber with energy harvesting and strain sensing capability," *Nano Energy*, vol. 55, pp. 348–353, 2019.

[195] Z. Zhao, C. Yan, Z. Liu, X. Fu, L.-M. Peng, Y. Hu, and Z. Zheng, "Machine-washable textile triboelectric nanogenerators for effective human respiratory monitoring through loom weaving of metallic yarns.," *Advanced Materials (Deerfield Beach, Fla.)*, vol. 28, no. 46, pp. 10267–10274, 2016.

[196] S. Pan, H. He, L. Xin, B. Li, X. Wu, X. Zhang, and P. Wang, "Super-elastic microstructured triboelectric fibers and textiles fabricated by extrusion and thermal drawing for smart-home applications," *Nano Energy*, vol. 122, p. 109259, 2024.

[197] X. Chen, Y. Liu, Y. Sun, T. Zhao, C. Zhao, T. A. Khattab, E. G. Lim, X. Sun, and Z. Wen, "Electron trapping & blocking effect enabled by mxene/tio2 intermediate layer for charge regulation of triboelectric nanogenerators," *Nano Energy*, vol. 98, p. 107236, 2022.

[198] S. Sathiyan, H. Ahmad, W. Chong, S. Lee, and S. Sivabalan, "Evolution of the polarizing effect of mos_2," *IEEE Photonics Journal*, vol. 7, no. 6, pp. 1–10, 2015.

[199] N. Kumar, P. D. Ukey, V. Francis, R. P. Singh, and S. Sahu, "Plastic pellets," in *Polymers for 3D Printing*, pp. 307–323, Elsevier, 2022.

[200] J. P. Greene, "Microstructures of polymers," *Automotive Plastics and Composites*, pp. 27–37, 2021.

[201] M. R. Goswami, P. Singh, P. Chamoli, S. Bhardwaj, K. Raina, and R. K. Shukla, "Effect of graphene oxide doping on the room temperature shear and dynamic rheological behaviour of pvdf," *Journal of Dispersion Science and Technology*, vol. 44, no. 7, pp. 1237–1247, 2023.

[202] K. Pandey, P. Yadav, D. Singh, S. K. Gupta, Y. Sonvane, I. Lukačević, J. Kim, and M. Kumar, "First step to investigate nature of electronic states and transport in flower-like mos2: Combining experimental studies with computational calculations," *Scientific reports*, vol. 6, no. 1, p. 32690, 2016.

[203] Y. Guo, X. Wei, J. Shu, B. Liu, J. Yin, C. Guan, Y. Han, S. Gao, and Q. Chen, "Charge trapping at the mos2-sio2 interface and its effects on the characteristics of mos2 metal-oxide-semiconductor field effect transistors," *Applied Physics Letters*, vol. 106, no. 10, 2015.

[204] J. E. Samaniego-Benitez, R. Mendoza-Cruz, L. Bazán-Díaz, A. Garcia-Garcia, M. J. Arellano-Jimenez, J. F. Perez-Robles, G. Plascencia-Villa,

J. J. Velázquez-Salazar, E. Ortega, S. E. Favela-Camacho, *et al.*, "Synthesis and structural characterization of mos 2 micropyramids," *Journal of Materials Science*, vol. 55, pp. 12203–12213, 2020.

[205] B. Li, L. Jiang, X. Li, P. Ran, P. Zuo, A. Wang, L. Qu, Y. Zhao, Z. Cheng, and Y. Lu, "Preparation of monolayer mos2 quantum dots using temporally shaped femtosecond laser ablation of bulk mos2 targets in water," *Scientific reports*, vol. 7, no. 1, p. 11182, 2017.

[206] J. Li, Q. Meng, W. Li, and Z. Zhang, "Influence of crystalline properties on the dielectric and energy storage properties of poly (vinylidene fluoride)," *Journal of Applied Polymer Science*, vol. 122, no. 3, pp. 1659–1668, 2011.

[207] D. T. K. Ong, J. S. C. Koay, M. T. Sim, K. C. Aw, T. Nakajima, B. Chen, S. T. Tan, and W. C. Gan, "High performance composition-tailored pvdf triboelectric nanogenerator enabled by low temperature-induced phase transition," *Nano Energy*, vol. 113, p. 108555, 2023.

[208] A. Sutka, K. Malnieks, A. Linarts, P. C. Sherrell, X. Yu, and E. Bilotti, "High-performance hybrid triboelectric generators based on an inversely polarized ultrahigh β-phase pvdf," *ACS Applied Energy Materials*, vol. 6, no. 18, pp. 9300–9306, 2023.

[209] M. Jangra, A. Thakur, S. Dam, S. Chatterjee, and S. Hussain, "Enhanced dielectric properties of mos2/pvdf free-standing, flexible films for energy harvesting applications," *Materials Today Communications*, vol. 34, p. 105109, 2023.

[210] X. Liu, J. Ma, X. Wu, L. Lin, and X. Wang, "Polymeric nanofibers with ultrahigh piezoelectricity via self-orientation of nanocrystals," *ACS nano*, vol. 11, no. 2, pp. 1901–1910, 2017.

[211] M. Gopika, B. Bindhu, K. Sandhya, and V. Reena, "Impact of surface-modified molybdenum disulphide on crystallization, thermal and mechanical properties of polyvinylidene fluoride," *Polymer Bulletin*, vol. 77, pp. 757–773, 2020.

[212] H. Parangusan, D. Al-Sowaidi, E.-H. Elhadrami, D. Ponnamma, and J. Bhadra, "Development of flexible pvdf/batio3-mos2 polymer nanocomposites for energy harvesting and gas sensing applications," *Journal of Materials Science: Materials in Electronics*, vol. 35, no. 10, p. 679, 2024.

[213] X. Zheng, Y. Zheng, H. Zhang, Q. Yang, and C. Xiong, "Flexible mos2@ electrospun pvdf hybrid membrane as advanced anode for lithium storage," *Chemical Engineering Journal*, vol. 370, pp. 547–555, 2019.

[214] M. N. Islam, R. H. Rupom, P. R. Adhikari, Z. Demchuk, I. Popov, A. P. Sokolov, H. F. Wu, R. C. Advincula, N. Dahotre, Y. Jiang, *et al.*, "Boosting piezoelectricity by 3d printing pvdf-mos2 composite as a conformal and high-sensitivity piezoelectric sensor," *Advanced Functional Materials*, vol. 33, no. 42, p. 2302946, 2023.

[215] Y. Zare, "Study of nanoparticles aggregation/agglomeration in polymer particulate nanocomposites by mechanical properties," *Composites Part A: Applied Science and Manufacturing*, vol. 84, pp. 158–164, 2016.

[216] X. Ma, Y. Zare, and K. Y. Rhee, "A two-step methodology to study the influence of aggregation/agglomeration of nanoparticles on young's modulus of polymer nanocomposites," *Nanoscale research letters*, vol. 12, pp. 1–7, 2017.

[217] S. Ippili, V. Jella, A. M. Thomas, C. Yoon, J.-S. Jung, and S.-G. Yoon, "Znal–ldh-induced electroactive β-phase and controlled dielectrics of pvdf for a high-performance triboelectric nanogenerator for humidity and pressure sensing applications," *Journal of Materials Chemistry A*, vol. 9, no. 29, pp. 15993–16005, 2021.

[218] D. Liu, L. Zhou, S. Cui, Y. Gao, S. Li, Z. Zhao, Z. Yi, H. Zou, Y. Fan, J. Wang, *et al.*, "Standardized measurement of dielectric materials' intrinsic triboelectric charge density through the suppression of air breakdown," *Nature Communications*, vol. 13, no. 1, p. 6019, 2022.

[219] M. N. Rylo, R. L. de Medeiros, and V. F. de Lucena Jr, "Gesture recognition of wrist motion based on wearables sensors," *Procedia Computer Science*, vol. 210, pp. 181–188, 2022.

[220] R. Tchantchane, H. Zhou, S. Zhang, and G. Alici, "A review of hand gesture recognition systems based on noninvasive wearable sensors," *Advanced Intelligent Systems*, vol. 5, no. 10, p. 2300207, 2023.

[221] H. Wang, B. Ru, X. Miao, Q. Gao, M. Habib, L. Liu, and S. Qiu, "Mems devices-based hand gesture recognition via wearable computing," *Micromachines*, vol. 14, no. 5, p. 947, 2023.

[222] D. Iyer, F. Mohammad, Y. Guo, E. Al Safadi, B. J. Smiley, Z. Liang, and N. K. Jain, "Generalized hand gesture recognition for wearable devices in iot: Application and implementation challenges," in *International Conference on Machine Learning and Data Mining in Pattern Recognition*, pp. 346–355, Springer, 2016.

[223] Y. Si, S. Chen, M. Li, S. Li, Y. Pei, and X. Guo, "Flexible strain sensors for wearable hand gesture recognition: from devices to systems," *Advanced Intelligent Systems*, vol. 4, no. 2, p. 2100046, 2022.

[224] S. Duan, F. Zhao, H. Yang, J. Hong, Q. Shi, W. Lei, and J. Wu, "A pathway into metaverse: Gesture recognition enabled by wearable resistive sensors," *Advanced Sensor Research*, vol. 2, no. 8, p. 2200054, 2023.

[225] Y. Wang, Z. Su, N. Zhang, R. Xing, D. Liu, T. H. Luan, and X. Shen, "A survey on metaverse: Fundamentals, security, and privacy," *IEEE Communications Surveys & Tutorials*, vol. 25, no. 1, pp. 319–352, 2022.

[226] J. Zhang, G. Chen, and J. Chen, "Magnetic skin for touchless human–computer interaction to prevent healthcare-associated infections," *Advanced Sensor Research*, vol. 1, no. 1, p. 2200008, 2022.

[227] K. M. Sagayam and D. J. Hemanth, "Hand posture and gesture recognition techniques for virtual reality applications: a survey," *Virtual Reality*, vol. 21, pp. 91–107, 2017.

[228] J. Huang, X. Yu, Y. Wang, and X. Xiao, "An integrated wireless wearable sensor system for posture recognition and indoor localization," *Sensors*, vol. 16, no. 11, p. 1825, 2016.

[229] S. Duan, J. Wu, J. Xia, and W. Lei, "Innovation strategy selection facilitates high-performance flexible piezoelectric sensors," *Sensors*, vol. 20, no. 10, p. 2820, 2020.

[230] M. Wang, Z. Yan, T. Wang, P. Cai, S. Gao, Y. Zeng, C. Wan, H. Wang, L. Pan, J. Yu, *et al.*, "Gesture recognition using a bioinspired learning architecture that integrates visual data with somatosensory data from stretchable sensors," *Nature Electronics*, vol. 3, no. 9, pp. 563–570, 2020.

[231] A. Moin, A. Zhou, A. Rahimi, A. Menon, S. Benatti, G. Alexandrov, S. Tamakloe, J. Ting, N. Yamamoto, Y. Khan, *et al.*, "A wearable biosensing system with in-sensor adaptive machine learning for hand gesture recognition," *Nature Electronics*, vol. 4, no. 1, pp. 54–63, 2021.

[232] Y. Lin, S. Duan, D. Zhu, Y. Li, B. Wang, and J. Wu, "Self-powered and interface-independent tactile sensors based on bilayer single-electrode triboelectric nanogenerators for robotic electronic skin," *Advanced Intelligent Systems*, vol. 5, no. 4, p. 2100120, 2023.

[233] S. Houis, E. Engelhardt, F. Wurm, and T. Gries, "Application of polyvinylidene fluoride (pvdf) as a biomaterial in medical textiles," in *Medical and Healthcare Textiles*, pp. 342–352, Elsevier, 2010.

[234] I. Markuniene, M. Rabiei, S. Nasiri, S. Urbaite, A. Palevicius, and G. Janusas, "Biocompatible piezoelectric pvdf/ha/agno3 thin film prepared by the solvent casting method," *Sensors*, vol. 23, no. 1, p. 289, 2022.

[235] D. F. V. Anaya and M. R. Yuce, "Wearable triboelectric sensor for respiration and coughing monitoring," in *2021 IEEE Sensors*, pp. 1–4, IEEE, 2021.

[236] Z. Ye, Y. Ling, M. Yang, Y. Xu, L. Zhu, Z. Yan, and P.-Y. Chen, "A breathable, reusable, and zero-power smart face mask for wireless cough

and mask-wearing monitoring," *ACS nano*, vol. 16, no. 4, pp. 5874–5884, 2022.

[237] M. H. Ebell, "Predicting pneumonia in adults with respiratory illness," *American family physician*, vol. 76, no. 4, pp. 560–562, 2007.

[238] K. Mochizuki, R. Shintani, K. Mori, T. Sato, O. Sakaguchi, K. Takeshige, K. Nitta, and H. Imamura, "Importance of respiratory rate for the prediction of clinical deterioration after emergency department discharge: a single-center, case–control study," *Acute medicine & surgery*, vol. 4, no. 2, pp. 172–178, 2017.

[239] M. M. Churpek, T. C. Yuen, M. T. Huber, S. Y. Park, J. B. Hall, and D. P. Edelson, "Predicting cardiac arrest on the wards: a nested case-control study," *Chest*, vol. 141, no. 5, pp. 1170–1176, 2012.

[240] S. Huang, J. Alexander, R. Grover, J. Maher, R. McCullough, R. McCullough, L. Moore, J. Weil, J. Sampson, and J. Reeves, "Increased metabolism contributes to increased resting ventilation at high altitude," *Respiration physiology*, vol. 57, no. 3, pp. 377–385, 1984.

[241] J. S. Weis, "Physiological, developmental and behavioral effects of marine pollution," 2014.

[242] J. Hallam and T. Dawson, "The pattern of respiration with increasing metabolism in a small dasyurid marsupial," *Respiration physiology*, vol. 93, no. 3, pp. 305–314, 1993.

[243] S. S. Choudhary and S. R. Choudhary, "Sleep effects on breathing and respiratory diseases," *Lung India*, vol. 26, no. 4, pp. 117–122, 2009.

[244] G. Gutierrez, J. Williams, G. A. Alrehaili, A. McLean, R. Pirouz, R. Amdur, V. Jain, J. Ahari, A. Bawa, and S. Kimbro, "Respiratory rate variability in sleeping adults without obstructive sleep apnea," *Physiological reports*, vol. 4, no. 17, p. e12949, 2016.

[245] M. Brauns, *The Comparative Effects of Three Enrichment Items on the Physiology and Behavior of Stalled Horses (Equus caballus)*. PhD thesis, UC Davis, 2024.

[246] J. Yun, J. Park, S. Jeong, D. Hong, and D. Kim, "A mask-shaped respiration sensor using triboelectricity and a machine learning approach toward smart sleep monitoring systems," *Polymers*, vol. 14, no. 17, p. 3549, 2022.

[247] A. Vázquez-López, J. S. del Río Saez, J. de la Vega, X. Ao, and D.-Y. Wang, "All-fabric triboelectric nanogenerator (af-teng) smart face mask: Remote long-rate breathing monitoring and apnea alarm," *ACS sensors*, vol. 8, no. 4, pp. 1684–1692, 2023.

[248] A. Rajabi-Abhari, J.-N. Kim, J. Lee, R. Tabassian, M. Mahato, H. J. Youn, H. Lee, and I.-K. Oh, "Diatom bio-silica and cellulose nanofibril for bio-triboelectric nanogenerators and self-powered breath monitoring masks," *ACS applied materials & interfaces*, vol. 13, no. 1, pp. 219–232, 2020.

[249] Q. Lu, H. Chen, Y. Zeng, J. Xue, X. Cao, N. Wang, and Z. Wang, "Intelligent facemask based on triboelectric nanogenerator for respiratory monitoring," *Nano Energy*, vol. 91, p. 106612, 2022.

[250] G. Liu, J. Nie, C. Han, T. Jiang, Z. Yang, Y. Pang, L. Xu, T. Guo, T. Bu, C. Zhang, *et al.*, "Self-powered electrostatic adsorption face mask based on a triboelectric nanogenerator," *ACS applied materials & interfaces*, vol. 10, no. 8, pp. 7126–7133, 2018.

[251] Y. Liu, J. Mo, Q. Fu, Y. Lu, N. Zhang, S. Wang, and S. Nie, "Enhancement of triboelectric charge density by chemical functionalization," *Advanced Functional Materials*, vol. 30, no. 50, p. 2004714, 2020.

[252] S. I. Hopper, S. L. Murray, L. R. Ferrara, and J. K. Singleton, "Effectiveness of diaphragmatic breathing for reducing physiological and psychological stress in adults: a quantitative systematic review," *JBI Evidence Synthesis*, vol. 17, no. 9, pp. 1855–1876, 2019.

[253] L. Whited, M. F. Hashmi, and D. D. Graham, "Abnormal respirations," 2017.

[254] A. Younes, S. Mandigout, L. Robin, and B. Borel, "What kind of non-pharmacological strategy for reducing sedentary behavior in copd? data from a scoping review.," *Respiratory Medicine*, p. 107662, 2024.

Appendix A

Experimental setup

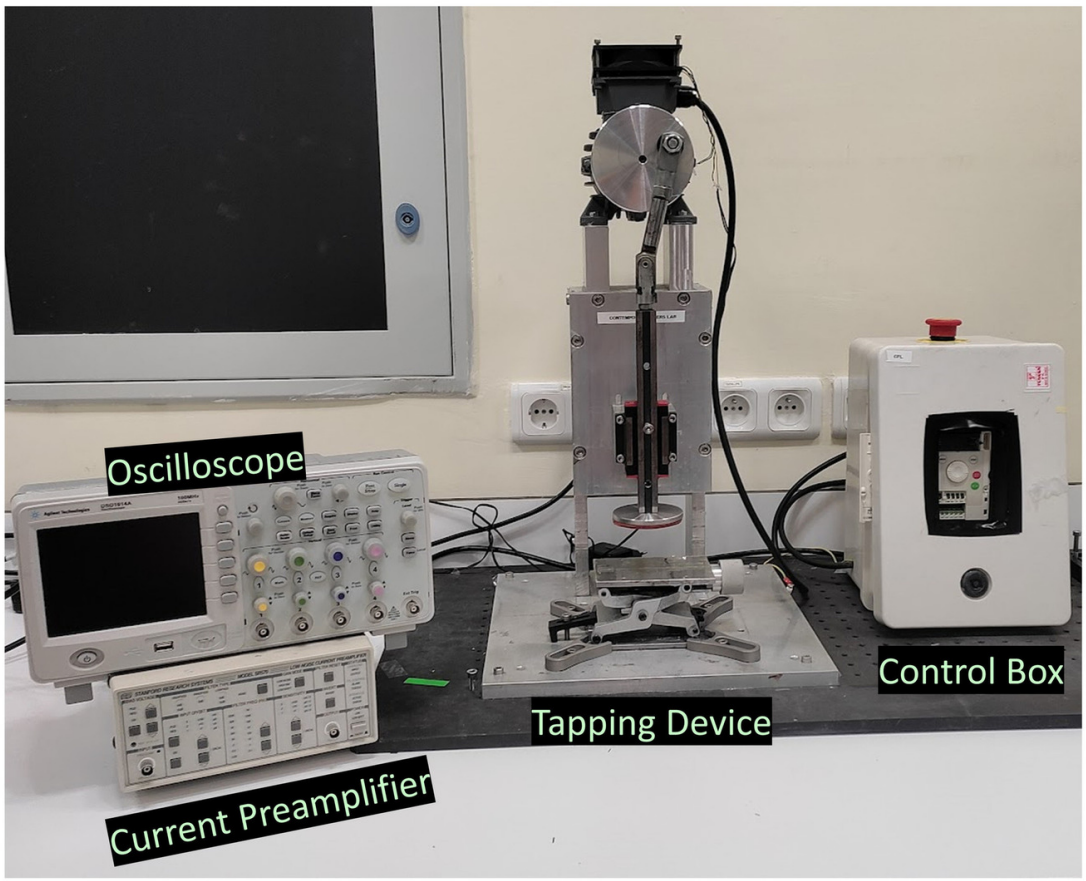

Figure A.1: Electrical characterization setup.

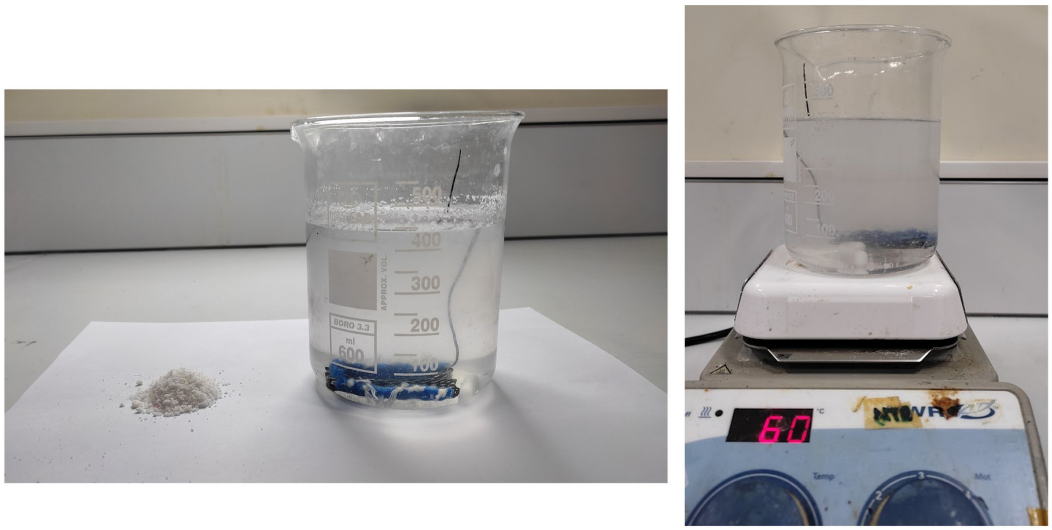

Figure A.2: Set up of wash-ability test for TENG fiber.

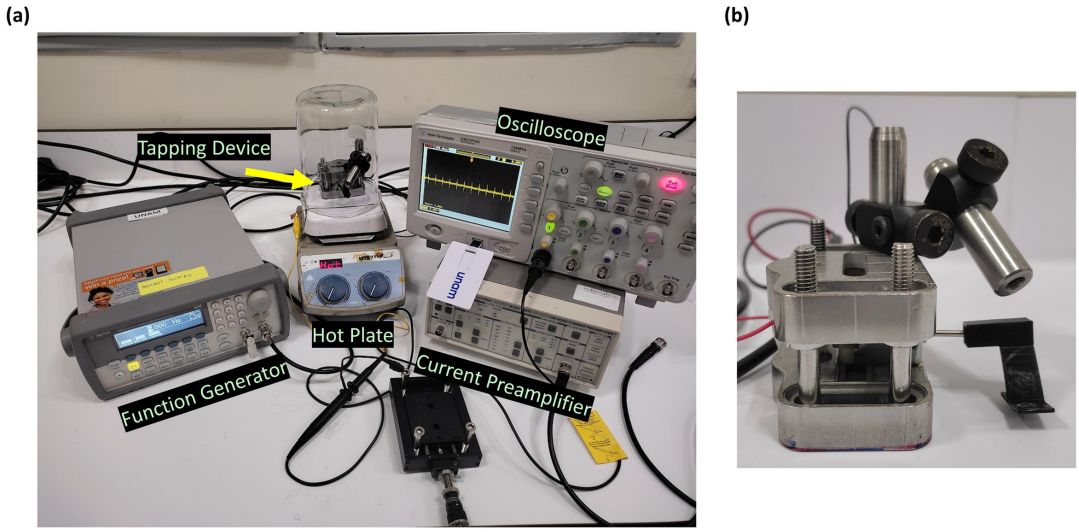

Figure A.3: Electrical characterization set up for temperature dependence test on triboelectric output. (b) Custom-made small tapping device that was placed over the hot plate.

Appendix B

Code

B.1 Arduino code with digital filter

const int analogPin = A0; // Analog pin connected to the TENG output unsigned long startTime; // Variable to store the start time float alpha = 0.2; // Initial exponential moving average weight float threshold = 0.1; // Threshold for dynamic weight adjustment float baseline = 0.0; // Estimated baseline voltage

void setup() Serial.begin(9600); Serial.println("Time (s) - Voltage (V)"); // Header for the data startTime = millis(); // Record the start time

void loop() unsigned long currentTime = millis(); // Get the current time float elapsedTime = (currentTime - startTime) / 1000.0; // Calculate elapsed time in seconds

int sensorValue = analogRead(analogPin); // Read the analog voltage float voltage = sensorValue * (5.0 / 1023.0); // Convert the analog value to voltage

// Adjust the filter weight based on the difference if (voltage ¿ baseline) alpha = 0.9; // Increase weight for faster response to peaks else alpha = 0.1; // Decrease weight for smoother filtering during lower values

// Exponential Moving Average Filter for baseline estimation baseline = alpha * voltage + (1 - alpha) * baseline;

// Subtract the baseline from the actual voltage to highlight irregularities float voltageWithoutBaseline = -voltage + baseline;

Serial.print(elapsedTime); Serial.print(" - "); Serial.println(voltageWithoutBaseline);

delay(100); // Delay for 1 second (adjust as needed)

B.2 Matlab code for data acquisition

serialPort = serial('COM3', 'BaudRate', 9600);

try fopen(serialPort);

figure; hLine = animatedline; xlabel('Time (s)'); ylabel('Voltage (V)'); title('Real-Time Arduino Data');

numPoints = 100; xData = zeros(1, numPoints); yData = zeros(1, numPoints);

axis auto;

while ishandle(hLine) dataString = fgetl(serialPort);

dataSplit = str2double(strsplit(dataString, ' - '));

xData = [xData(2:end), dataSplit(1)]; yData = [yData(2:end), dataSplit(2)];

clearpoints(hLine); addpoints(hLine, xData, yData);

drawnow; end

disp('Real-time data collection completed.');

```
catch err disp('Error occurred:'); disp(err.message);

if strcmp(serialPort.Status, 'open') fclose(serialPort); end end
```